Alma Mater Studiorum · Università di Bologna

Scuola di Scienze
Dipartimento di Fisica e Astronomia
Corso di Laurea in Fisica del Sistema Terra

Analysis and characterization of the morning and the evening transition over a west-facing slope: case-studies from the MATERHORN Program

Relatore:
Prof.ssa Silvana Di Sabatino

Correlatore:
Dott. Francesco Barbano

Presentata da:
Giulia Maria Bellucci

Sessione III
Anno Accademico 2021/2022

Sommario

La maggior parte delle terre emerse del nostro pianeta è molto distante dall'essere piatta o pianeggiante. L'interazione tra la topografia complessa e lo strato limite atmosferico a contatto con essa genera una grande varietà di fenomeni che sono stati negli anni oggetto di studio. L'evoluzione dei fenomeni che hanno luogo in questo strato dipende in larga parte dal ciclo diurno del sole e quindi dal riscaldamento o raffreddamento della superfice, soprattutto quando l'influenza delle condizioni sinottiche è bassa. Nelle zone montuose il riscaldamento disomogeneo genera una circolazione a piccola scala chiama thermally-driven circulation caratterizzata dalla presenza di venti superficiali che scendono lungo i pendii delle montagne e scorrono lungo le valli di notte, invertendo la loro direzione dopo il sorgere del sole. Il periodo che intercorre tra la fase notturna e quella diurna è detta morning transition e quella tra la fase diurna e quella notturna è detta evening transition.

Lo scopo di questa tesi è quello di caratterizzare la morning e la evening transition che si verificano sul fianco ovest di una montagna utilizzando i dati collezionati durante la campagna di presa dati chiamata MATERHORN (Mountain Terrain Atmospheric Modeling and Observations) che si è svolta in Utha nei pressi della Granite Mountain tra il 2012 e il 2013. Questo lavoro ha quindi lo scopo di approfondire la conoscenza della circolazione termica che si sviluppa sula fianco ovest di una montagna isolata, che è stata poco studiate durante gli anni. L'analisi riguarda 4 casi studio corrispondenti a 4 IOP (Intense Observation Period) caratterizzati da scarsa influenza sinottica, il che permette lo sviluppo indisturbato della circolazione termica.

L'analisi mostra che durante la morning transition avvengono due fenomeni principali: l'erosione dell'inversione termica notturna e la rotazione del vento. Questi fenomeni non avengono necessariamente in questo ordine e possono anche erificarsi contemporanea-

mente, a seconda del modo in cui il riscaldamento avviene che a sua volta dipende dalle caratteristiche del boundary layer notturno. Quando il processo di riscaldamento si attiva a partire dal suolo, la transizione parte dalla zona balla della slope prima dell'alba locale e la transizione nella zona alta è lenta. Quando il riscaldamento parte dall'alto a causa del mixing con l'aria negli strati superiori, la morning transition è ritardata in valle ed è veloce verso la la zona più inclinata della montagna.

Durante la evening transition la variazione di temperatura e la rotazione del vento si verificano in maniera inversa. Le caratteristiche del boundary layer convettivo determinano il modo in cui la transizione avviene. Se il CBL è debole la transizione si attiva prima ma è molto lenta e graduale e comincia dalla parte più ripida. Un CBL ben sviluppato è collegato ad una transizione più veloce che comincia dalla zona più in valle.

Abstract

Most of Earth's landmass is far from being flat. The interaction between the complex topography and the atmospheric boundary layer produces a great variety of phenomena that have been studied over the years. The evolution of these phenomena depends largely on the diurnal cycle of the radiation (and thus energy) budget, driving the heating and cooling of the surface, especially under weak synoptic conditions. The inhomogeneous heating in mountainous areas generates a small-scale circulation called *thermally-driven circulation*, characterized by the presence of surface winds that descend along the mountain slope and flow along the valleys at night, while climbing slopes and backtracking the valleys during daytime. In between, two transitional periods are observed around sunrise and sunset, called morning transition and evening transition, respectively. The scope of this thesis is to characterize the morning and evening transitions of a west-facing slope and adjacent valley, by means of experimental data collected within 4 case studies during the Mountain Terrain Atmospheric Modeling and Observations field campaign (MATERHORN) that took place in Utah near Granite Mountain between 2012 and 2013. In doing so, this thesis hopes to close some existing gaps concerning the development of thermally-driven circulations on west sides of isolated mountains, where very few in-field studies have been proposed in the past. The analysis addresses 4 case studies from the same number 4 IOPs (Intense Observation Period),characterized by weak synoptic conditions that allows the undisturbed development of thermal circulation, and uneven distribution among Autumn and Spring days to capture possible seasonalities. The results on this investigation has shown that during the morning transition, two main phenomena take place: the erosion of the temperature inversion and the rotation (i.e. transition) of the wind. The two phenomena do not necessarily occur in order, and may even occur

simultaneously depending on the warming process which in turn depends on the nocturnal boundary layer development. When the heating process is triggered from the ground, the transition starts from the flattest part of the west slope before local sunrise. and on the steeper part is slower. When the heating process is due to mixing with overlying air, the morning transition is delayed near the valley and is faster near the steepest slope. During the evening transition the temperature variation and the wind rotation occurs with a reversed process. The convective boundary layer characteristic determines the evening transition developing. A weakly developed CBL leads to an earlier transition onset, but very slow and gradual, starting from the steepest gentle slope. A well developed CBL leads to delayed but faster transition starting from the less steep part of the slope.

List of Figures

List of Figures

List of Figures

List of Tables

Contents

Introduction

The extreme variability of mountain weather is one of the most fascinating aspects of meteorology despite being one of the most important reasons for weather forecasts fails. Mountain weather comprises a myriad of phenomena which spans over a wide range of time and spatial scales. A fundamental obstacle to rapid progress in mountain meteorology is that there are almost infinite possible terrain configurations. So, any field measurement or numerical experiment that is valid for a specific situation does not automatically have greater significance beyond that case (Zardi and Whiteman, 2013).

Thermally driven winds are a well-recognized local flows under fair-weather conditions (Serafin et al., 2018). They develop due to differential heating of adjacent air masses and show regularly changing flow patterns during the day and the night. As the atmosphere is primarily heated or cooled by the Earth's surface, temperature contrasts in the boundary layer are mostly generated by inhomogeneous distributions of land properties (Whiteman, 2000). For example, land—sea breezes develop in regions with adjacent water and land surfaces, whereas mountain—plain circulations are found between flat plains and mountains. Along the mountain slopes and within the adjacent parallel-oriented valley, the-near surface circulation in a shallow layer above the ground of a mountain consists in an upslope/up-valley wind during the day and a downslope/down-valley wind during the night, following the daily cycle of insolation. (Zardi and Whiteman, 2013). In between of the nocturnal and the diurnal surface flow, two short transitional periods develop around sunrise and sunset, namely the morning and the evening transition respectively. Transition periods are problematic in numerical modeling, given rapid flow evolution and non-equilibrium turbulence (Fernando, 2010). Their complexity thus required a very detailed analysis. This thesis work focuses on the characterization of these two

transient phases and presents a data analysis of several case studies from the Mountain Terrain Atmospheric Modeling and Observations field campaign (MATERHORN) that took place in Utah between 2012 and 2013. The aim is the characterization and process identification of the transitional phases occurring under weak synoptic conditions along the west side of the Granite Mountain, an isolated massif already subject of intense investigation especially for its east side (Fernando et al., 2015). Following the aim of this investigation, this thesis is structured as follows. The first chapter starts with the characterization of the atmospheric boundary layer, followed by the description of the Mountain Wind System that develops in mountainous regions under weak synoptic forcing. The second chapter is aimed to the general overview of the MATERHORN project, of data, of methods and analyses performed for the data processing. The third chapter describes the data selection and the characteristics of the case studies , identified in 4 IOPs (Intensive Observation Periods), chosen on the basis of data availability among weak synoptic days. Specifically, two IOPs belong to the 2012 fall campaign and two to the 2013 spring . The description of the morning and the evening transition is found in the fourth chapter. The transitions description starts from the analysis of the solar radiation variation on the west side of the Granite Mountain, which shows well-defined distinctive features. This allows to identify numerous differences with what happens on the other side of the mountain and is fundamental for the understanding of the processes of heat loss and accumulation on the ground, deeply affecting the transition of the winds. Subsequently, the wind, relative humidity and temperature variations, measured between the surface and the first tens of meters of the atmosphere, were analyzed and described. In the end, the transitions were further analyzed with the help of TKE variations and kinematic heat fluxes. In the last chapter, the main characteristics of the analysis are summarized and commented, , drawing the conclusive remarks of this work.

Chapter 1

Atmospheric Boundary Layer over Complex Terrain

The boundary layer is defined as the layer of a fluid (liquid or gas) in the immediate vicinity of a material surface, in which significant exchange of momentum, heat, or mass takes place between the surface and the fluid (Arya, 2001).

The Atmospheric Boundary Layer (ABL) is the bottom layer of the atmosphere that feels the influence of the Earth's surface (lands and oceans), and it is the only atmospheric layer that experiences a diurnal (daily) cycle of temperature, humidity, wind and pollution variations (Stull, 2015), over times scales of a few hours to about 1 day.

1.1 General Characteristics of the ABL

The ABL evolves continuously in response to the heating and cooling of the earth's surface. Its development is regulated by the exchange of energy (heat) and mass (moisture) to and from the ground. However, although its spatial and temporal variability, the ABL has distinct state with peculiar physical characteristics.

1.1.1 Surface Energy Budget

The amount of heat and moisture transferred between the atmosphere and the underlying surface and the direction (upward or downward) of the transfer are determined

by the *surface energy budget* (Whiteman, 2000), that is shown in figure 1.1. This is evaluated at the Earth's surface and consists of a four-term budget: the net solar and terrestrial radiation (***R***),the sensible heat flux (***H***), the latent heat flux (***L***), the ground heat flux (***G***).

The Earth's surface is an infinitesimally thin layer, hence no heat can be stored in this layer and the sum of all incoming ad outgoing heat fluxes must exactly balance. The net flux at the surface must be zero (Stull, 2015).

The surface energy budget in units of $\mathrm{W\,m^{-2}}$, at any instant in time, is expressed by:

$$\mathbf{R} + \mathbf{H} + \mathbf{L} - \mathbf{G} = 0 \tag{1.1}$$

If the equation 1.1 is divided by $\rho_{air} \cdot C_p$ the balance is in kinematic form (in units of $\mathrm{K\,m\,s^{-1}}$).

$$\frac{\mathbf{R} + \mathbf{H} + \mathbf{L} - \mathbf{G}}{\rho_{air} \cdot C_p} = R + H + L - G \tag{1.2}$$

Fluxes are conventionally defined to be positive for heat moving upward, regardless of whether these fluxes are in the soil or the atmosphere (Stull, 2015).

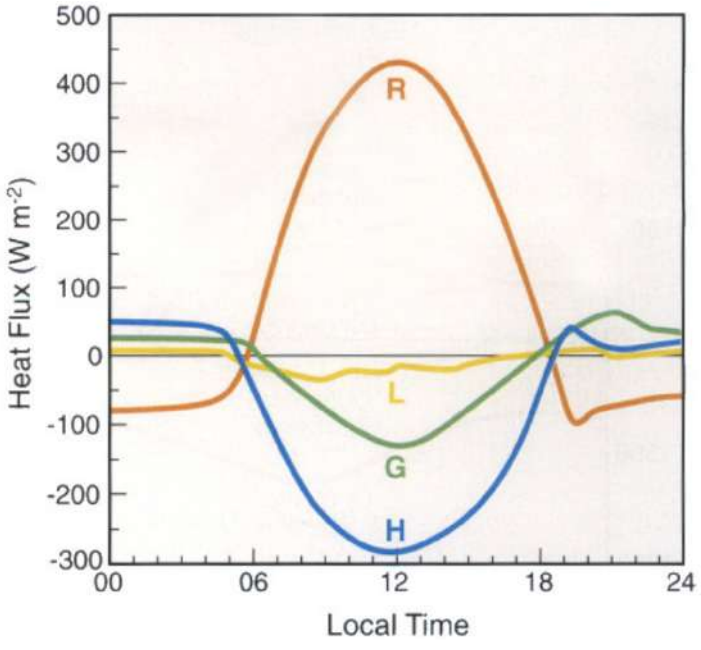

Figure 1.1: *Surface Energy Budget on a fair-weather June day. (Whiteman, 2000)*

The first three terms on the left in equation 1.1 are fluxes between the surface and the air above, while the last term is between the surface and the Earth below (hence the – sign).

Net radiation R is an external forcing that drives the other fluxes. R comprises radiation from the sun and ration from the Earth. The radiation emitted by an object depends on its temperature. The external temperature of the sun is approximately 6000° C and it emits radiation in the wavelength range 0.15-3 µm. This is

what we call *shortwave radiation*. The Earth and its atmosphere, which have a lower temperature, emit the so called *longwave radiation* at wavelengths of 3-100 µm. At the Earth's distance from the sun the intensities of solar and terrestrial radiation are comparable, even if there is no overlap between their spectra (Whiteman, 2000). Therefore, R has contributions from downwelling solar radiation K ↓ and reflected upwelling solar radiation K ↑, but also from downwelling longwave radiation emitted from the atmosphere I ↓ and upwelling longwave radiation emitted from the Earth I ↑ (Stull, 2015):

$$R = K\downarrow + K\uparrow + I\downarrow + I\uparrow \tag{1.3}$$

where K ↓ and I ↓ are negative because they are downward.

Conduction is the transfer of heat from the solid soil surface or liquid ocean surface into the air (Stull, 2015). The molecular heat conduction is caused by microscopic-scale vibrations and movements of air molecules transferring some of their microscopic kinetic energy to adjacent molecules. The molecular conductivity for air is small, and vertical temperature gradients are also small in most of the atmosphere. But near the ground in the ABL, large vertical temperature gradients frequently occur in the first mm of the atmosphere. This large temperature gradient compensates for the small molecular conductivity of air, to create turbulent vertical heat fluxes at the surface. The sum of molecular and turbulent heat fluxes gives rise to the so-called *effective turbulent heat flux*, that is shown in figure 1.2. At the surface, this effective flux is entirely due to molecular conduction, whereas above about 5 mm altitude effective flux is mostly due to turbulence. The effective flux is frequently

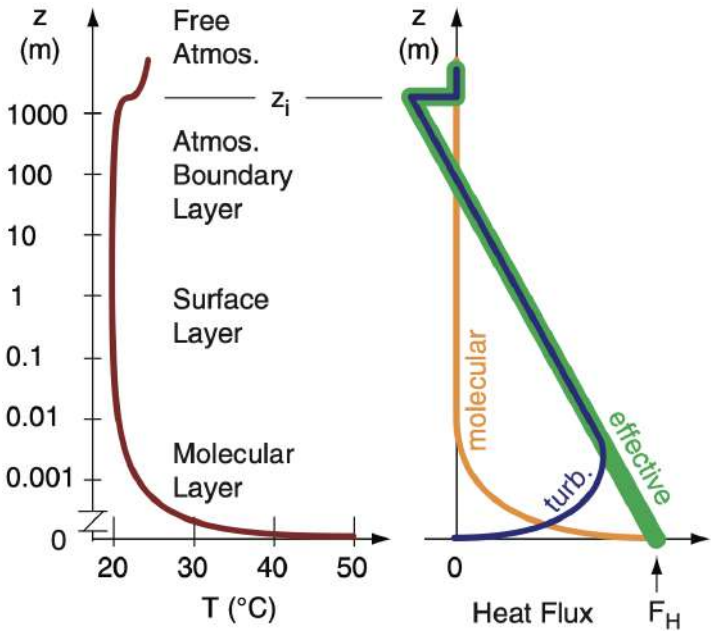

Figure 1.2: *Temperature gradient and heat fluxes. (Stull, 2015)*

approximate using the *bulk-transfer relationships*. For windy conditions where most of the turbulence in the ABL is caused by wind shear (change of wind speed or direction with altitude),the following formula may be used (in kinematic form) (Stull, 2015):

$$H = C_H \cdot M \cdot (\theta_{sfc} - \theta_{air}) \tag{1.4}$$

where M is the wind speed at 10 m AGL and C_H is the dimensionless *bulk heat-transfer coefficient* and varies from about 2×10^{-3} over smooth lakes or salt flats to about 2×10^{-2} for a rougher surface such as a forest. The potential temperature θ_{sfc} and θ_{air} are the potential temperature at the surface skin and the corresponding value at 2 m AGL (above ground level) respectively. The potential temperature is the temperature an air parcel with absolute temperature T and pressure p would have if brought adiabatically to the pressure at the 1000 mbar = 1000 hPa level (Kaimal and Finnigan, 1994), and it is calculated by:

$$\theta(z) = T(z) + \Gamma_d \cdot z \tag{1.5}$$

or

$$\theta = T \cdot \left(\frac{P_0}{P}\right)^{(\Re_d/C_p)} \tag{1.6}$$

where z can be the either the height above mean sea level and height AGL, and $\Gamma_d = 9.8$ $\mathrm{K\,km^{-1}}$ is the dry adiabatic lapse rate, that is the temperature change with height for dry air (Stull, 2015). The reference pressure is $P_0 = 1000$ hPa and $\Re_d/C_p = 0.28571$ is dimensionless, where $\Re_d = 287.053$ $\mathrm{J\,K^{-1}\,kg^{-1}}$ is the gas constant for dry air and C_p is the specific heath capacity. The potential temperature of an air parcel is constant for an adiabatic sinking or rising processes, but can increase/decrease when sensible heat is added/removed, such as during turbulent mixing, condensation and radiative heating (Stull, 2015).

For calm sunny conditions, turbulence is created by thermals of warm air rising due to their buoyancy. The resulting circulations produces a stirred well mixed layer, which is described by the following formulae (Stull, 2015):

$$H = b_H \cdot w_B \cdot (\theta_{sfc} - \theta_{ML}) \tag{1.7}$$

where $b_H = 5 \times 10^{-4}$ is called a *convective transport coefficient*. θ_{ML} is the *mid-mixed-layer potential temperature* (at height 500 m for a ML that is 1 km thick). The w_B factor is

called the *buoyancy velocity scale* ($\mathrm{m\,s^{-1}}$) (Stull, 2015):

$$w_B = \left[\frac{|g| \cdot z_i}{T_{v\,ML}} \cdot (\theta_{v\,sfc} - \theta_{v\,ML})\right]^{1/2} \tag{1.8}$$

where $\theta_{v\,ML}$ and $T_{v\,ML}$ are virtual potential temperature and virtual temperature in the mixed layer, $\theta_{v\,sfc}$ is the surface skin virtual potential temperature, z_i is the depth of the mixed layer and $|g| = 9.81\ \mathrm{m\,s^{-2}}$. The virtual temperature includes the effects of the presence of water vapor in the air and it is defined as $T_v = T \cdot [1 + (a \cdot r)]$, where $a = 0.61$ $\mathrm{g_{dry\ air}\,g^{-1}_{water\ vapor}}$ and r is the water vapor mixing ratio ($\mathrm{g_{water\ vapor}\,g^{-1}_{dry\ air}}$). Typical updraft speeds in thermals are of order $0.02 \cdot w_B$.

The latent heat flux is tied to the movement of water molecules ad thus to the moisture flux at the Earth's surface. The relationship between latent heat flux ($\mathrm{W\,m^{-2}}$) and vertical water vapor flux ($\mathrm{kg_{water}\,m^{-2}\,s^{-1}}$) is (Stull, 2015):

$$\mathbf{F_{water}} = \mathbf{L}/L_v \tag{1.9}$$

where $L_v = 2.5 \times 10^6\ \mathrm{J\,kg^{-1}_{water}}$ is the latent heat of vaporization. If the vertical water vapor flux is divided by air density ρ_{air} and the latent heat flux is divided by $\rho_{air} \cdot C_P$ the equation is then in kinematic form (in units of $\mathrm{K\,m\,s^{-1}}$) (Stull, 2015):

$$F_{water} = \gamma \cdot L \tag{1.10}$$

$\gamma = C_p/L_v = 0.4$ ($\mathrm{g_{water}\,kg^{-1}_{air}}$)$\mathrm{K^{-1}}$ is the *psycrometric constant*. The units of kinematic water flux F_{water} are ($\mathrm{kg_{water}\,kg^{-1}_{air}}$)$\cdot$($\mathrm{m\,s^{-1}}$). The evaporation rate of water on the Earth's surface (i.e. the depth decrease rate of a puddle) is related to the moisture flux according to this equation (Stull, 2015)

$$Evap_{rate} = \frac{\rho_{air}}{\rho_{water}} \cdot F_{water} = \frac{\rho_{air}}{\rho_{water}} \cdot \gamma \cdot L \tag{1.11}$$

For this equation $\rho_{water} = 1000\ \mathrm{kg_{water}\,m^{-3}}$. For windy conditions, another way to estimate the water vapor flux (in kinematic units) is with a *bulk-transfer relationship* similar to 1.4 (Stull, 2015):

$$F_{water} = \gamma \cdot L = C_H \cdot M \cdot (r_{sfc} - r_{air}) \tag{1.12}$$

where M is the wind speed at 10 m AGL and r_{air} is the water-vapor mixing ratio in the air at 2 m AGL. The *bulk-transfer coefficient* C_H is roughly the same as equation 1.4. In calmer conditions with sunny skies, convective thermals of warm raising air can form, which are effective at transporting moisture in the vertical. The resulting kinematic water vapor flux is (Stull, 2015):

$$F_{water} = \gamma \cdot L = b_H \cdot w_B \cdot (r_{sfc} - r_{ML}) \tag{1.13}$$

for a mid-mixed layer mixing ratio of r_{ML} and a *convective heath-transport coefficient*of $b_H = 5 \times 10^{-4}$(dimensionless). w_B is the buoyancy-velocity scale. The last equation has a problem in the mixing ratio at the surface r_{sfc} (literally at the Earth's surface skin) because this is an abstract concept that is not measurable. Thus, for the special case of a river or lake surface or rain-saturated ground, scientists often approximate $r_{sfc} \approx r_s(T_{sfc})$; namely the surface mixing ratio equals the saturation mixing ratio r_s for air at a temperature T_{sfc} equal to that of the surface skin (Stull, 2015).

Ground heat flux G accounts for the energy gained or lost during belowground warming or cooling. A crude first-oder approximation for heat flux down into the soil is (in kinematic units) (Stull, 2015):

$$G \approx X \cdot R \tag{1.14}$$

with factor $X = (0.1/0.5)$ for daytime/nighttime. R is the net radiation.

The tilt of the Earth's axis, as well as latitude, altitude, day of the year, time of the day, cloud cover, aerosol content, slope and orientation of the surface and ground cover all affect the surface energy budget (Whiteman, 2000). However on the ABL timescales, under cloudless conditions, the diurnal variation of the insolation is the main responsible for the net radiation oscillation during the day. Incoming solar radiation peaks at midday, growing from sunrise and decreasing until sunset. Incoming and outgoing longwave radiation continue all day long, but the latter peaks in early afternoon.

At night, the absence of solar radiation makes R driven by a net loss of longwave radiation from the surface, so that R becomes negative approximately one hour before sunset until one hour after sunrise.

The decrease of R during night is balanced by an increase in upward flux of heat from the ground, downward flux of heat from the air, and condensation of moisture at the

surface. Contrariwise, higher values of R at the surface during the day heats the ground and the air while evaporating water from the surface.

1.1.2 Diurnal Evolution of the ABL

Atmospheric stability quantify the resistance of the atmosphere to vertical motion and thereby controls formation and evolution of the ABL. The fair-weather ABL over flat terrain experiences a regular evolution of the vertical temperature structure as a consequence of the upward and downward sensible heat flux.

The behavior of an air parcel lifted a very small distance up or down from a point in the atmosphere is studied in order to define the static stability. When an air parcel moves vertically, its temperature changes. Furthermore, when it is lifted, the lower pressure makes it expand and cool. In contrast, a parcel that is lowered in the atmosphere is brought to a higher pressure, causing it to compress and warm (Whiteman, 2000). If the displaced parcel is warmer than its surroundings at the same height or pressure, the parcel is positively buoyant and rises, and the atmospheric layer trough which it moves is said to be *statically unstable*. If cooler, it is negative buoyant and sinks back to its starting point, indicating that the layer is *statically stable*. A parcel with the same temperature as its surroundings experiences zero buoyant force and it remains where it was released, indicating that the atmospheric layer is *neutral*. The rate at which temperature decrease with height is called the *lapse rate*, whether it refers to the adiabatic cooling of a rising parcel or the actual decrease of environmental temperature. In case of an air

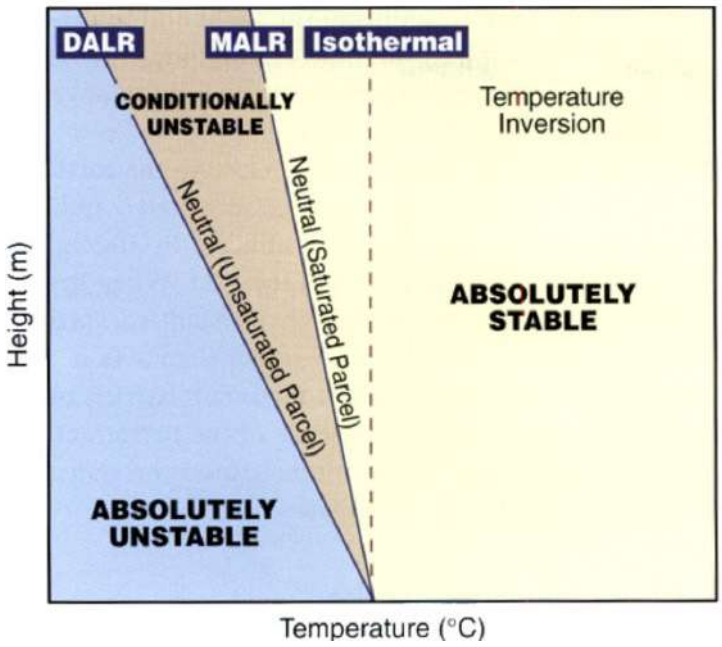

Figure 1.3: *Atmospheric stability. (Whiteman, 2000)*

parcel, the lapse rate depends on water content, thus an unsaturated (relative humidity less than 100% and contains no liquid water) raised parcel cools at a constant rate, called the *dry adiabatic lapse rate* (DALR), of 9.8°C per km, and a saturated (relative humidity of 100%) lifted parcel cools at the *moist adiabatic lapse rate* (MALR). The latter is not constant but depends on the parcel's temperature and pressure, and it is always lower than the DALR, since the latent heat released to condense the water partially offset the expansion cooling. At low temperature, when the saturated parcel can hold a very small amount of water, the two lapse rate are about the same.

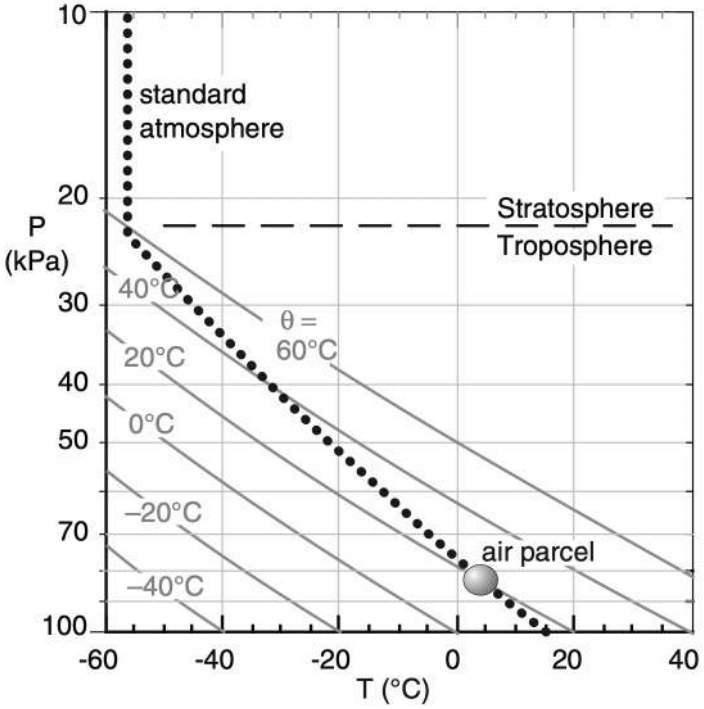

Figure 1.4: *Standard atmosphere (dotted black line) plotted on a thermodynamic diagram. The circle represents a hypothetical air parcel. Diagonal grey lines are dry adiabats (Stull, 2015)*

The atmospheric stability in a layer can be determined comparing the slope of an environmental temperature profile with the DALR and the MALR (Fig.1.3), taking into account whether the layer is or is not saturated. A typical vertical temperature structure in the atmosphere is described by the *Standard Atmosphere*. The Standard Atmosphere is an engineering approximation of the atmosphere adopted as a reference which represents average annual conditions at midlatitudes, although it is not calculated from data at any one location (Whiteman, 2000). The standard atmosphere in the troposphere is not parallel to the dry adiabats (Fig.1.4), but crosses the adiabats toward warmer potential temperatures as altitude increases (Stull, 2015). Therefore, the standard atmosphere is statically stable. However, the ABL is often turbulent, and when turbulent mixing occurs during daytime, the lower part of the troposphere exhibits a temperature profile

that is uniform with height. In such situation, the ABL corresponds to a *Mixed Layer* called *Convective Boundary Layer* (CBL) (Fig. 1.5), which is statically unstable. This is common on sunny days in fair weather or whenever cold air blows over a warmer surface. The CBL can reaches height of 3-4 km on sunny summer days. It is capped by the strongly stable *Entrainment Zone* formed during the day, which allows the CBL to grow by incorporating air from the overlying free atmosphere.

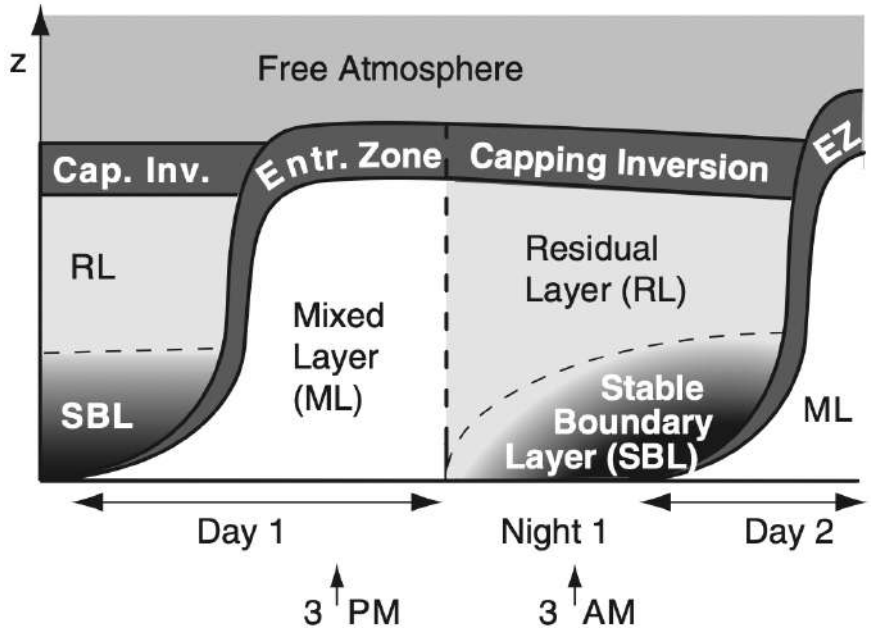

Figure 1.5: *Components of the boundary layer during fair weather in summer over land. White indicates nonlocally statically unstable air, light grey (as in the RL) is neutral stability, and darker greys indicate stronger static stability (Stull, 2015).*

At night, the ground quickly loses heat and a layer of cold air develops in close vicinity of it. This layer is called *Stable Boundary Layer* (SBL), and the more the atmosphere loses heat with a downward sensible heat flux, the deeper the stable layer grows during night, until it reaches several hundred meters just before sunrise. The ground cooling is responsible for the formation of a temperature inversion below the *Residual Layer*, that is usually statically neutral. The residual layer is composed of leftover convection and it persists during night. It is topped by a *Capping Inversion* which is still very stable.

The description of the ABL we have made thus far, cannot be applied to the Mountain

Boundary Layer without making any changes. Over the plain, earth-atmosphere exchanges are essentially restricted to turbulent mixing. Over mountains, we have to deal with a multi-layered structure and a variety of atmospheric processes at different scales (Lehner and Rotach, 2018) that are not covered by flat terrain ABL.

1.2 Atmospheric Boundary Layer Over Mountainous Regions

Where the terrain is complex and heterogeneous, the daily cycle of the ABL is not only influenced by the daily cycle of radiative heating (i.e., enhancement and suppression of turbulent mixing) but also by baroclinicity due to differential heating or cooling (Serafin et al., 2018), which leads to thermally driven flows, especially under weak synoptic forcing. Flows over complex terrain concernes different types of surfaces:

- inhomogeneous surface, such as coastal regions urban-rural transitions
- non-flat terrain, like hills and mountains
- rough surfaces, namely forests or cities

Complex topography may include all three types of surface above mentioned. Indeed, in such a case the ABL structure is much more intricate, and it can be divided in four different regions (Fig.1.6), as first stated by Ekhart (Ekhart, 1948): the slope atmosphere with a depth of a hundred meters; a valley atmosphere characterized by valley flows; a large-scale mountain atmosphere which encompasses the entire mountain range; and an unperturbed free atmosphere which contains the whole, at great distance from the mountain ridge(De Wekker and Kossmann, 2015). Each components of this atmosphere interacts with the others and none can be observed separately from the others.

The thermally-driven circulation on mountainous terrain plays an important role in the ABL, since it is found almost all over the world (i.e., over a wide range of spatial scales) and it may affect large scale phenomena. It follows a daily cycle and it is stronger under weak synoptic forcing on clear-sky days. The small-scale end of thermally-driven

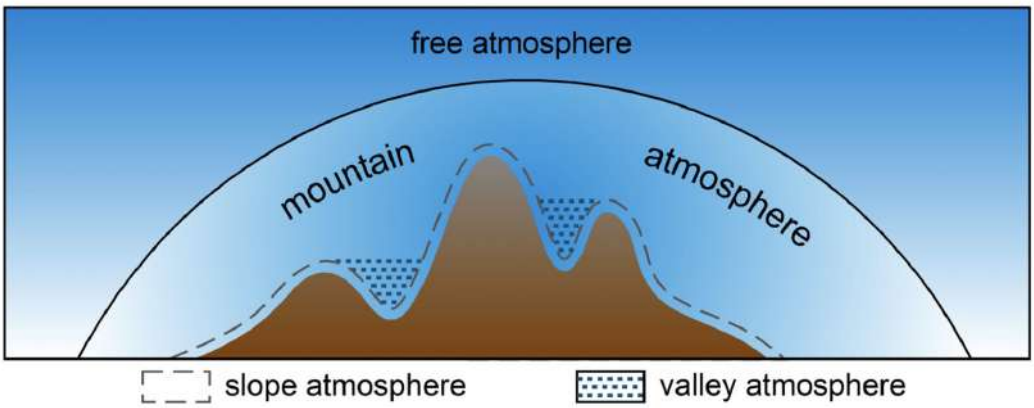

Figure 1.6: *Atmospheric structure over a mountain ridge. (De Wekker and Kossmann, 2015)*

baroclinic circulations over mountainous terrain corresponds to slope winds (Serafin et al., 2018).

1.3 Mountain Wind Systems

Mountain winds develop in mountainous regions, generally under weak synoptic forcing. The inhomogeneous distributions of land properties and surface shapes generates nonuniform surface temperature. Air at a given point in the sloping boundary layer is colder or warmer than the air just outside the boundary layer at the same elevation. These temperature differences are responsible for the formation of an horizontal pressure gradient, which in turn generates winds that blow from a point with lower temperature and higher pressure toward point with higher temperature and lower pressure. By convention, daytime flows are *upslope*, *up-valley* and *plain-to-mountain* whereas nighttime flows are *downslope*, *down-valley* and *mountain-to-plain* (Zardi and Whiteman, 2013). In a traditional view, each flow has corresponding compensatory currents aloft, presumably to form a closed circulation, as shown in figure 1.7.

The mountain wind system is composed by four types of flow. However, it is difficult to observe any one component in its pure form because each flow interacts with the others (Whiteman, 2000).

1. The slope wind system (upslope and downslope winds) is driven by horizontal

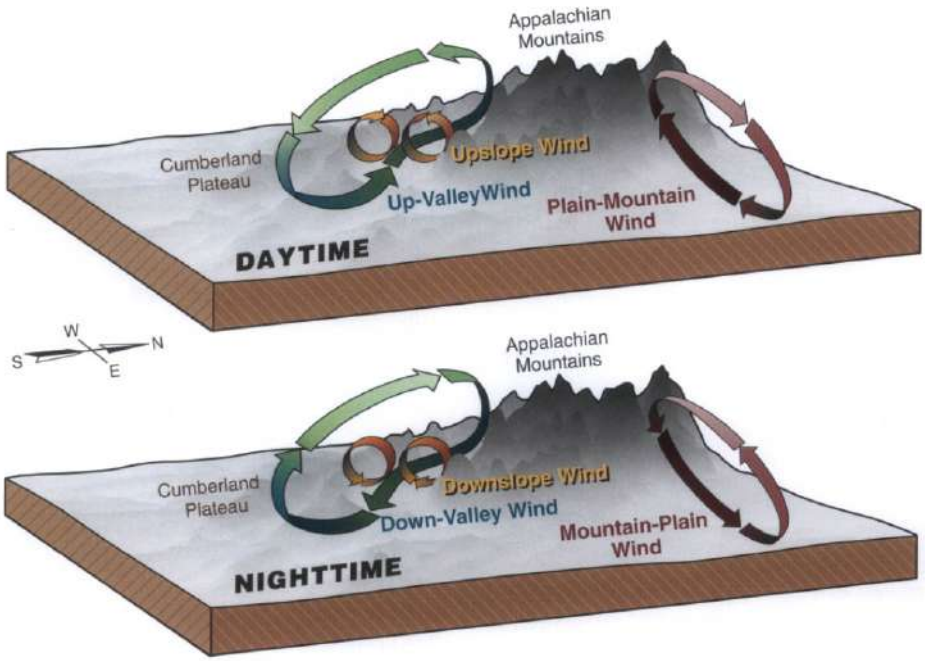

Figure 1.7: *Wind systems found over mountainous terrain (digital elevation model of the Appalachian Mountains).The third wind system, cross-valley flow (not shown), blows from cooler sidewalls toward warmer sidewalls.(Elevation model provided by J. Fast, Battelle Northwest Laboratories). (Whiteman, 2000)*

temperature contrasts between the air over the valley sidewalls and the air over the center of the valley.

2. The along-valley wind system (up-valley and down-valley winds) is driven by horizontal temperature contrasts along a valley's axis or between the air in a valley and the air over the adjacent plain.

3. The cross-valley wind system results from horizontal temperature differences between the valley sidewalls, producing winds that blow perpendicular to the valley axis and toward the more strongly heated sidewall.

4. The mountain-plain wind system results from horizontal temperature differences between the air over a mountain massif and the air over the surrounding plains, producing large-scale winds that blow up or down the outer slopes of a mountain

massif. The mountain-plain circulation and its upper level return flow are not confined by the topography but are carried over deep layers of the atmosphere above the mountain slopes.

The sun is the engine that drives mountain wind systems, and the strongest development of this circulation occurs during sunny summer days with sufficiently weak synoptic flow. In addition to the factors that characterize the diurnal insolation on a flat surface (subsection 1.1.1), the occurrence of wind systems in mountainous regions is dominated by formation and propagation of topographic shadings, which makes the exposure to insolation highly variable and causes differential heating of the ground.

Let us consider a mountain massif with an adjacent shallow valley which opens in a plain (that is the topographical configuration analyzed in this thesis). It is possible to describe the general relationship between mountain winds (i.e., slope, along valley and plain to mountain winds) and thermal forcing following the daily solar cycle (Fig. 1.8) (Whiteman, 2000):

- The *evening transition period* begins shortly before sunset (The evening transition will be analysed in details in section 1.3.4.2). It is characterized by the disruption of the upslope and up-valley winds and the gradual onset of the downslope and down-valley winds. The absence of incident solar radiation produce cooling of the valley and sidewalls surface and, as a result, the air near the surface becomes cooler. The temperature difference between the air above the slope and the air over the valley at the same height induce a sinking of cold air along the sidewalls down in the valley, creating a temperature inversion layer. When the air along the valley cross-section becomes colder than the air over the adjacent plain and the wind reverse completely to down-valley, the transition is over.

- During the *nighttime phase*, the downslope winds continue on the sidewalls and the down-valley persist within the valley temperature inversion. The stable structure along the valley hinders the vertical exchange of air between the valley and the free atmosphere above. Above the inversion, the remnant of the daytime convective boundary layer, now called the residual layer, may persist, bounded at its top by the remnant of the daytime entrainment zone, now called the capping inversion.

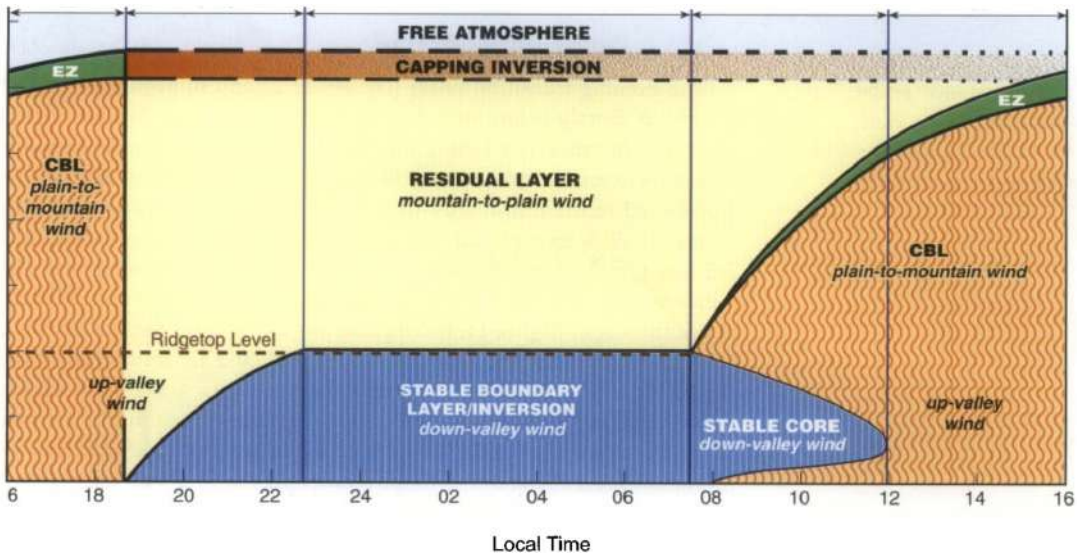

Figure 1.8: *Daily cycle of temperature and wind structure of a 500 m deep valley cross-section, with valley wind system and plain-to-mountain wind system. Although the general evolution of mountain winds depicted in this schematic diagram applies to the particular topographic configuration studied in this thesis, the stable layer does not reach the ridge-top level in the real case because the valley is too shallow and wide with respect to the ideal case of the figure. (Whiteman, 2000)*

- The reversal of slope winds from down to up identifies the *morning transition*, just after sunrise (The morning transition will be analysed in details in section 1.3.4.4). Incoming solar radiation warms the ground and erodes temperature inversion from below until its complete depletion. The air over the slopes, now warmer than the air over the center of the valley at the same height, rises up the slopes, creating upslope flows. Convective currents that rise from the heated valley floor and slopes entrain air from the base of the inversion into a growing CBL. As more and more air is removed from the base of the stable core and carried up the sidewalls, the top of the stable core sinks. This subsidence produce warming and causes the along-valley pressure gradient to reverse, letting up-valley winds replace the nighttime down-valley winds. The transition ends when the stable core is finally destroyed and up-valley winds prevail.

- The diurnal insolation dominates the *daytime phase*, when an unstable CBL develops

from the valley floor, reaching the sidewalls and the above-valley atmosphere, thus coupling the valley air with the atmosphere above. Air from the free atmosphere is incorporated into the growing CBL through the entrainment zone at its top. Mixing within the convective boundary layer produces fairly uniform profile of both wind speeds and temperature throughout the layer.

1.3.1 Variations in the Surface Energy Budget Affecting Mountain Winds

Due to the complexity of mountain topography, there are almost infinitely possible terrain configurations with as many surface energy budget and specific microclimate ecosystems.

Sensible heat is a major part of surface energy budget and is responsible for the creation of significant temperature contrast near the surface. When this contrasts take place on mountainous area, strong and well formed diurnal winds can develops. The strongest mountain wind systems are generated in dry areas (i.e., small latent heat flux) at high altitude with considerable sun exposure and strong longwave radiation loss at night. Therefore the factors modifying the mountain wind system characteristics can be classified in seasonal factors, such as the variation of solar declination angle, soil composition and ground vegetation, short-term factors (for time-scale from hours to some days), such as cloud cover and precipitation (soil water content), and local factor, namely inclination angle of the slope and the consequent shadows cast by surrounding terrain (Whiteman, 2000).

The position of the sun in the sky, which is described by the variation of the azimuth angle during the day and by the declination angle during the year, together with the inclinations angle of the slope and the resultant ridge shadow determines the times of sunrise and sunset and thus the times of initiation of up-slope and down-slope flows (i.e.morning and evening transition). A west facing slope, especially steep slopes that are shaded by ridges, may experience a significant delay in the initiation of upslope flow (Whiteman, 2000).

If soil moisture increases due to precipitation, much of the daytime net all-wave radiation is used to evaporate water, leaving little energy for sensible heat flux. Without

strong upward sensible heat flux, strong horizontal temperature contrasts do not form and diurnal mountain winds are weak. In climates where there are seasonal changes in ground cover, there are also seasonal changes in the strength of diurnal mountain wind systems, due to variation in evapotranspiration and surface albedo. The former has an impact on the sensible heat flux while the latter influence the net radiation term of the budget. Snow cover decreases the net all-wave radiation at the surface because the high albedo of snow results in a large portion of solar radiation being reflected back into space. Temperature contrasts during the day are thus reduced and the winds over snow-covered surface are weak. At night, the high emissivity of the snow enhances long- wave radiation losses. The cooling of the snow surface and the atmosphere just above is consequently enhanced, producing strong temperature contrast and hence strong wind. An evergreen forest is a good absorber of sunlight and when the layer of air above the forest is heated by the up- ward sensible heat flux from the trees, it produces upslope flows above the forest canopy. If below the forest canopy the slope is covered by snow, it produces a downslope flow during all the day, because the ground is cooler than the top of the forest (Whiteman, 2000)

Very short-term variations in the surface energy budget, caused for example by the presence of cumulus clouds obscuring the sun or reducing the nocturnal outgoing longwave radiation (i.e., weakening surface temperature contrasts), can cause slope flows to blow intermittently at a given site.

1.3.2 The Slope Wind System

The slope wind system is the lower branch of a closed circulation that arises from thermally driven pressure gradient between the air above a sloping surface of a mountain and the air at the same level above the center of the nearby valley. It consists in an upslope flow during the day and a reversal downslope flow during night, since it experiences a daily cycle. The former is also referred to as the *anabatic* wind while the latter is called *katabatic*. The strongest temperature contrast occur at the slope ground, although wind speed peak a few meters above the sloping terrain because of frictional drag at the surface. Slope winds are a small-scale flow hence they are not affected by Coriolis forces (Zardi and Whiteman, 2013). In figure 1.9 are shown the typical values and profiles of wind

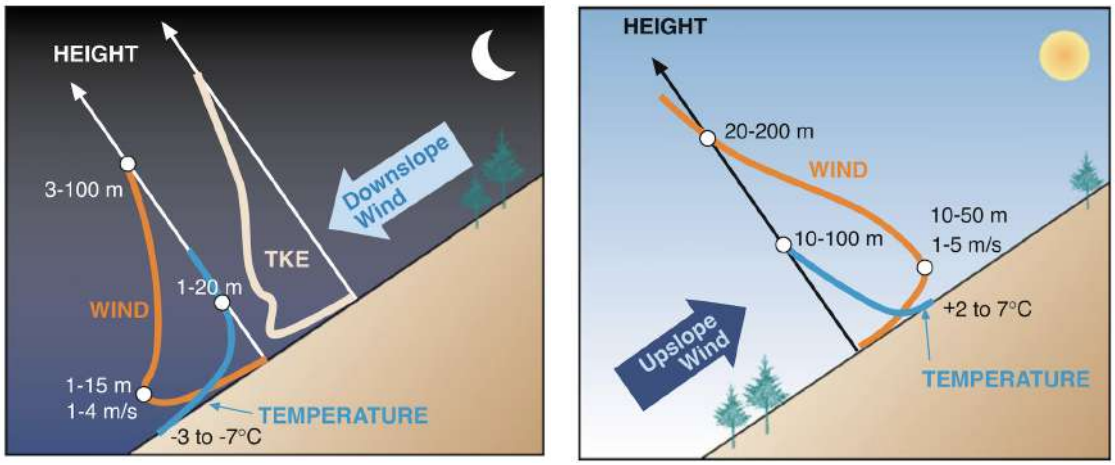

(a) (b)

Figure 1.9: *Schematic representation of (**a**) downslope and (**b**) upslope winds. Typical values for temperature contrasts (deficit or excess) and relatives profile depth, slope flow strengths and depth are shown. In (**a**) there is also the TKE profile from Skyllingstad, 2003. (Zardi and Whiteman, 2013)*

speed and temperature for mid-latitude slope flows, at a fully developed and steady state (Zardi and Whiteman, 2013). Figure 1.9(a) shows a surface temperature deficit from -3°C to -7°C with respect to the temperature at the top of the inversion layer, which may extend from 1 m to 20 m AGL. The depth of the downslope flow layer varies from 3 m to 100 m AGL, with a speed maximum of 1-4 $\mathrm{m\,s^{-1}}$ that occurs at height of 1-15 m AGL. The strength and vertical scale of slope flow increase with downslope distance due to cooling at the surface and entrainment of ambient air at the top of the flow. During the evening, the inversion becomes deeper and the maximum downslope wind speed,the height of the wind maximum, and the total depth of downslope flow normally increase. Usually, the depth of the temperature inversion layer is about 5% of the vertical drop from the top of the slope (Horst and Doran, 1986). Downslope flow often becomes weak and intermittent during the night as the inversion builds up in the valley and as the overriding down-valley flow increases in strength and expand to fill more of the valley cross section (Whiteman and Zhong, 2008).

Upslope flows characteristics values are shown in figure 1.9(b). Typical flow depth are 20-200 m AGL with the maximum wind speed of 1-5 m/s at 10-50 m AGL. Temperature

excess near the ground varies from 2 °C to 7 °C with respect to the temperature at 10-100 m (Zardi and Whiteman, 2013). Upslope winds are generally accompanied with advection of cold air from the valley. The flow depth increase with distance up the slope and with time because winds converge towards the mountain crests while in the valleys the compensating subsidence leads to smaller growth rates of the CBL (Kossmann et al., 1998).

1.3.2.1 Upslope Flow

Upslope flows develop along a layer over a heated slope, confined by highly stable air formed above the slope during night. The daytime boundary layer above a slope differs from that on flat surface because it is a convective-advective boundary layer (Zardi and Whiteman, 2013). Nonuniform heating by solar radiation generates inhomogeneities in the turbulent heat flux at the surface due to different steepness and orientation of the slopes and due to the shade of surrounding terrain elevation. The result is an along-slope gradient in potential temperature in the slope wind layer. The upslope winds are therefore characterized by advection of cold air from the valley inversion, which leads to a reduction in the heating rate near the ground, hence limiting the intensity of the daytime slope wind circulation. (De Wekker and Kossmann, 2015). The upward movement of cold air advected over the crests also implies the formation of a stable layer near the top of the slope wind layer (Kossmann et al., 1998).

Throughout the morning, increased heat flux reinforces the upslope flow strength and depth, resulting in a non-stationary flow with the possible occurrence of sudden jumps to higher or lower depth values (De Wekker and Kossmann, 2015).

During the course of the afternoon, slope flows become less well-defined and are often overpowered by the up-valley or regional winds due to downward turbulent momentum transfer.

After sunset, surface cooling leads to the formation of downslope winds in the developing surface inversion layer, while up-valley and/or regional winds still prevail aloft in a residual layer. Later, up-valley winds will cease and may be replaced by down-valley winds (De Wekker and Kossmann, 2015).

1.3.2.2 Downslope Flow

Cooling of the ground and adjacent air layer during the evening causes the upslope flow to reverse. Theoretical models and laboratory observation describe the transition from up to downslope through the formation of a stagnant frontal region.

While flowing upslope, air parcels at various heights cool and gradually decrease their buoyancy and when their upslope inertia become too feeble, they begin to stagnate. The upper air layers still flow upslope, since they have higher inertia, thus giving a frontal shape to the stagnation line. Relatively warmer air near the ground can be incorporated into the overturning frontal motion and rapidly mixed. This frontal region is non-stationary and migrates downslope, causing the cool air layer behind the front to drain, initiating the katabatic flow. Aloft the newborn katabatic flow, the upslope flow can persist for some time due to the inertia of air parcels at greater heights.

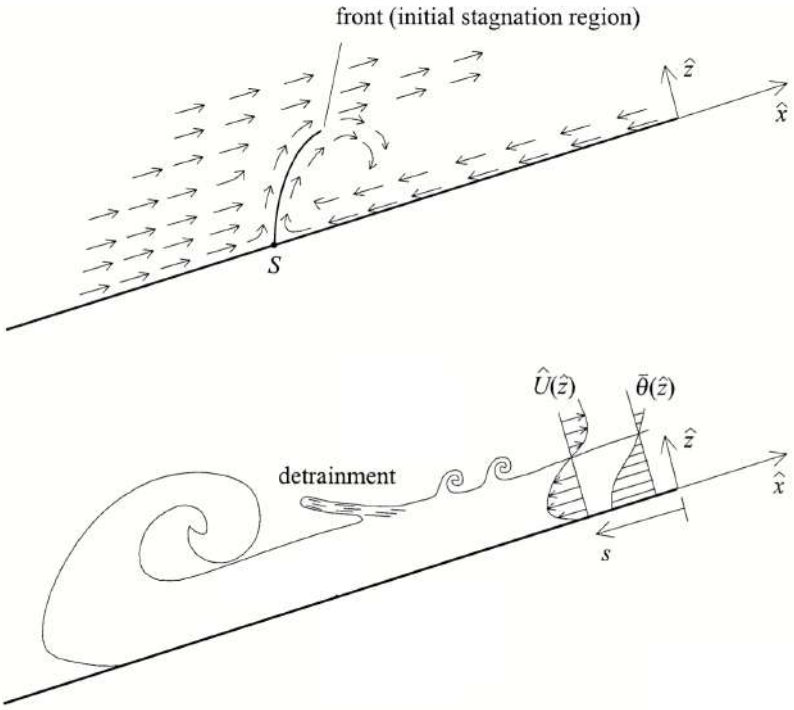

Figure 1.10: *Schematic of slope flows: (up) transition from upslope to downslope flow (S indicates the stagnation region); (down) downslope flow, including the downslope propagating frontal region. (Monti et al., 2002)*

Although the stable stratification inhibits turbulent motions in katabatic flows, the presence of layers of different densities and velocities stacked one above and the generation of large velocity shears causes the flow to be unstable and break down into turbulence, at least intermittently (Monti et al., 2002).

The turbulence structure associated with the jet-like downslope flow has a distinctive structure. The vertical wind shear is positive below the jet, disappears at the height of the jet and is negative above the jet. This vertical configuration produces TKE profiles (Fig.1.9(a)) with a maximum near the surface and a local minimum at the height of the wind maximum. Above it, TKE is highly dependent on the speed and direction of the ambient wind (Zardi and Whiteman, 2013).

If a continuous source of cold air were introduced at the top of a slope the downslope flow would be stronger on steeper slopes where the along-slope component of the gravity vector is maximized. The air moves down if it has negative buoyancy with respect to the ambient environment. As it moves down the slope, the air is heated adiabatically at 9.8° C/ km. To continue its descent it must be continuously cooled by a downward sensible heat flux to the cold underlying surface. The faster the flow, the lower the rate of cooling per unit mass of flow. On low angle slopes, the air travels a greater horizontal distance along a slope to descend the same vertical distance compared to a steeper slope. The air loses heat through downward sensible heat flux along its entire trajectory, which is longer on a shallow slope than on a steep slope(Zardi and Whiteman, 2013).

Slope flows will not form on horizontal surfaces, where radiative loss to the sky and downward sensible heat flux occur but the along-surface component of the gravity vector is zero. At the other limit, a vertical surface will have a strong component of the gravity vector along the slope, but cannot radiate well to the sky because of its extreme inclination. In this situation, the rate of cooling of the flow to the underlying surface would be small because of the small distance that the air would travel to lose a unit of altitude. The strongest downslope flows will thus develop on slopes of intermediate angle where there is a combination of good outgoing longwave radiative loss to the sky that drives a slope-normal sensible heat flux and a component of the gravity vector acting along the slope. Slope flows are often stronger in the early evening when the ambient stability is weak. Downslope flows accelerate with downslope distance while increasing their depth as additional mass is entrained into the flowing layer at its upper boundary (Zardi and Whiteman, 2013).

1.3.3 Valley Wind System

Diurnal valley winds are thermally driven winds that blow along the axis of a valley. They experience a daily cycle, with up-valley flows during daytime and down-valley flows during nighttime. Usually they have weak to moderate wind speed, frequently in the range from 3 to 10 m/s. Valley winds are the lower branch of a closed circulation that is formed when there is an horizontal temperature gradient along the valley axis or between the valley and the adjacent plain. The upper branch of this closed circulation is unconfined by topography and thus it has a larger horizontal extent, is generally quite weak and blows in the opposite direction with respect to the valley winds. Unlike slope winds, valley winds are not primarily a function of the slope of the underlying valley floor. In fact, they have been observed even in valleys with horizontal floors. Instead, they depend on other geometrical factors, such as the shape and aspect of the valley cross-section and their along-valley variations, including tributaries.

The evening reversal of the daytime up-valley wind begins in late afternoon or early evening when the daytime wind system gradually lose strength, over several hours. Once the sensible heat flux reverses on the sidewalls or in the shadowed parts of the valley,air parcels at various heights cool and gradually decrease their buoyancy (Monti et al., 2002). Then downslope flows begin, transferring cold air into the valley. Advection rebalances temperature along the valley axis, causing a decrease in the along-valley pressure gradient and a gradual loss of strength of the daytime up-valley winds. As the valley atmosphere cools, the horizontal pressure gradient between the valley and adjacent plain reverses and a down-valley flow begins (Fig. 1.11, lower panel). The valley wind reversal lags that of the slope flows because the large mass of the valley atmosphere must be cooled before the pressure gradient can reverse. Valley floor cools first, allowing formation of a temperature inversion. Cooling then propagates upwards, but the coldest temperature are formed at the valley floor.

The morning reversal of the down-valley wind, which occurs after sunrise, similarly requires a reversal of the valley-plain pressure gradient as the valley atmosphere warms (Fig. 1.11, upper panel). The reversal occurs several hours after upslope flows are initiated when the heat transfer processes become effective in warming the entire valley atmosphere.

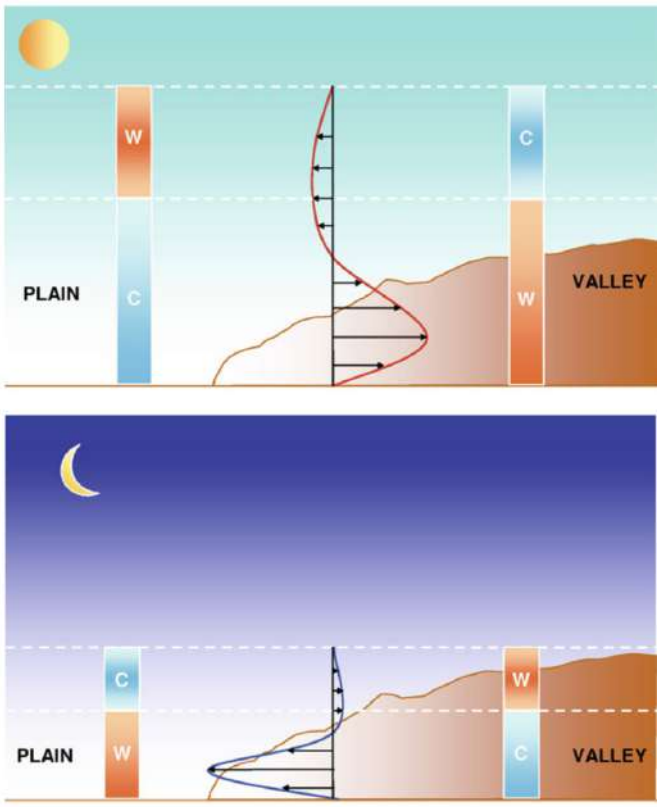

Figure 1.11: *Idealized picture of the development of daytime up-valley winds (upper panel) and nighttime down-valley winds (lower panel) with their vertical profile in a valley-plain system with a horizontal floor. The columns of hair over the valley floor and over the plain represent the horizontal temperature gradient between the tow areas. At the tops of the columns, the free atmosphere is assumed to be unperturbed (Adapted from Whiteman, 2000). (Zardi and Whiteman, 2013)*

The warmer temperatures during daytime and colder temperatures during nighttime in the valley atmosphere compared to the atmosphere over the adjacent plain, or farther down the valley are mainly caused by two factors. First, under weak synoptic conditions, the valley atmosphere is protected by the surrounding topography from mass and heat exchange with the atmosphere above the valley so that heating and cooling will be more effective. A second, more important, factor called "valley volume effect" or "topographic amplification factor"(TAF) attributes the faster heating and cooling of a valley compared with an adjacent plain for an equal energy input to the smaller air volume. The concept is that the daily temperature range in the valley will be amplified by the smaller mass of air that is heated or cooled within the confined valley volume. The higher mean temperature inside the valley during daytime causes a pressure gradient to develop between valley and plain that drives an up-valley wind. The lower mean temperature and higher pressure in the valley during nighttime drive a down-valley wind (Zardi and Whiteman, 2013).

1.3.4 Coupling Between Slope and Valley Wind Systems

The dynamics of diurnal valley winds results from the combination of slope flows on the sidewalls and boundary layer processes on and above the valley floor. As a consequence, turbulent processes associated with valley winds occur on different space scales (height above the slope, slope length, boundary layer depth over the valley floor, valley width) and time scales (hour, morning, afternoon, daytime, nighttime). A high site-to-site variability must be hence considered.

The evolution of the coupled slope and valley systems during a typical day progresses through four distinct phases, described below (Zardi and Whiteman, 2013).

1.3.4.1 Daytime Phase

After the final destruction of the stable nighttime boundary layer due to daytime heating, the valley atmosphere becomes coupled with the atmosphere above the valley and along the sidewalls (Fig. 1.8). By mid-morning, the air on the valley floor is warm enough to produce a pressure gradient which makes air to flow up the valley axis. Convective currents rise from the valley floor and quickly extend up and over the valley ridges. The convective boundary layer become deeper and incorporates air from the free atmosphere through the entrainment zone. Wind speeds increase as the convective boundary layer grows to higher altitudes and encounters stronger winds. Wind speeds, both in the valley and over the plain, usually peak in late afternoon when the convective boundary layer reaches its maximum depth. The extra heating in the valley, due to the TAF and the partially enclosure of the valley air by the surrounding, invigorates the convection from the valley but this effect decreases as the mixed layer grows deeper above the ridges (Zardi and Whiteman, 2013)..

If winds aloft are light, diurnal mountain winds continue to blow up the valley and the sidewalls. If winds aloft are moderate to strong, they can overpower the diurnal mountain winds.

The daytime period ends with the onset of the evening transition period shortly before sunset, and the cycle begins again (Whiteman, 2000)

1.3.4.2 Evening Transition

The evening transition phase (Fig. 1.8) begins in the late afternoon shortly before sunset, starting usually in areas of the valley that are shadowed by terrain. The surface energy budget reverse sign when outgoing longwave radiation first exceeds incoming shortwave radiation. The ground begins to cool and a downward turbulent sensible heat flux removes heat from the lower atmosphere, producing a shallow layer of cool, stable air over the valley and the sidewalls. Because the air above the slopes is colder than the ambient air over the valley center, it becomes negatively buoyant and slides down the slopes in a shallow layer immediately above the slopes. The cold air slides along the steepest drop of a slope and accumulates over the valley center, building up a valley temperature inversion. The coldest air is found both on the valley floor and over the ridge tops, and as a result the warmest air forms a belt on top of temperature inversion which extends part way over the sidewalls.

The convergence of downslope flows over the valley center is compensated by rising motion over the valley center. This upward cold advection allows the inversion to grow deeper and the cooling to rise higher (on clear nights often grows to 500 m within 3-5 hours after sunset) (Whiteman, 2000).

Daytime up-valley winds continue to blow for several hours after the energy budget reversal because of inertial effects and because it takes some time for the cooling over the valley slopes to be transferred to the entire valley volume through compensatory rising motions and other processes. The temporary post-sunset continuance of the up-valley flow generates shear that increases turbulent sensible heat flux in the surface layer (Zardi and Whiteman, 2013). The wind reverse occurs as soon as all the air along the valley cross-section becomes colder than the air over the adjacent plain, also reversing the pressure gradient. Down-valley flows first appear in the ground-base stable layer. As the inversion layer deepens, the down-valley flow also deepens and increases in strength.

The evening transition ends when the growth of the inversion slows and the residual air layer above, previously flowing up-valley, is overcome by down-valley winds through the entire valley depth.

Downslope flows, which characterize the onset of the evening transition period, gradually decay during the stable layer growth and reinforcement. They continue on the

upper sidewalls of the valley above the rising stable layer, but leave the sidewall and converge into the main valley volume once encountering it.

During the reversal to down-valley winds, strong radiative cooling occurs along the inhomogeneous valley floor and slopes, resulting in the formation of shallow cold air layers which preferentially fill low spots on the valley floor. During this period winds are light and variable and the surface- based inversion often strengthens. The formation of the cold air layer on the floor and sidewalls tends to decouple the valley winds from the friction of the surface. The decoupling can sometimes generates acceleration in valley winds, increasing shear and mixing and causing temporary evening temperature rising. This may cause repeatedly decays and reforms of the cold air layer together with oscillations in the valley and slopes winds (Zardi and Whiteman, 2013).

1.3.4.3 Nighttime Phase

During the night (Fig. 1.8) down-valley winds prevail within a fully formed valley temperature inversion. The inversion depth remains essentially constant and is approximately equal to the valley depth. Shallower valleys in climates with strong nighttime cooling often have inversions that extend above the adjacent ridge tops, whereas deeper valleys have inversions that do not completely fill the valley. In moist or cloud-covered valleys, the nighttime inversions are often much shallower than the valley, with the inversion depth often corresponding to the top of a fog, haze, or cloud bank (Whiteman, 2000).

During this phase, the downslope flows weakened and became intermittent late in the night as the down- valley flow strengthened and downward momentum transport turned the slope flow into the down-valley direction and suppressed its strength and depth. Compensatory flow rising from the valley because of the strong cooling is reduce. Because the down-valley flow is at right angles to the underlying downslope flow significant directional shear occurs in the slope flow through heights that roughly coincide with the depth of the temperature deficit layer (Whiteman and Zhong, 2008).

The vertical wind profile takes a jet-like shape with the wind maximum displaced tens or hundreds of meters above the floor and with the peak wind over the valley center, where frictional influence of the sidewalls is minimized. The nighttime down-valley current is sometimes called a *down-valley jet* (DVJ). In some cases, downward mixing causes

abrupt warming at the jet low levels and others periodic phenomena associated with vertical transport of heat such as gravity waves, Kelvin-Helmholtz waves and pulse in the jet strength (Zardi and Whiteman, 2013). Above the inversion, the remnant of the daytime convective boundary layer (i.e., the residual layer) may persist, bounded at its top by the capping inversion.

Nocturnal drainage flow are strongly affected by local topography, given that they fit flush against the ground and thus display a very irregular behavior.

1.3.4.4 Morning Transition

The morning transition period (Fig. 1.8) begins shortly after sunrise. The sun rising over the mountain ridges initiates the heating process of the surface: incoming solar radiation exceeds longwave radiation loss and the surface energy budget reverses on the valley sidewalls. Sensible heat is transferred from the ground to the air until the ground-base inversion that fills the valley at night breaks-up. There is one key difference between valleys and plains inversion break-up. The plains are heated form below by the upward sensible heat flux which allows the CBL to grow up. Valleys, on the other hand, are heated in many different ways. Whiteman (Whiteman, 1982) observed three different pattern of temperature inversion destruction. In the widest valley the inversion destruction approximate that over flat terrain, in which the nocturnal inversion is destroyed after sunrise by the upward growth from the ground of a warm CBL. The second pattern, observed in snow-covered valleys, is characterized by a growth of the CBL until a depth of 25-50 m. Then the top of the nocturnal inversion descend into the valley and is destroyed by the subsidence warming. The third mechanism, for valley without snow cover, is a more general case of the previous pattern and is the most frequently observed in the Whiteman's field experiments. In this pattern, the inversion is destroyed by two processes: the continuous upward growth from the valley floor of a warm CBL ad the continuous descent of the top of the nocturnal temperature inversion, that is the subsidence. However, the development of warm CBL over the valley floor after the direct sunlight is the common element of all three patterns.

Other patterns were found using a laboratory experiment in which an idealized V-shaped valley with negligible width is heated uniformly from below (Princevac and

Fernando, 2008). In the first one, starting from a weak stratification, the destruction of the descending stable core occurs by convective turbulence with a flow dominated by upslope advection, accompanied by a subsidence in the middle of the valley. This pattern is similar to the Whiteman's third pattern, even though in Whiteman's mechanism the top of the density inversion remains stationary although entrainment progresses causing the convective mixed layer to grow. The second one analyzes the destruction of a strong stratification, which occurs via a dominant horizontal intrusion at mid-depth and its entrainment into the bottom convective layer.

The warming effect of compensatory sinking motions decreases in wider valleys while in narrow valleys, the stable core inhibits the growth of a convective boundary layer above the valley floor and sidewalls. The time required to destroy the inversions depends also on inversion strength at sunrise and on the rate of input of sensible heat from the valley surfaces after sunrise (Whiteman, 1982), which varies with season and snow cover.

The morning transition period ends when the stable core is completely eroded, the valley air is completely heated and the pressure gradient between valley and plain revers, causing up-valley winds to replace down-valley winds.

1.3.5 Diurnal Progression of Wind Directions on Valley Sidewalls

A particular sequence of wind directions on the valley sidewalls results from the daily timeline of slope and valley winds. The winds shift from upslope just after sunrise, to up-valley during daytime, to downslope at sunset, and then to down-valley during the night. On the right sidewall of a valley (as viewed from the head of a valley), the phasing results in a clockwise turning of the winds with time; on the left sidewall, the winds turn counterclockwise with time (Whiteman, 2000).

Slopes winds reverse direction near sunrise and sunset whereas along-valley winds require warming or cooling a large volume of air along the valley. The wider or deeper a valley, the greater the volume of air in the valley and the greater the delay in along-valley wind reversal.

Chapter 2

The MATERHORN: methods and data analysis

The data collected around the Granite Mountain at Dugway Proving Ground in Utah during the Mountain Terrain Atmospheric Modeling and Observations (MATERHORN) field program (Fernando et al., 2015) are use in this thesis to study the evolution of the morning and the evening transition over complex terrain. In the following sections a detailed overview of the field campaign and of the data analysis techniques are presented.

2.1 The MATERHORN Program

The MATERHORN Program was designed to investigate complex-terrain meteorology over a wide range of scales, topographic features, and driving mechanisms. This ambitious program has been carried out with the help of numerous experts, thanks to the collaboration of numerous experts, mainly from the following universities: the University of Notre Dame (UND; lead); University of California, Berkeley (UCB); Naval Postgraduate School (NPS); University of Utah (UU); and University of Virginia (UVA).

The four component of the MATERHORN program were:

- The modeling component (MATERHORN-M)
- The experimental component (MATERHORN-X)

- The technology development component (MATERHORN- T)
- The parameterization component (MATERHORN-P)

Two extensive field campaigns (MATERHORN-X) on the fall off 2012 and the spring of 2013 were conducted with high-resolution measurements, focusing on conditions dominated by thermal circulations and strong synoptic forcing. The data related to the periods in which develop the thermal circulations were used for this thesis, as will be described in the next section.

2.1.1 General Description of the Experimental Site

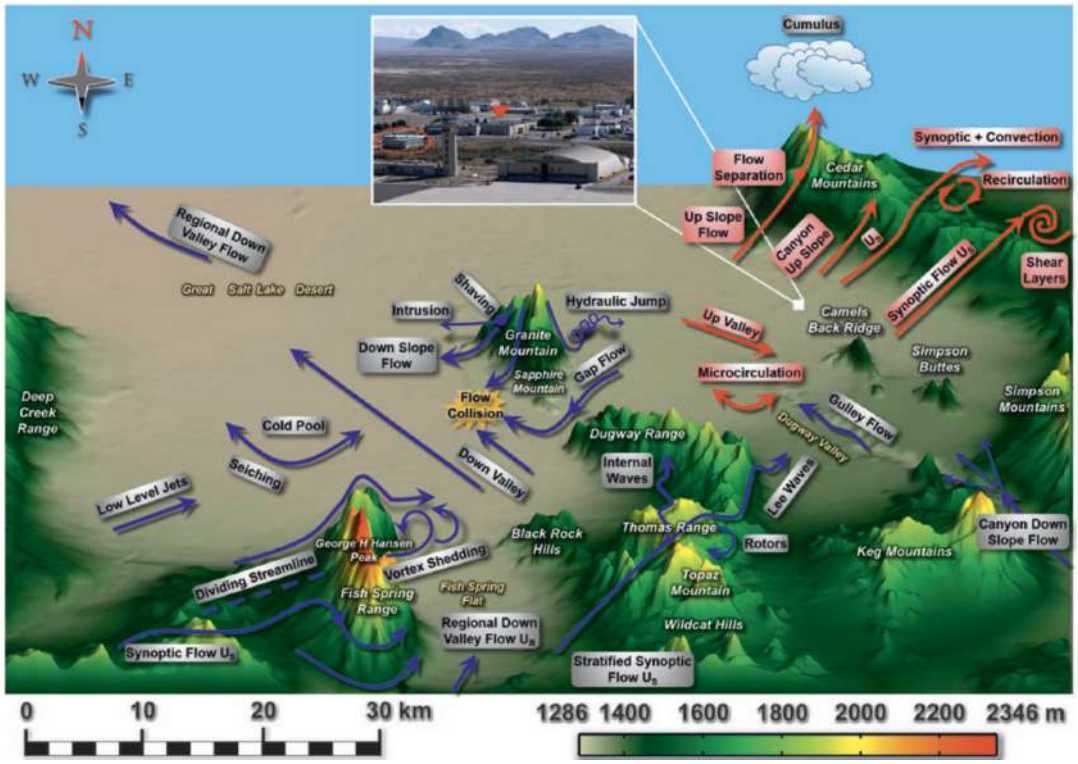

Figure 2.1: *Schematic representation of the physical processes over complex terrain on a topographic map of the DPG. Blue arrows represent nocturnal flow while red arrows represent daytime flows. The spatial and the elevation (shading) scales are shown below. (Fernando et al., 2015).*

The Granite Mountain Atmospheric Science Testbed of the U.S. Army Dugway Proving Ground (DPG) was selected as the field site. This site has the advantages of a large spatial extent, richness in mountain weather phenomena, interesting climatological regimes, distinct (but few) land-use types, an existing instrumentation network. The DPG is located about 137 km south-west of Salt Lake City, Utah. The terrain of the DPG site consists of sand dunes, salt flats and isolated hills surrounded by interconnected mountains, with sparse shrub steppe vegetation and very little human population (Hang et al., 2015).

The Granite Mountain Atmospheric Science Testbed (GMAST) is a part of the U.S. Army DPG shown in Fig.2.1. It consists of 3700 km2 of land in complex terrain, which present on the central part, a nominally isolated topographic feature, the Granite Mountain. This mountain consists of an isolated massif with an east – west aligned slope that stand on a large plain (The Dugway Valley to the east and The Playa to the west), surrounded by interconnected mountains that, in the southern part, are closer to it. The Granite Mountain is 11800 m in length, 6100 m at its widest, and has a peak elevation of 840 m above the valley floor, which itself is 1300 m above mean sea level (MSL) (Fernando et al., 2015).

The fall campaign period (25 September–31 October 2012) was characterized by quiescent, dry, fair weather periods dominated by thermal circulation and the spring campaign (1–31 May 2013) by synoptic forcing. A dry experimental run (25–30 August 2012) helped fine- tune the instrument placement and logistics. Under weak synoptic conditions (wind speed $U < 5\ \mathrm{m\,s^{-1}}$) dominated by high pressure, the characteristic winds are downslope (katabatic) and down-valley at night (blue arrows in fig. 2.1) while upslope (anabatic) and up-valley during the day (red arrows in fig. 2.1), signifying thermal circulation ((Whiteman, 2000); (Fernando, 2010); (Zardi and Whiteman, 2013)). Pure slope and valley winds are rare in nature, since they interact among themselves and with synoptic flow.

Flows that develop on either side of Granite Mountain during quiescent IOPs are driven by differential thermal forcing, for example, caused by the land surface contrast between sparsely vegetated areas to the southeast and the playa to the northwest. The intricacy of the topography and the existence of a small and a big gap in the southern part

trough which the air drain periodically, add complexity to the developing mountain-valley circulation.

2.1.2 Instrumentation

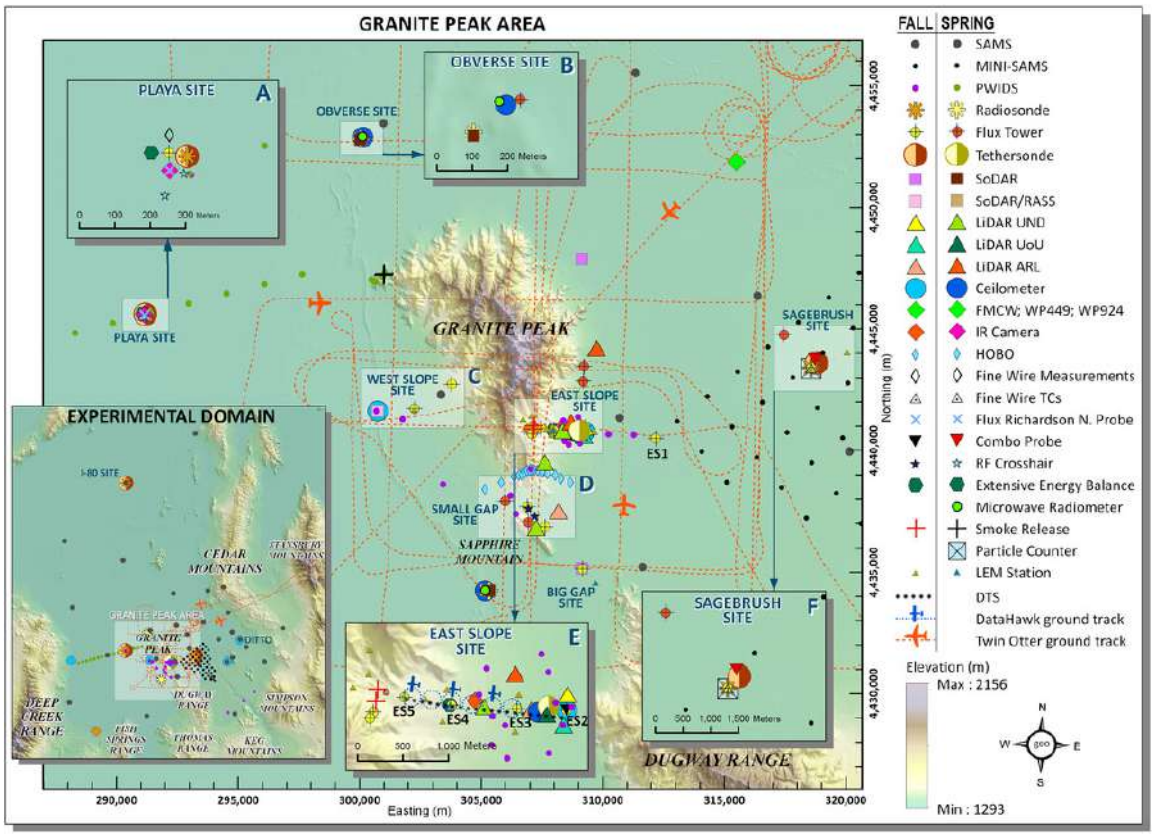

Figure 2.2: *Instrument placement during fall and spring campaigns. Insets provide details of IOSs as well as the full experimental domain (bottom-left inset). Only the additional instruments deployed (or relocated) for the spring experiment are shown under the "spring" column (Fernando et al., 2015).*

Figure 2.2 describes the instrumentation and observing locations of the MATERHORN-X. Six main intensive observing sites (IOS) were selected based on science plans and logistical constraints:

- IOS-Playa on the west of Granite Mountain, in the Great Salt Lake Desert. The area is extremely flat, smooth, and mostly devoid of vegetation. It is characterized

by high albedo and seasonally changing moisture.

- IOS-Obverse was the footprint where north/ northwesterly/northeasterly approach flow impinges on the GM
- IOS-WS (west slope) was on the western slope of GM for studies on slope flows and their interaction with synoptic, valley, and canyon flows.
- IOS-Gap was a flow exchange area covered by sparse desert shrub vegetation between west and east basins. This site covered a small gap and a big gap.
- IOS-ES (east slope) was on the eastern slope of GM. Covered by sparse desert shrub vegetation and long grasses, local slope flows played an important role at this site.
- IOS-Sagebrush was located east of the GM and centrally in the main valley. Covered by sparse desert shrub vegetation, it was highly representative of the land cover in DPG.

2.1.2.1 West Slope Instrumentation and Description

The lack of comprehensive studies on the west slope of Granite Mountain, and in general on characterization of thermal circulation of this side of the mountain, is the main reason why it has been chosen for this work.

The IOS-WS consisted of two towers (WS-1 and WS-2), a SAMS station, eight HOBOs (available only during the spring campaign), and a LEMS along the western slope of Granite Mountain for observing the interactions of synoptic and slope flows as well as characterizing the thermal circulation developing around the Granite Mountain. WS-1 and the LEMS were on the lower portion of the slope approximately 20 m above the Playa floor. The former was a 28-m tower instrumented with six levels of 3D sonics and T–RH sensors. During the fall campaign, IOS-WS hosted a sound detection and range/radio acoustic sounding system (SoDAR/RASS) , a ceilometer, and additional PWIDS. The 20-m WS-2 was located farther along the slope with five sonics, a vane anemometer, Krypton hygrometer, 12 thermocouples, and extensive surface energy budget instrumentation (Fernando et al., 2015). The two surface towers on the west slope are equipped with RM Young 81000 Ultrasonic Anemometers.

The west slope instruments actually used in this work are shown in figure 2.3.

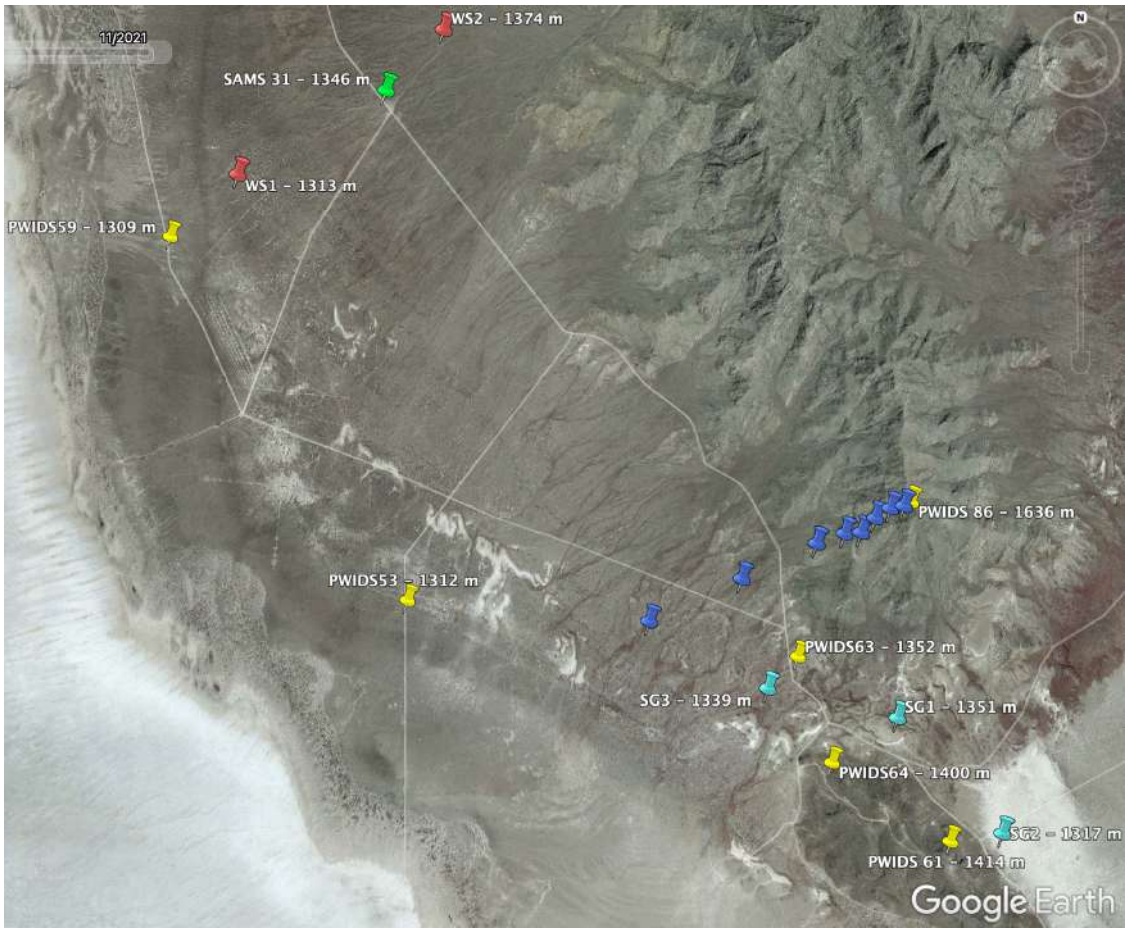

Figure 2.3: *Position on the west slope of the instruments actually used in this thesis. Given the very limited distance among the HOBO's (blue placeholders), their names are hidden due to overlap problems. (Copyright Google Earth Pro.)*

The topography nearby the WS2 (the tower that is farther up the slope) is composed in the eastern part by a small inclined valley bounded by higher terrain (Figure 2.4). A very narrow valley, similar to a canyon, slices trough very steep peaks to the northeast. Other smaller creeks are found nearby. The steepest part of the west slope is located east-northeast of the WS2. The slope width increases with distance from the peak, while the slope angle decreases from $\approx 3^\circ$ - 4° near the WS2 to $\approx 0.5^\circ$ approaching the WS1. The distance from the steepest part of the slope and the location of the WS1, where the valley widens, involves several differences between it and the WS2, as we will show in

chapter 4.

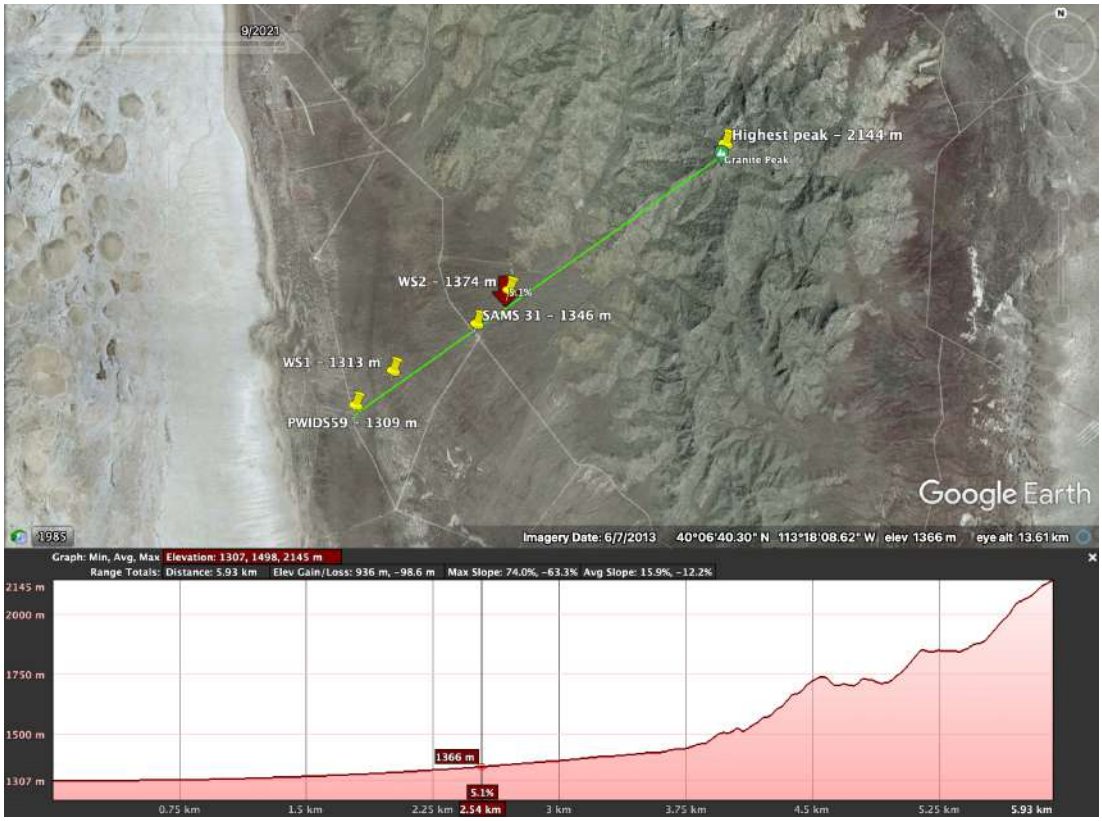

Figure 2.4: *Google Earth Landsat Image/Copernicus showing a transect of the instrumented west slope with an elevation profile and inclination value near the WS2. The indication "Highest peak" refers only to the highest elevation of the transect, but nonetheless the highest point of Granite Mountain is 2160 m in the very near. (Copyright Google Earth Pro.)*

2.2 Intensive Observing Period: Selection and Synoptic conditions

Both the spring and fall campaign included 10 Intense Observation Periods (IOPs) during which all instruments were operated in coordination, producing a large amount of data. The IOPs were classified according to the synoptic wind speed (Fig. 2.5), and the IOP days were chosen a day earlier considering weather forecast. The data will be

released to the scientific community 3 years after the end of each experiment. The IOPs were classified according to the wind sped U at 700 hPa:

- *quiescent* when $U < 5\ \mathrm{m\,s^{-1}}$
- *moderate* when $5 < U < 10\ \mathrm{m\,s^{-1}}$
- *transitional* when $U > 10\ \mathrm{m\,s^{-1}}$

Fall 2012 IOPs		
IOP	**Period**	**Type**
0	1400 MDT 25 Sep–1400 MDT 26 Sep	Quiescent
1	1400 MDT 28 Sep–1400 MDT 29 Sep	Quiescent
2	1400 MDT 1 Oct–1400 MDT 2 Oct	Quiescent
3	0200 MDT 3 Oct–0200 MDT 4 Oct	Transitional
4	1400 MDT 6 Oct–1400 MDT 7 Oct	Moderate
5	1400 MDT 9 Oct–1400 MDT 10 Oct	Transitional (quiescent–moderate)
6	0200 MDT 14 Oct–0200 MDT 15 Oct	Quiescent
7	1200 MDT 17 Oct–2000 MDT 17 Oct	Transitional (quiescent–moderate)
8	0500 MDT 18 Oct –1200 MDT 19 Oct	Quiescent
9	1400 MDT 20 Oct –1400 MDT 21 Oct	Moderate

Spring 2013 IOPs		
IOP	**Period**	**Type**
1	1400 MDT 1 May–1400 MDT 2 May	Transitional (moderate–quiescent)
2	1400 MDT 4 May–1400 MDT 5 May	Moderate
3	0500–1700 MDT 7 May	Moderate
4	1400 MDT 11 May–1400 MDT 12 May	Quiescent
5	1200 MDT 13 May–1200 MDT 14 May	Transitional (moderate–quiescent)
6	1200 MDT 16 May–1200 MDT 17 May	Transitional (moderate–quiescent)
7	1715 MDT 20 May–1400 MDT 21 May	Quiescent
8	1400 MDT 22 May–1400 MDT 23 May	Moderate
9	1000 MDT 25 May–1000 MDT 26 May	Moderate
10	1400 MDT 30 May–1000 MDT 31 May	Moderate

Figure 2.5: *IOPs days classification according to the synoptic wind speed. Dates and time of each IOPs are also shown (Fernando et al., 2015).*

In order to investigate the thermal circulation of the west slope and characterise the morning and the evening transition, we chose to consider *quiescent* IOPs, during which the synoptic forcing was very weak or even absent.

2.3 Data Processing

The methods and the analysis used during the data processing are presented in this section.

2.3.1 Sonic Anemometer Orientation

Looking at the orientation of the sonic anemometer on the flux towers, it is necessary to determine the angle between the instrument wind coordinates $(u_{inst}, v_{inst}, w_{inst})$ and the geographic wind coordinate system $(u_{geo}, v_{geo}, w_{geo})$. In particular, we have to know the angle with respect to the North of the $+v_{inst}$ direction, in order to convert instrument in geographic coordinates. We call this angle v_{az}. It is assumed that all trig functions use or return angles in radians. Angles are nevertheless converted to degrees for easier understanding: radians are converted to degrees by multiplying $DperR = \frac{180}{\pi}$ and degrees are converted to radians by multiplying $RperD = \frac{\pi}{180}$.

The measurement of wind vector components are relative to the orientation of the sonic array on the sonic anemometer. We assume that the sonic anemometers are level, so that $w_{inst} = w_{geo}$. In the particular case of RM Young 81000 Ultrasonic Anemometer, $+u_{inst}$ represents wind blowing from the East whereas $+v_{inst}$ is wind from North. The geographic wind coordinates however assume a positive u_{geo} component for wind blowing to the East and $+v_{geo}$ represents wind to the North, and so this is a right handed coordinate system with respect to an upward $+w_{geo}$. Thereby the instrument coordinate system is rotated 180 degrees clockwise (or -180 degrees counterclockwise, but we choose $v_{az} = 180°$). The following formulas hold:

$$u_{geo} = u_{inst} \cdot \cos(v_{az} \cdot RperD) + V_{inst} \cdot \sin(vaz \cdot RperD) \tag{2.1}$$

$$v_{geo} = -u_{inst} \cdot \sin(v_{az} \cdot RperD) + V_{inst} \cdot \cos(vaz \cdot RperD) \tag{2.2}$$

$$Spd = \sqrt{u_{geo}^2 + v_{geo}^2 + w_{geo}^2} \tag{2.3}$$

$$Dir_{geo} = atan2(-u_{geo}, -v_{geo}) \cdot DperR \tag{2.4}$$

The $atan2(y, x)$ returns the arctangent of y/x in the range $[-\pi, \pi]$ radians (-180 to 180 degrees) and thus we have to add on 360 degrees to each negative direction data so as to obtain positive direction values only (from 0 deg to 360 deg). Moreover the value 360 is forced to zero, so we do not have two different values corresponding to the North.

Choosing 5 degrees width intervals to sort through wind direction data, we obtain 72 intervals of the same width. The bin edges are set out as follows:

$$edges(k) \leq Dir_{geo}(i) < edges(k+1) \tag{2.5}$$

Wind velocity data are sampled at 20 Hz and the time interval chosen to compute the wind direction is 30 minutes. Wind direction in each half hour is determined through the most frequently occurring value among the wind direction data in each interval , i.e. the mode of each half hour data range.

2.3.2 Double rotations

Some errors can occur while measuring velocities and fluxes over complex terrain because the reference frame in which the measurement are taken is different from the reference frame of the equations. In this thesis the reference frame chosen is that of the streamline coordinates (i.e., flow coordinates), in which the x axis is in the direction of the local mean wind vector, and y and z are in the directions of the binormal and principal normal to the streamline. Therefore measurement taken in the instrument reference frame need to be rotate after they have been collected. To rotate wind vector from the instrument reference frame to the streamline reference frame three mathematical transformation are required (Kaimal and Finnigan, 1994).

Assuming that digitally sampled velocity data are recorded in the instrument's rectangular Cartesian reference frame, denoted by x_1, y_1, z_1, the velocity component in this frame are:

$$u_1 = u_{inst}, v_1 = v_{inst}, w_1 = w_{inst} \tag{2.6}$$

Firstly, we determine the average wind vector $\vec{\bar{u}} = (\bar{u}_1, \bar{v}_1, \bar{w}_1)$ from the time series of the data to be rotated, i.e. the velocity components. The mean vector depends upon both the averaging time chosen and the spatial resolution of the instrument. In this case, as we already said, we choose half-hour averages among wind velocity data, that are sampled at 20 Hz. The first transformation swings the x_1, y_1 axes around z_1 to produce a new set of axes (x_2, y_2, z_2) with x_2 in the plane spanned by $\vec{\bar{u}}$ and z_1 (Fig. 4.1).

$$\begin{aligned} u_2 &= u_1 cos\vartheta + v_1 sin\vartheta \\ v_2 &= -u_1 sin\vartheta + v_1 cos\vartheta \\ w_2 &= w_1 \end{aligned} \tag{2.7}$$

$\vartheta = tan^{-1}\left(\frac{\bar{v}_1}{\bar{u}_1}\right)$. This rotation forces $\bar{v}_2 = 0$, but the vertical component is unaffected.

The second rotation swings x_2 and z_2 about y_2 into new directions x_3, y_3, z_3, so x_3 now points along the mean wind direction (Figure 2.6). the new velocity components are:

$$\begin{aligned} u_3 &= u_2 cos\phi + w_2 sin\phi \\ v_3 &= v_2 \\ w_3 &= -u_2 sin\phi + w_2 cos\phi \end{aligned} \tag{2.8}$$

where $\phi = tan^{-1}\left(\frac{\bar{w}_2}{\bar{u}_2}\right)$.

At this point the x_3 axis points in the direction of the mean wind vector, but the directions of the y_3 and z_3 axes depend on the initial choice of instrument alignment.

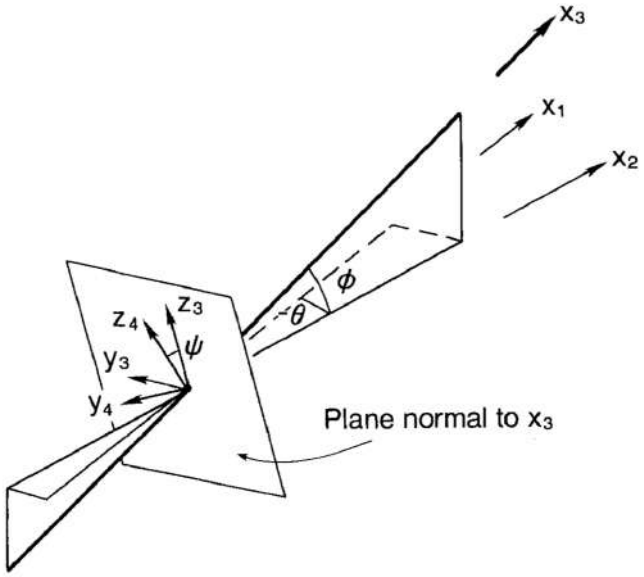

Figure 2.6: *Three dimensional coordinate rotations for alignment of coordinate axes to the flow field over sloping terrain (Kaimal and Finnigan, 1994).*

2.3.3 Turbulent Components

The turbulence analysis of the variables measured on the surface towers (velocity component and sonic temperature) starts from the Reynolds decomposition, according to which it is possible to write:

$$u_i' = u_i - \overline{u_i} \tag{2.9}$$

where u is the measured variable, $\bar{u}$ is the mean values and u_i' is the fluctuation. The application of Reynolds decomposition requires some averaging rules:

$$\begin{aligned} \overline{u_i'} &= 0 \\ \overline{u_i u_j} &= \overline{u_i} + \overline{u_j} + \overline{u_i' u_j'} \\ \overline{\overline{u_i}\, u_j} &= \overline{u_i}\, \overline{u_j} \\ \overline{a u_i} &= a\, \overline{u_i} \\ \overline{u_i + u_j} &= \overline{u_i} + \overline{u_j} \end{aligned} \tag{2.10}$$

These relations are valid only if the time series is statically stationary over relevant time scales, so that time averages are equivalent to ensemble averages, for which Reynolds averaging holds (ergodic hypothesis) (Kaimal and Finnigan, 1994). In the ABL, the characteristics time scale of about 1 hour sets the validity time limit. Turbulent components of velocity are computed with the eddy covariance method, using averaging periods of 5 minutes. Specifically, we computed turbulent variables with the eddy covariance method (Aubinet et al., 2012) using averaging period of 5 minutes. This variable are the kinematic flux of heat ($\overline{w'T'}$). Finally, we computed the TKE, starting from turbulent component of velocity:

$$TKE = \frac{1}{2}\left(\overline{u'^2} + \overline{v'^2} + \overline{w'^2}\right) \tag{2.11}$$

2.3.4 Vertical Profile of potential temperature θ

Finally, the analysis considers time series (30 minutes averaged) and vertical profile (10 minutes-averaged) of potential temperature (θ) computed for each levels at both tower's locations. Firstly, we need to find a pressure reference. Pressure data are not available at WS1 so we need to consider the pressure values at the PWIDS59, which is located to the east of the WS1 (Figure 2.4). Using the pressure measured at 2m AGL at PWIDS59, the pressure values at WS1 for each levels can be obtained, using the hypsometric formula. The same formula was used to derive the pressure levels of WS2, but using the ground pressure measured at WS2 as a reference .

$$P_{level} = P_0 \cdot exp\left(\frac{z_0 - z_{level}}{(g/\Re_d) \cdot T}\right) \tag{2.12}$$

where T is the average thermohygrometer temperature between heights z_0 an z_{level} and P_0 is the reference pressure. Here below are the formulae for the other variables:

$$\theta_{level} = T_{level} \cdot \left(\frac{P_0}{P_level}\right)^{(\Re_d/C_p)} \tag{2.13}$$

where θ refers to potential temperature at 0.5m AGL at each tower, $\Re_d/C_p = 0.28571$ is dimensionless, $\Re_d = 287.053\ \mathrm{J\,K^{-1}\,kg^{-1}}$ is the gas constant for dry air and C_p is the specific heath capacity.

Chapter 3

Case-studies Overview

This thesis focuses exclusively on the datasets and instrumentation which belong to the so-called west slope of Granite Mountain. Four IOPs has been chosen, two from the fall campaign, IOP2 and IOP6, and two more from the spring campaign, IOP4 and IOP7. In the following sections all times are given in Granite Mountain local time: Mountain Daylight Time, namely MDT (UTC - 6).

The western side of the Granite Mountain turns out to be the least equipped with weather instruments and, perhaps for this reason, less studied. The primary assessment that has been carried out in the choice of the IOPs has been the actual availability of the data, that is the quality and the completeness of the different datasets of all the analyzed physical quantities for both flux towers. Therefore, the choice of the days analyzed was subordinated to the aforementioned availability. Nevertheless, there are some shortcomings in the datasets. The WS1 tower has no thermohygrometers data on the IOP2 (fall campaign of 2012) and this has made it impossible to evaluate the various stability indices along the tower levels. The WS1 morning transition data of both IOP4 and IOP7 (spring campaign of 2013) are also missing.

A general description of the diurnal cycle of the IOPs is given in this chapter, accompanied by a rough identification of the two transitions using only time series of wind speed and direction, temperature and relative humidity. A detailed definition of morning and evening transitions will be found in the subsequent chapter.

IOP	Date and time UTC	Date and time MDT	WS1 (UTC)	WS2 (UTC)
Fall 2012 IOPs				
2	20 UTC, 1 Oct 20 UTC, 2 Oct	14 MDT, 1 Oct 14 MDT, 2 Oct	NO DATA from 20 UTC,1 Oct to 23:36:03.8, 1 Oct Sonic at 0.5 m is not working	Problems with the sampling rates from 20 UTC to 21 UTC, 1 Oct
6	08 UTC, 14 Oct 08 UTC, 15 Oct	02 MDT, 14 Oct 02 MDT, 15 Oct	FULL DATASET	FULL DATASET
Spring 2013 IOPs				
4	20 UTC, 11 May 20 UTC, 12 May	14 MDT, 11 May 14 MDT, 12 May	NO DATA from 12:05:58.75 12 May to 16:22:23.3 12 May	FULL DATASET
7	2330 UTC, 20 May 20 UTC 21, May	1730 MDT, 20 May 14 MDT, 21 May	NO DATA from 10:10:20.65, 21 May to 16:05:58.3, 21 May	FULL DATASET

Figure 3.1: *Dates and times of the four IOPs chosen, each one with its dataset shortcoming, if present.*

3.1 Climatology and Synoptic Conditions

The U.S. Army's Dugway Proving Ground (DPG) site is characterized by an arid climate with an annual cumulative precipitation of ≈ 100 mm. The annual mean air temperature is ≈ 13.7 °C (Hang et al., 2015). Given the arid conditions, the vegetation is sparse desert steppe on the order of 1 m tall (Jensen et al., 2017).

Some rain events occurred during the field campaign. In particular, as reported by (Jensen et al., 2017), precipitations occurred on October 12th (≈ 10 mm) 2012 and from May 17th to 20th (with cumulative rainfall of about 15 millimeters, depending on the exact location). These events enhance the relative humidity of both IOP6 and IOP7 , as will be evident in sections 3.2.1.2 and 3.2.1.4

The fair weather conditions required for the occurrence of the thermal circulation are dominated by high pressure and absence of fronts passage or large pressure gradient. The synoptic conditions on the west part of the United States were analyzed with the aid of ERA5 reanalysis (Hersbach et al., 2018). Reanalysis combines model data with observations from across the world into a globally complete and consistent dataset using the laws of physics. The atmospheric variables that were chosen to built up the reanalysis

were the geopotential height at 500 hPa and the mean sea level pressure.

3.1.1 Fall IOPs

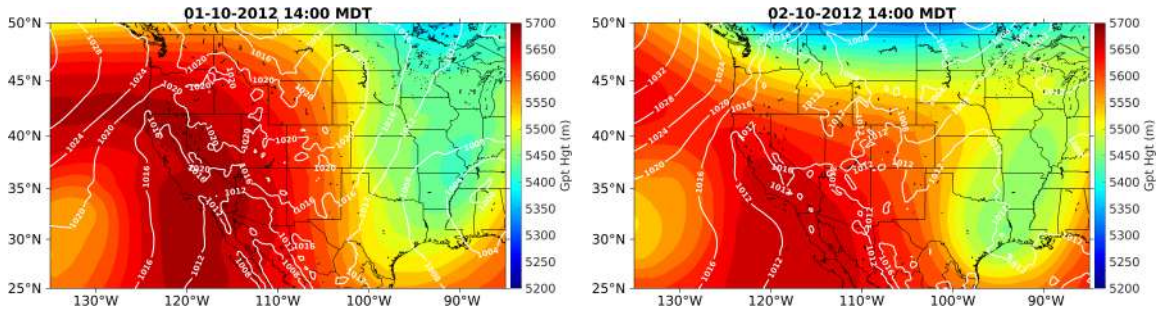

(a) (b)

Figure 3.2: *IOP2 large scale atmospheric condition (Generated using Copernicus Atmosphere Monitoring Service information (2021))*

Figure 3.2 shows the synoptic condition at the beginning and at the end of the IOP2. In figure 3.2(a) the high pressure (1016-1020 hPa) and the elevated geopotential height indicate stable weather conditions all over the west side of the United States, where the measurement site was located. The geopotential height evolution on this side may suggest the presence of some weak disturbances in the upper layers just before the end of the IOP2, but nonetheless mean sea level pressure still remains quite high in Utah (1012 hPa).

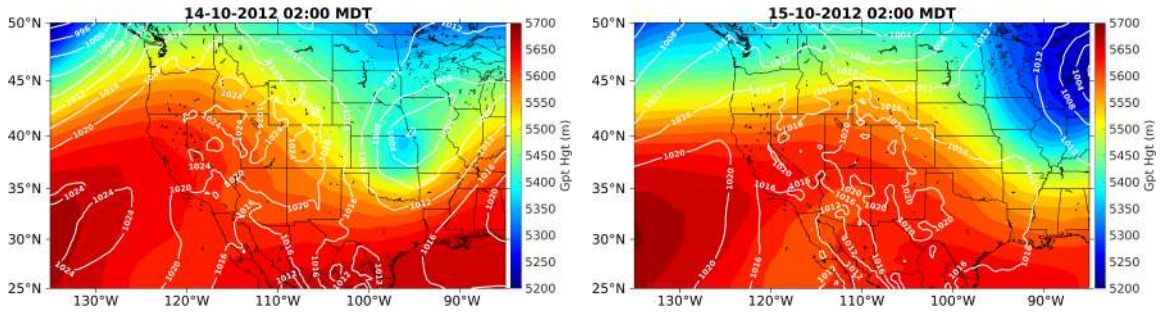

(a) (b)

Figure 3.3: *IOP6 large scale atmospheric condition (Generated using Copernicus Atmosphere Monitoring Service information (2021))*

In figure 3.3 there is a large high pressure system on the western United States, with values up to 1024 hPa in Utah, which however tends to weaken slightly during the course

of the IOP6. The disturbances in the upper layer are made visible by the geopotential height reduction, but they affect mainly the central-east side of the USA.

3.1.2 Spring IOPs

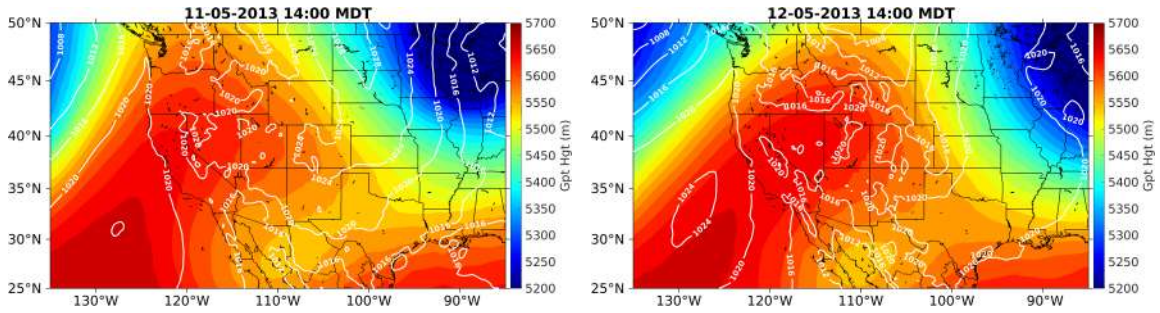

(a) (b)

Figure 3.4: *IOP4 large scale atmospheric condition (Generated using Copernicus Atmosphere Monitoring Service information (2021))*

May is usually the most synoptically active month of the year (Hang et al., 2015). High pressure, up to 1020 hPa, is clearly visible in both panels of the figure 3.4. Therefore it is evident that IOP4 had weak synoptic forcing.

The IOP7 certainly had the most unstable synoptic conditions among the IOPs, but the atmospheric conditions in the lower layers still allowed it to be classified as quiescent. Starting from the figure 3.5(a), it is clearly visible the mean sea level pressure drop from an initial value of 1016 hPa to 1008 hPa. This IOP also shows the lowest value of geopotential height at 500 hPa throughout experimental area.

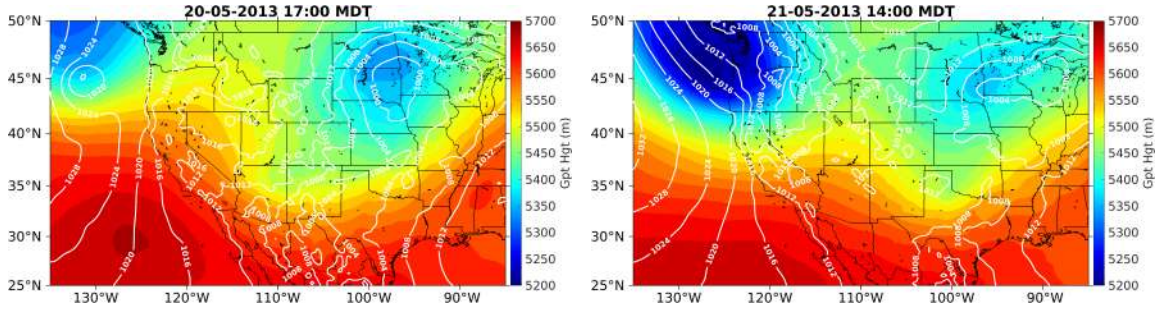

(a) (b)

Figure 3.5: *IOP7 large scale atmospheric condition (Generated using Copernicus Atmosphere Monitoring Service information (2021))*

To summarize, the previous figures shows that weak synoptic forcing in the western United States occurs oftentimes when a trough shifts from north, affecting the eastern side, while a ridge rise on the western part.

3.2 Mean Diurnal Cycle Flow of Fall and Spring IOPs

In all four IOPs analyzed, the synoptic forcing was quite weak to let the thermal circulation develops undisturbed or near enough. Despite each IOP presented interesting peculiarities that distinguished them from others, certain common characteristics existed. In the following section a more detailed description of the IOPs is presented through the diurnal cycle of the main meteorological variables analyzed. The IOPs are described in chronological order.

3.2.1 Winds and Temperatures

The topography of the west slope site measurement can lead to intricate interactions between slope winds and valley winds. Such interactions can be seen in the wind speed and direction time series, in addition to the time series of temperature and relative humidity. The average period chosen for the time series intervals was 30 minutes, with the indicated times referring to the beginning of the averaging period. Note that in every figures all times are given in Granite Mountain local time: Mountain Daylight Time, namely MDT (UTC - 6).

3.2.1.1 IOP2

The IOP2 started on October 1st at 14 MDT but the initial part of the dataset presented some problems. In figure 3.6 data begin one hour after the start fixed according to the MATERHORN field program. All wind speed levels, at first, showed the same pattern. The lowest speed is found at the lowest level and, from that, the speed increased along the tower levels, in ascending order of height. What appears to be up-valley north-westerly wind lasted just before sunset. Then a suddenly wind speed decrease

happened and it was accompanied by a rotation of the wind from the northwest to easterly/northeasterly downslope direction, starting from the lower levels of the tower. After sunset, wind speed and direction presented some variability. During the night the highest wind speed frequently occurred at 5 m above ground level (AGL). It was observed that the wind speed pattern of the 20 m AGL did not follow the other precisely, and this was true also for the wind direction. The lowest level at WS2, being the closest to the ground, had almost always the lowest speed, during both day and night. Wind speed did not increase along the tower as it happened before sunset instead. Wind direction swung between the northeast and the southeast and starting from 3 MDT the direction at 20 m exhibited some large oscillations until after sunrise, when there was a transition from the east-northeast to the south at about 09:00 MDT. Wind speed levels all seemed to follow the same pattern again, as it had happened in the initial part of the IOP2. An additional speed drop was found between 12:30 and 13 MDT and in the meanwhile wind direction appeared to turn south-westerly (upslope).

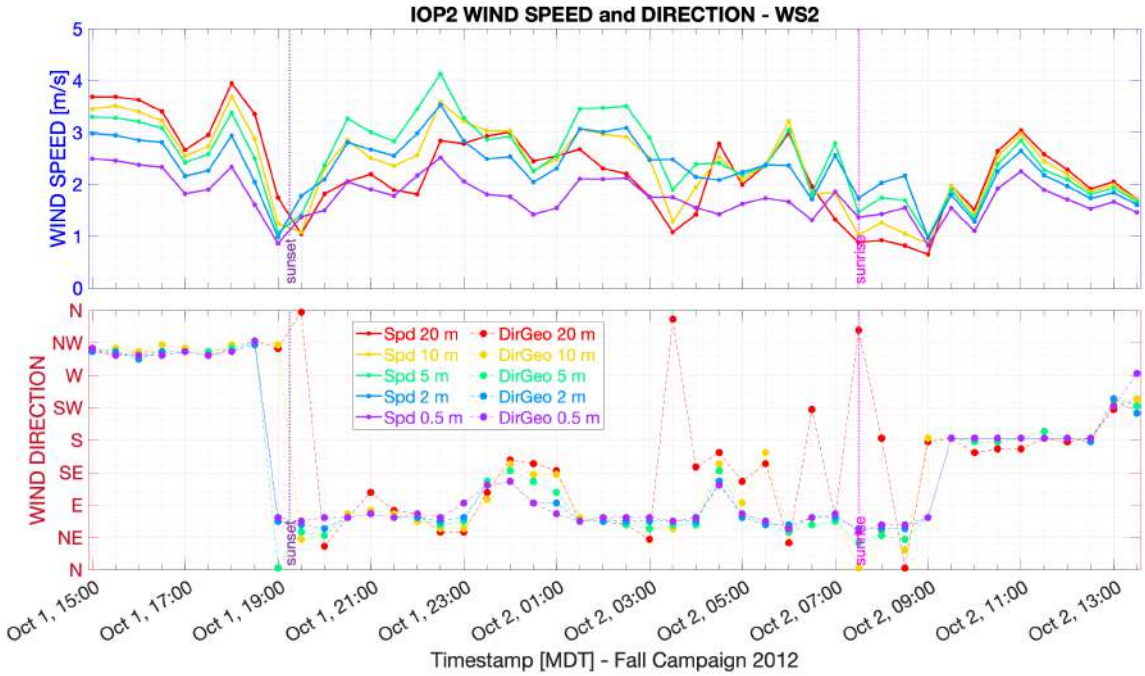

Figure 3.6: *IOP2 time series of wind speed and direction at WS2*

Time series of wind speed and direction at WS1 started a little later with respect to

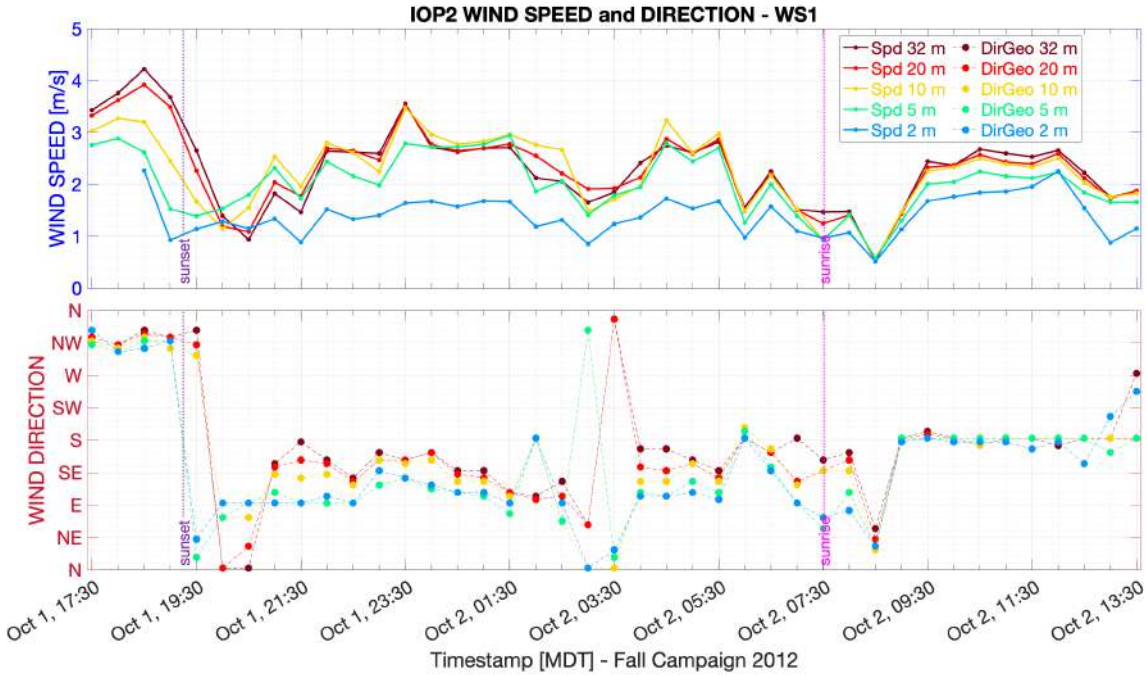

Figure 3.7: *IOP2 time series of wind speed and direction at WS1*

WS2 time series (Figure 3.7). Several differences were found: while wind speed at WS2 presented some variability throughout the night, all WS1 levels had almost the same wind speed (except for the 2 m level that presented a lower speed). In addition to this, the reversal of the higher wind speed levels between night and day was not observed at WS1. Wind direction variations seemed quite in agreement between the two towers, with some differences here too, especially in the timing of wind rotation between night and day. At WS1 wind blew from the northwest and the speed drop occurred at the sunset or slightly after that, starting from the lower levels. This short delay as regards the WS2 wind drop was probably due to the fact that the WS2 is closer to the steep slope ad it experienced colder air earlier than the WS1. After that winds at WS1 blew from the north-northeast, whereupon from the east-southeast in the lower layers and from the south-southeast in the upper levels, with some oscillation. A disturbance is visible in the figure 3.7, in both wind speed and direction near 3:30 MDT. Wind direction became then less defined. The speed drop and the variation of direction of the wind at WS1 happened half an hour after sunrise (08:00 MDT), slightly earlier than WS2 that had probably the

shadow cast by surrounding terrain. Thereafter, wind speed remained quite weak and all the tower levels experienced wind from the south. A further change in wind direction from the south-southeast to the south-southwest together with a speed drop occurred near 12:30 MDT, like the other tower.

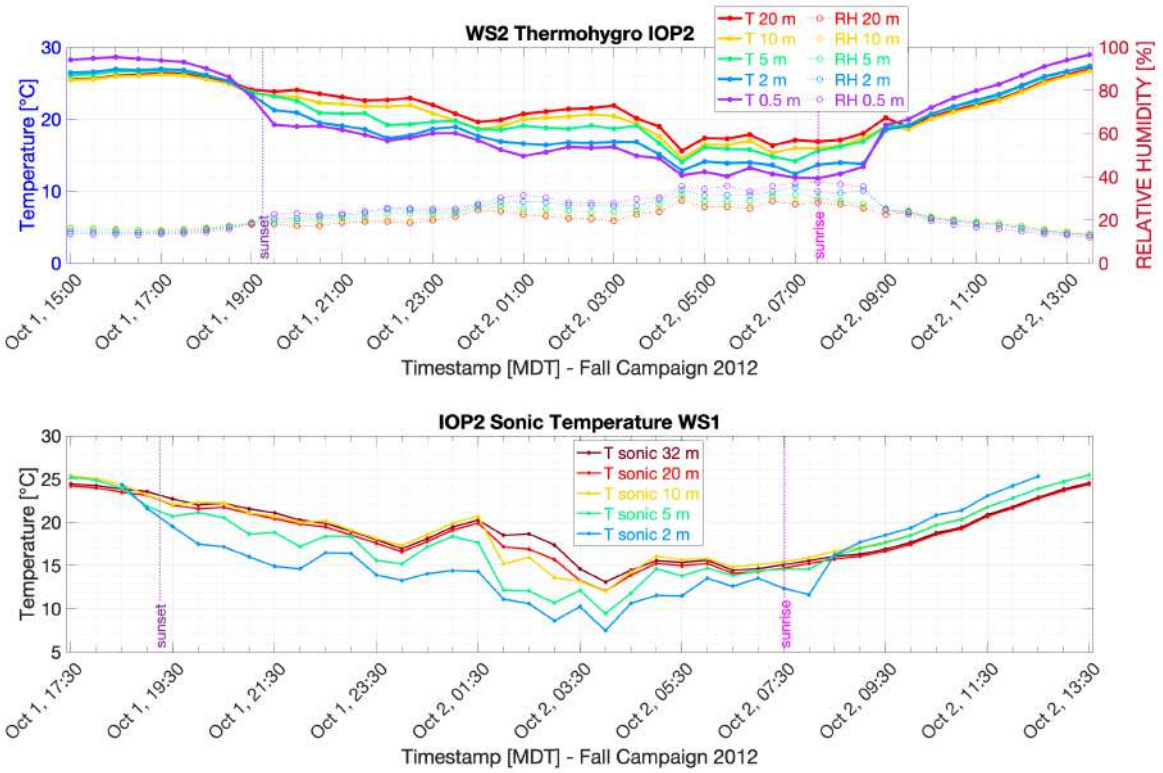

Figure 3.8: *IOP2 Temperature time series*

Figure 3.8 shows temperature time series, with sonic temperatures along the WS1 because of the absence of thermohygrometers data. Nighttime temperature inversion is well visible and its formation and destruction is in accordance with the wind variations in the previous figures. The disturbance seen in the time series of wind at WS1 was likely to be evident also in the temperature drop about 3:30 MDT.

3.2.1.2 IOP6

The IOP6 was centered on the daylight hours, with full-length time series of all the variables. Indeed, the range of data preceding and comes after sunset and sunrise was

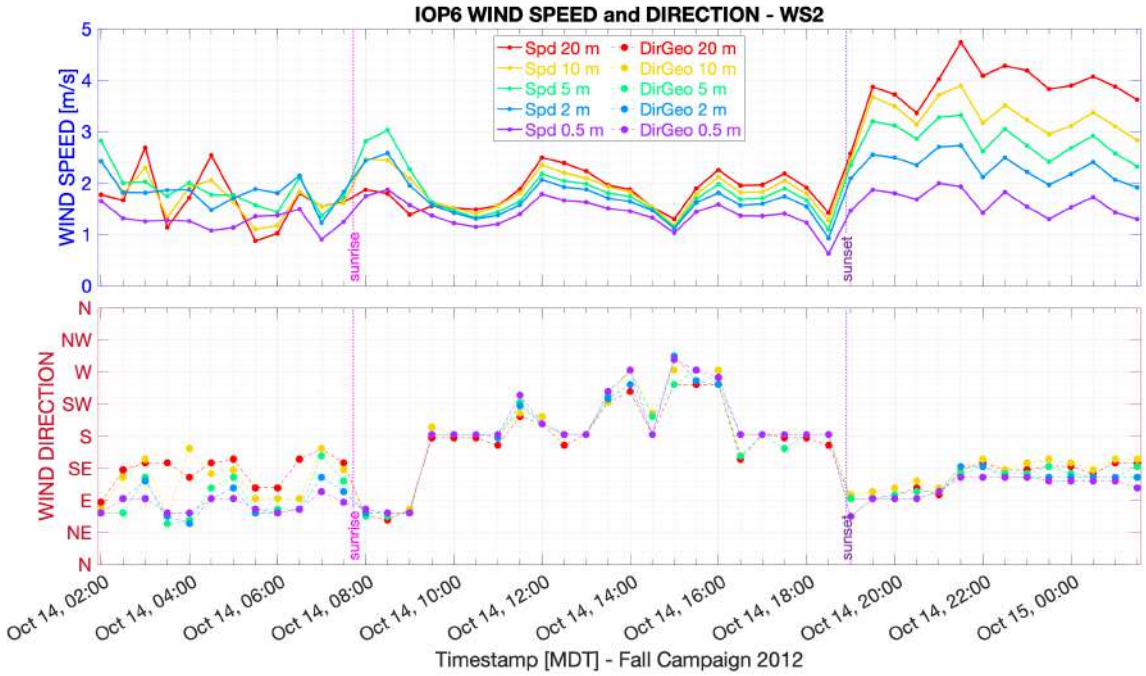

Figure 3.9: *IOP6 time series of wind speed and direction at WS2*

longer than the IOP2. Starting from wind direction at WS2 (Figure 3.9) there were some oscillations in the katabatic flow before the sunrise. Lower layers did not follow upper layer exactly, and this is visible in both wind speed and direction chart. Lower layers, in fact, were around the eastern direction with a near-constant wind speed while upper layer moved around the southeast and showed higher speed values. The 20 m level was the one with the widest oscillation in the wind speed. The wind direction turned toward the south, right after the speed drop occurred at 9:00. Then, wind speed showed two main oscillations whit a speed minimum about 15:00 MDT. All the different levels of the tower were distinct but appeared similar in speed, with the highest level (20 m) exhibiting the higher speed and the lower levels at reduced speed. Wind direction showed a certain volatility: starting from the south, after the morning transition it first swung to the southwest and then turned twice west. At the wind speed minimum there was the second rotation from the south to the west, followed by a final southward rotation. Sunset and the variation in wind speed and direction occurred almost contemporaneously. After that, wind speed showed a wider range of values, with the highest level reaching nearly 5 m/s. Wind direction was first easterly and thane became south-easterly, though

the lower levels were slightly easterly.

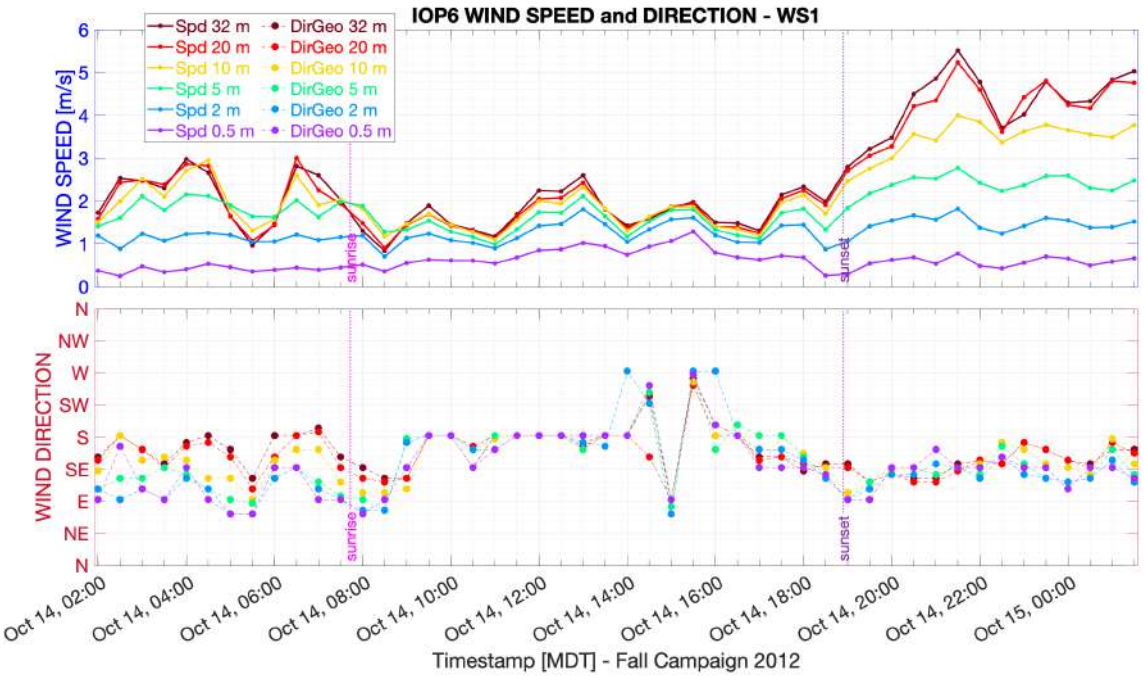

Figure 3.10: *IOP6 time series of wind speed and direction at WS1*

In figure 3.10 wind variations due to the change in the incident solar radiation between night and day are less visible. the levels closest to the surface were quite distinct from upper layers, both in speed and direction. Before the sunrise, speed in the lower levels remained substantially stable, with an easterly direction and some south-easterly oscillations. Higher levels had all the same speed and a south-easterly direction with some shift from the south. A speed minimum at 5:30 MDT occurred in the higher levels, together with a small temperature rise and a slight decrease in RH (Figure 3.11, lower chart). At about 8:30 a speed drop in the higher level and a variations in wind direction is visible. It took almost an hour for wind direction to turn southerly along the entire height of the tower. The higher levels exhibited the higher speed afterwards, like on the other tower. A suddenly change in wind direction at 15:00 MDT appeared at the same time as the speed minimum at WS2. The direction was than southeasterly until the end, except for a slight easterly rotation at sunset. The range of values of speed became considerably wide from 17:00 MDT onwards, with a minimal drop before sunset, and this

made the transition difficult to identify.

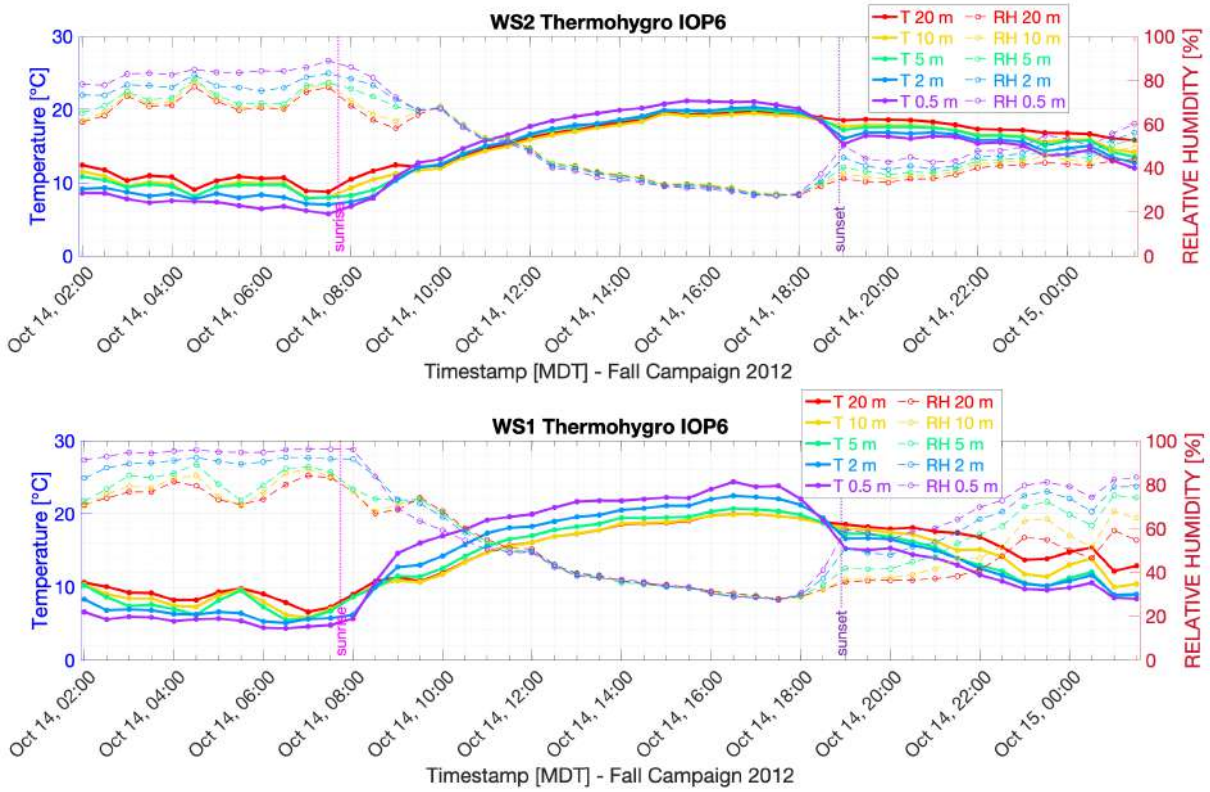

Figure 3.11: *IOP6 Temperature time series*

Figure 3.11 shows the time series of temperature and relative humidity from thermohygrometers data. As mentioned in section 3.1 during IOP6 relative humidity was quite high, due to the precipitation event on October 12th. The 32 m AGL thermohygrometer on WS1 was not working, therefore the two charts shows the same levels and can be directly compared. Relative humidity was higher and temperature was cooler on WS1 at night, because of its positions further down the slope. Because of its position WS1 also presented the widest range of temperatures, the strongest temperature inversion and the higher daily temperature. Also the strongest temperature gradient during daytime was at WS1. Looking at the temperature inversion at sunrise, its destruction occurred earlier at WS1 than at WS2 because of the upslope propagation of the sunlight front, while temperature inversion initiation at sunset did not seemed to happen without considerable time lag between the towers. The evening temperature drop was visible only in the lower

layers and it occurred almost at the same time as sunset. Upper layers experienced a moderate but continuous temperature decrease during that period. At WS2 the initial temperature drop at sunset was followed by a temporary increase, also minimally in the 20 m AGL level , and this behavior was not seen either at WS1 or in IOP2.

3.2.1.3 IOP4

Datasets relative to IOP4 covered a period of 24 hours, except for missing data at WS1 from 5:30 to 10:30 . Wind speed structure at WS2 presented in the first chart of figure 3.12 is very similar to wind speed at WS2 on IOP2 (figure 3.6) and to wind speed at WS2 on IOP6 with regard to a period of 6 hours before and after the sunrise (see the left part of the wind speed chart in figure 3.9). Thus, in summary, before sunset and after sunrise all levels followed the same pattern between them. In addition, the lowest level showed the lowest speed and the speed increased along the tower levels, in ascending order of height, as it was in IOP2 and IOP6. During the night the highest wind speed frequently occurred at 5 m above ground level (AGL) as in the IOP2.

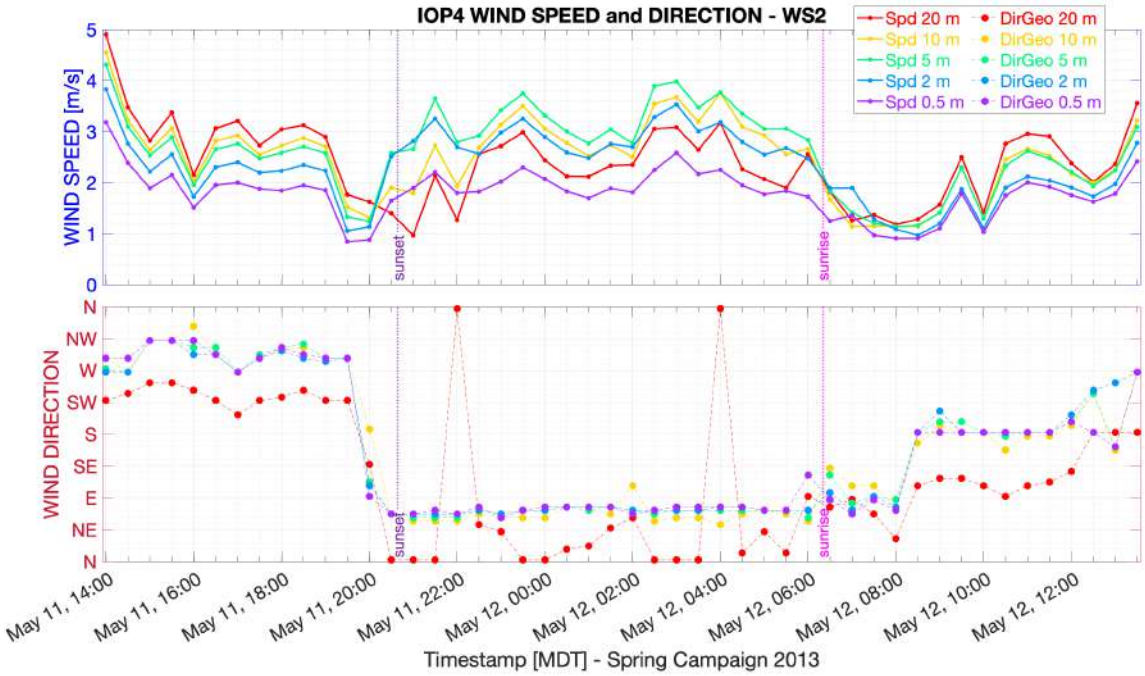

Figure 3.12: *IOP4 time series of wind speed and direction at WS2*

The 20 m AGL wind direction did not follow the other levels on WS2, neither by day nor by night. Starting at 14:00 MDT, wind direction at this level was initially southwesterly, and then, after the evening transition, it began to swing between the north and the north-east. It turned from the east just before sunrise and after that became easterly and southeasterly. Finally it was from the south. This development was not seen in any of the previous IOPs.

The other levels showed westerly and north-westerly wind at the beginning. They experienced wind from east/north-east during the night and easterly/southeasterly at sunrise. Than they showed wind from the south and finally from the south-west and west. This development at WS2 was quite in agreement with that seen on IOP2 and IOP6, regarding the latter only for a period of 6 hours before and after the sunrise.

It was observed that wind at WS2 presented near sunset a sharper decrease in the speed and a faster variation in the wind direction than after sunrise. This also applied to previous IOPs.

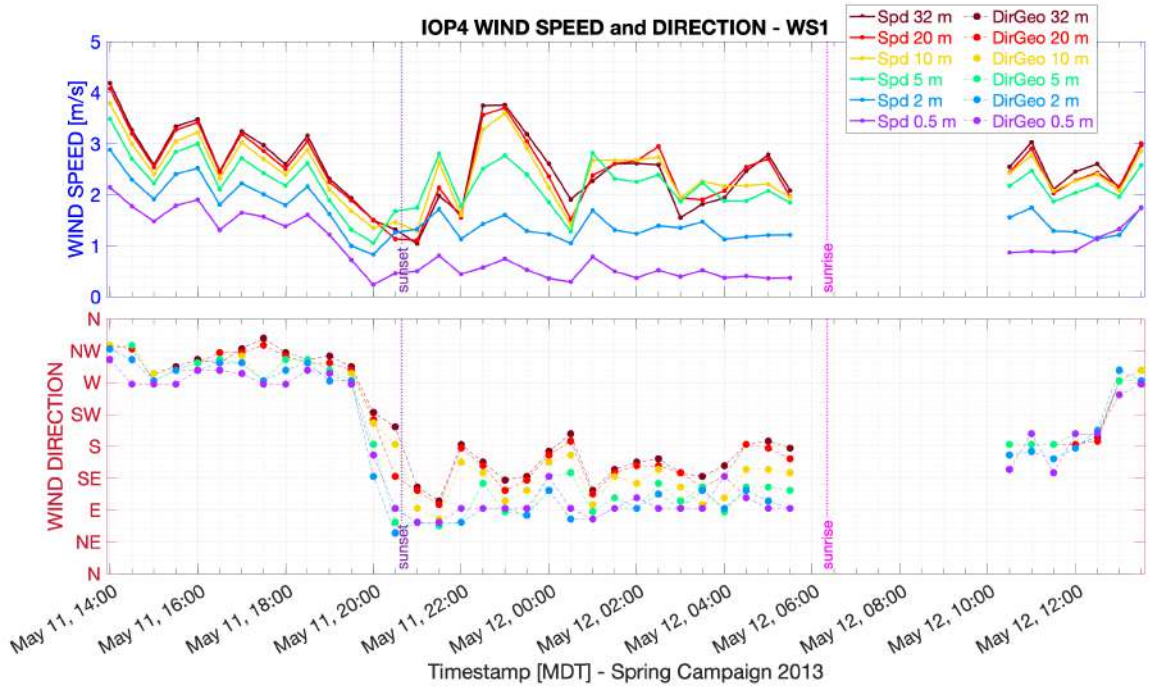

Figure 3.13: *IOP4 time series of wind speed and direction at WS1*

Wind speed and direction at WS1 were in accordance with the previous IOPs. In

figure 3.13 all tower levels present the same well defined pattern before sunset, each one with a different wind speed that increase along the levels, in ascending order of height. After that wind speed in the lower levels remained substantially stable whereas wind speed further up was more variable ad did not increased along tower levels. Wind direction presented a slight separation between lower layers (0.5 m, 2 m and 5 m AGL) and the others (10 m, 20 m and 32 m AGL). The former had an initial westerly wind while the latter were more northwesterly. Lower layer became averagely easterly at sunset whereas those above were more southeasterly and southerly sometimes. At the end of the IOP wind appeared to blow from the south with a finally westerly change.

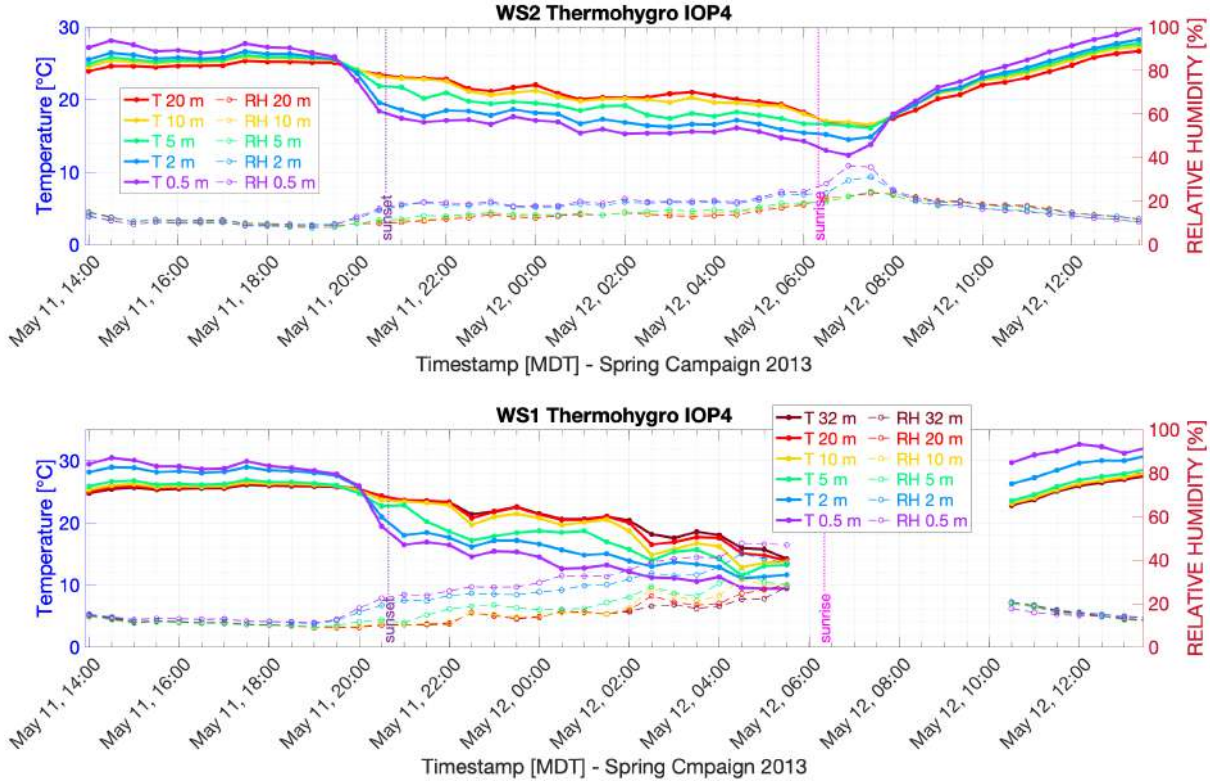

Figure 3.14: *IOP4 Temperature time series*

Figure 3.14 shows temperature time series at WS1 and WS2 on IOP4. Relative humidity was considerably low during the entire IOP and temperature varied according to the daily cycle. Even in this case WS1 presented the widest range of temperatures, the strongest temperature inversion and gradient and the higher daily temperature. Evening

transition seemed to occur at WS2 first. The temperature drop relative to the evening transition was visible only in the lower layer while upper layers temperatures remained steady or increased minimally until the inversion. The temperature drop occurred in advance of sunset, in contrast with what happened in the fall IOPs in which it occurred at the same time as sunset.

3.2.1.4 IOP7

The last IOP7 was the one with the highest wind speed values, specially after sunrise. At WS2 (figure 3.15) wind speed and direction structure was quite similar to the previous IOPs. The 20 m AGL wind direction did not follow the other levels on WS2, neither by day nor by night, as it did in IOP4.

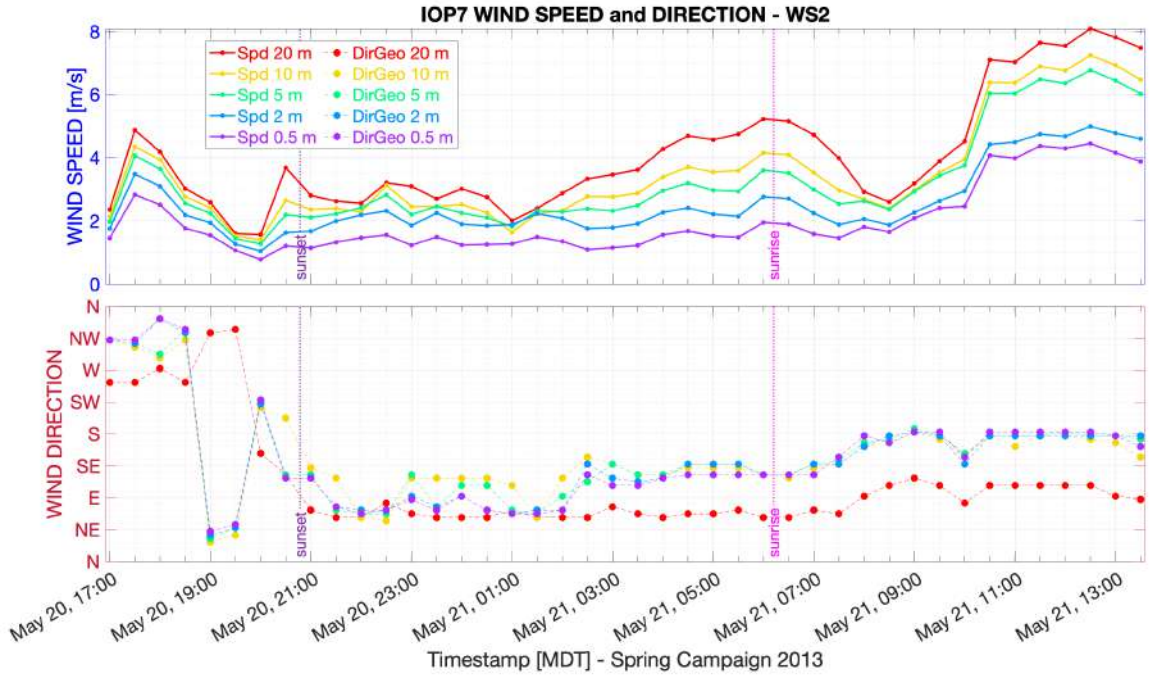

Figure 3.15: *IOP7 time series of wind speed and direction at WS2*

Even in this case the evening transition presented sharp variations in wind speed and direction. The morning transition, however, was less visible especially in the wind direction chart and perhaps it turned out to be disturbed by the stronger wind. After a rotation from the northwest in the lower layers and from west at 20 m AGL, the wind was

averagely easterly or northeasterly during the first part of the night, with the 10 m and 5 m AGL becoming sometimes southeasterly. Then, al levels presented a southeasterly wind while the 20 m AGL level remained between the northeast and the est. Wind speed showed a small drop in the upper levels near 01:00 AM, after which the speed at 20 m AGL raised substantially, reaching a speed of about 5 m/s at sunrise. The speed drop occurred between 08:00 and 09:00 MDT affected only the upper levels and did not result in a substantial change in wind direction. Indeed, wind changed direction becoming from the south in the lower layer and from the east at 20 m AGL.

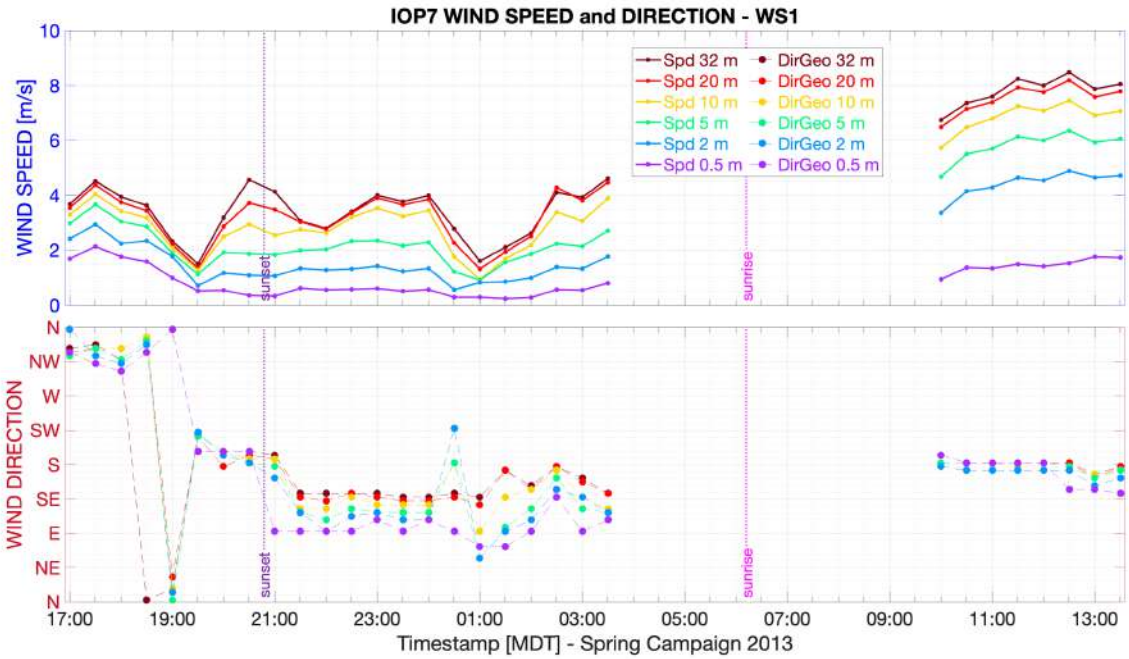

Figure 3.16: *IOP7 time series of wind speed and direction at WS1*

Wind speed and direction pattern of IOP7 at WS1 were very similar to those seen on IOP2 and IOP4. At WS1 the shortcomings in the dataset some hours before and after sunrise is visible in both speed and direction chart of figure 3.16. There were two main speed drop at WS1: the first one was before sunset and the second was the same seen at WS2, although it was much more pronounced at WS1 than at WS2. After that, the speed increased significantly, especially in the higher levels.

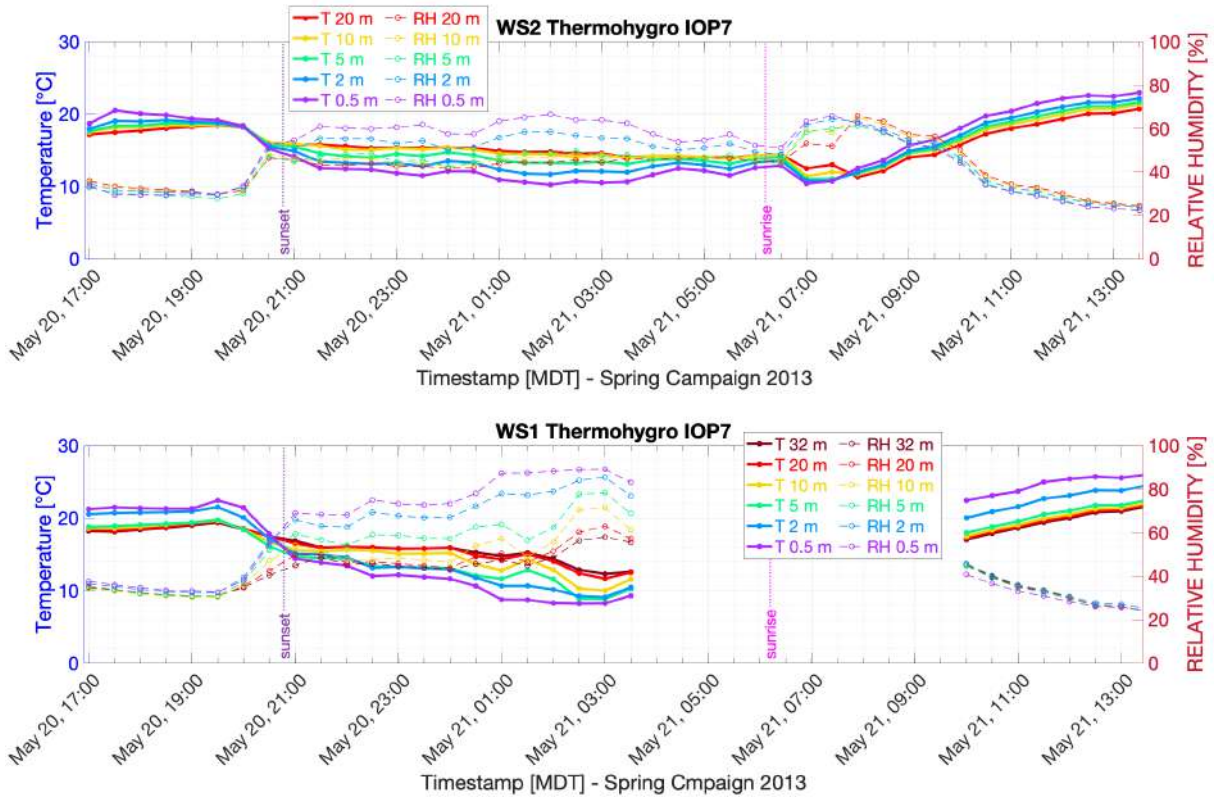

Figure 3.17: *IOP7 Temperature time series*

As mentioned in section 3.1 during IOP7 relative humidity was higher than IOP2 and IOP4, especially during the night. In figure 3.17 it is interesting to observe that during the night the temperature did not fall as it did in the other IOPs. Looking at the first chart of figure 3.17, nighttime temperature at WS2 remained almost constant and the temperature differences between the various levels of the tower were weak and tended to decrease approaching the sunrise. This was caused by the presence of the wind, which was stronger than in previous IOPs. The mixing caused by the wind brought warmer air from above to mix with colder air near the surface resulting in weaker temperature inversion. However, the temperature variations at sunrise and sunset were still visible. As can be seen in the first chart of figure3.17, the speed drop occurred between 08:00 and 09:00 MDT at WS2 mentioned above, was also characterized by the onset of the morning temperature increase.

3.2.2 Radiation

In figure 3.18 are shown the radiation time series of each IOP. It is possible to see in each chart the daily variation of incident (positive) solar radiation (SW), outgoing (negative) terrestrial radiation (LW) and the total net radiation (addition sum of solar and terrestrial radiation). This data are taken from the extensive surface energy budget instrumentation at the WS2. Radiation is computed at 5 minutes average to observe its variability due to the possible formation of clouds (i.e., small fluctuations during the day).

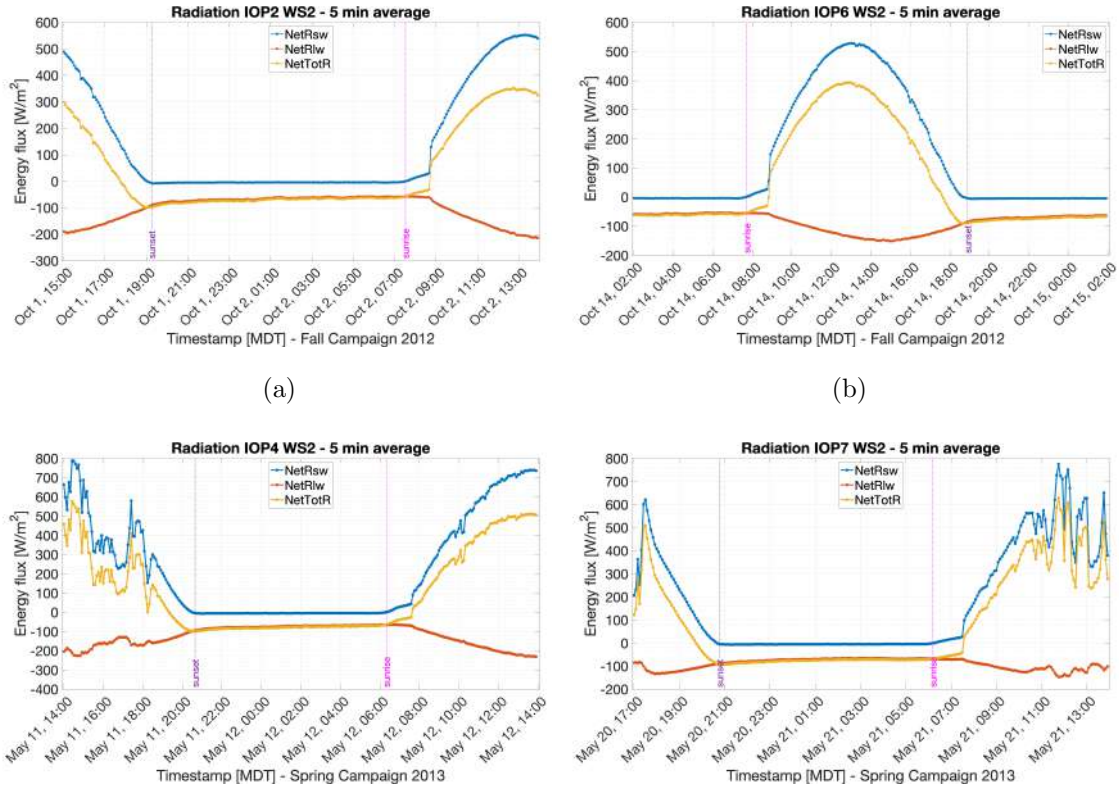

Figure 3.18: *Radiation time series*

Looking at the net shortwave radiation, there is a difference between sunrise and sunset period. Incident radiation increased sharply after sunrise due to the upslope propagation of the sunlight front while it gradually decreased near sunset, because of the predominance of scattered radiation. (3.18(a) and 3.18(b)) although shortwave radiation

is stronger and reaches higher values during spring (3.18(c) and 3.18(d)). The maximum values reached by incident solar radiation (SW) were obviously higher in the two spring IOPs than in fall IOPs, because of the seasonal variation of the sun position in the sky (sun declination angle). These factors can all influence the development of transitions.

Chapter 4

Results and discussion

In this section we analyse the morning and the evening transition on the west facing slope of the Granite Mountain during the four IOPs mentioned in the previous chapter. It is important to underline that the thermal circulation that develops in this area is far from the ideal conditions described in the theory. The particular circulation on this side of the mountain arises from the interaction between slopes and valley winds, resulting in a flow which comprises several characteristics of both regimes.

Sunrise and sunset times are crucial in the development of the transitions and are presented in table 4.1.

IOPs	**Sunset (MDT)**	**Sunrise (MDT)**
2	19:15 - 01 October 2012	07:31 - 02 October 2012
6[1]	*18:54 - 14 October 2012*	*07:43 - 14 October 2012*
4	20:39 - 11 May 2013	06:20 - 12 May 2013
7	20:47 - 20 May 2012	06:12 - 21 May 2013

Table 4.1: *Astronomical sunrise and sunset dates and times*

In this thesis the transitions have been investigated, based on available data, through the study of near-surface processes, as has been done in several other studies (e.g. Papadopoulos and Helmis (1999), Nadeau et al. (2013), Lehner et al. (2015), Jensen et al.

[1]IOP6 is a diurnal IOP (sunrise precedes sunset)

(2017), Nadeau et al. (2020)). The variable whose variation is analysed in this chapter are the following:

- wind speed and direction, temperature and relative humidity;
- 2 m AGL temperature and wind vectors of each west-slope instruments;
- vertical profile of potential temperature along the towers;
- TKE, its components and kinematic heat fluxes.

The morning transition will be analysed in section 4.2 focusing on the fall IOPs, followed by the evening transition analysis of a fall and spring IOP (Section 4.3).

4.1 Clarifications on the influence of topography on wind direction

The particular topographical configuration, shown in figure 4.1 makes necessary some clarifications regarding the wind direction. The WS2 is to the northeast of the WS1, in the steepest part of the instrumented slope and at the foot of the Granite Peak massif, which surrounds it from the north to the southeast. From this area to the west the contour lines take a northwest-southeast direction. The WS1 is located farther down the slope, on the southwest of the WS2 and towards the Playa, where the contour lines take a north-south direction. In general, the direction of the valley wind follows that of the contour lines, and the direction of the slope wind follow the direction of the contour lines maximum gradient (from east-northeast to west-southwest). Because of their geographical location on the slope, the WS2 should be more exposed to slope winds than the WS1, which should be more affected by valley winds instead. However, given the oscillatory behavior of the wind on time scales of less than an hour, both wind regimes are expected at both towers, with the resulting direction arising from the interaction between the different regimes.

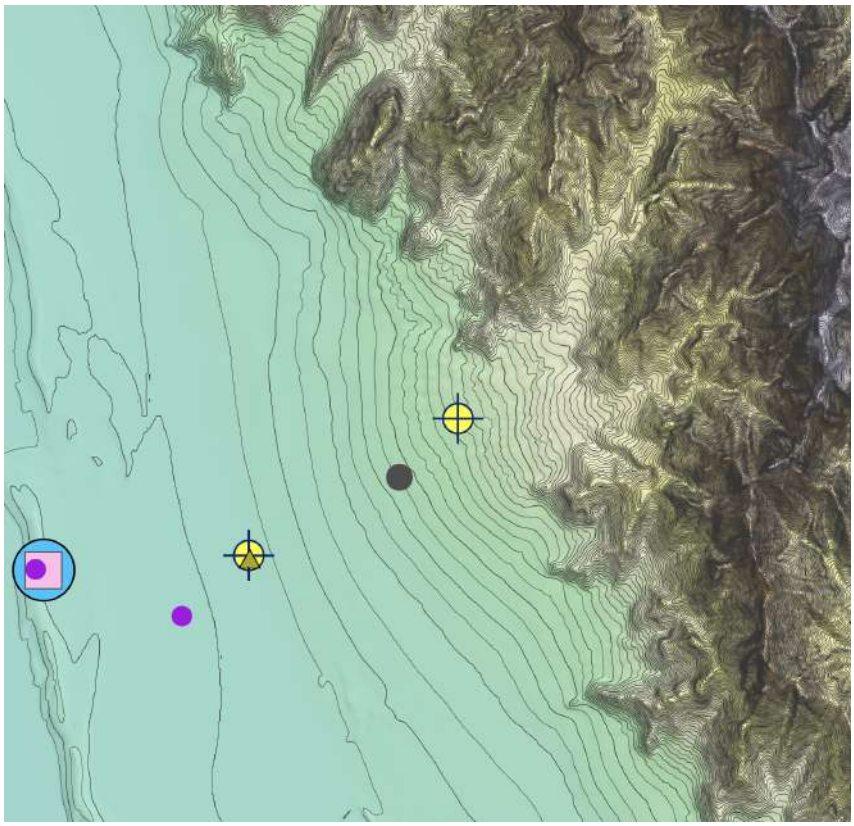

Figure 4.1: *West slope contour lines. Starting from the right and going to the west, we find WS2 (1374 m ASL), SAMS31 (1346 m ASL), WS1 (1313 m ASL) and PWIDS59 (1309 m ASL). In the western part there are the PWIDS62, the ceilometer and the soDAR (1312 m ASL)*

Despite the lack of instrumentation in the west slope with respect to the east one, it stand to reason that the west slope flow is influenced by the presence of the Playa to the west, of the Dugway Range and of a tow large valleys to the south of the Granite Mountain. Their positions are shown in figure 4.2. During the night, as the southerly flow comes out of the valleys and the downslope comes down the Dugway Range, it reaches the Big Gap and separates, proceeding partly towards the east slope. The southerly flow that does not interact with the topography of the Gap, proceeds northward reaching the west slope. Here the flow interacts with the topography and converges with the northeasterly downslope coming from the Granite mountain ridge, resulting in a southeasterly flow which sometimes rotates from the west-southwest, as the valley influence becomes prominent.

This is the expected behavior on the basis of the topographic configuration and of what is observed on the east slope of the Granite Peak (Lehner et al., 2015). The data to support this hypothesis, depending on their availability, will be shown in the following sections.

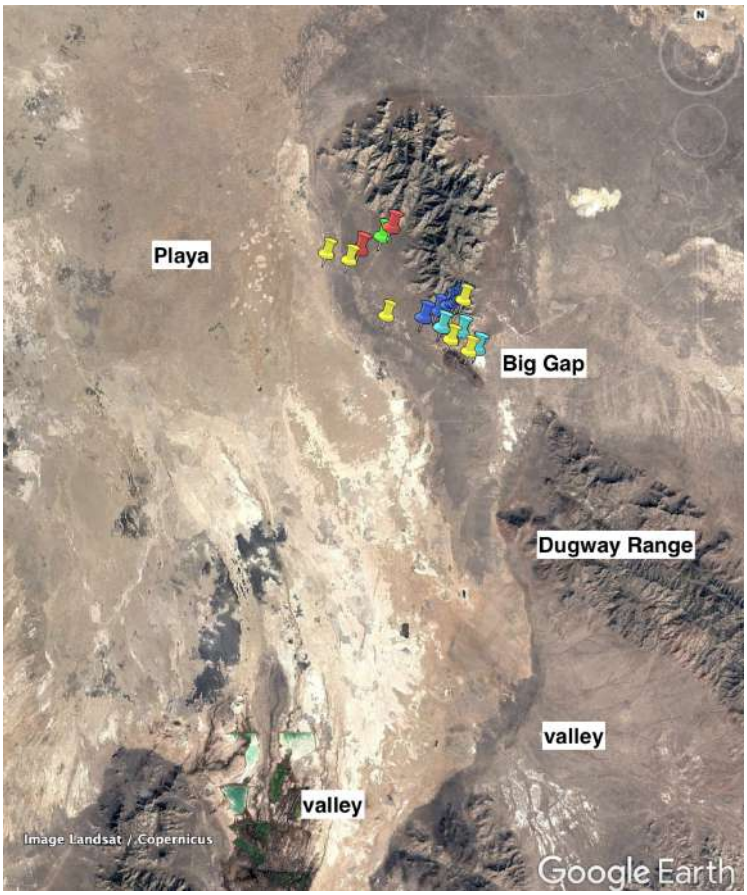

Figure 4.2: *Granite Peak surrounding topography. (Copyright Google Earth Pro.)*

4.2 Characterization of the morning transition

We will now focus on the morning transition in the near surface layer of IOP2 and IOP6 (2 October and 14 October of the 2012 fall campaign), the only ones for which both towers data are available (except for the lack of thermohygrometers data on IOP2 at WS1). Unfortunately, it is not possible to perform a complete description of the morning transition period during the 2013 spring campaign, owing the lack of any data at the

WS1 around the sunrise on IOP4 and IOP7. However, the length of the transition, based on the WS2 data, will be evaluated and compared with the results of the fall campaign at the end of this section.

The morning transition identifies the period between the end of the nocturnal flow and the onset of the diurnal one. There are several ways to characterize the morning transition and to evaluate its duration. This length can be assessed in four different ways:

- analysing the wind direction variation;
- assessing the duration of the erosion of the nocturnal thermal inversion;
- observing the change in sign of turbulent fluxes;
- considering the TKE variations.

During the morning transition, two main phenomena take place: the erosion of the temperature inversion and the rotation (i.e. transition) of the wind. The two phenomena occur in order, but may even occur simultaneously. They will be outlined in section 4.2.2.2 and 4.2.2.3 for both towers, also comparing the differences between them. The transition, being a gradual phenomenon, is also characterized by the so-called calm period, during which the wind speed drops to very low values. This period is analysed in section 4.2.2.5. Finally, in sections 4.2.2.6 and 4.2.2.7, the TKE and the kinematic heat flux variations will be assessed.

The identification of the local sunrise is of crucial importance, as we will see in the next section. Therefore the characterization of the morning transition period will start from the analysis of the solar radiation measured at WS2 and SAMS31. Then, all the other variables mentioned above will be introduced and discussed. At the end of the morning transition description, a short report will be performed to display summary information, in order to underline the major differences between the two towers and among all the IOPs analyzed (Section 4.2.3).

4.2.1 Evolution of the Solar Radiation at Sunrise

Once the sun rises, the west side of the mountain is not immediately illuminated by direct light but undergoes a period of twilight characterised by the presence of diffuse

solar radiation only. The presence of diffuse radiation before the arrival of the direct light is characteristic of the west slope morning transition, which distinguishes it from the morning transition on the east slope. In fact, because of the west-facing orientation of the terrain, after astronomical sunrise the slope gets illuminated at its top and then at its bottom, while the central sections of the steepest part remain in the shade even after several hours from astronomical sunrise. Direct solar radiation, contrary to the diffuse one, provides enough energy for the ground to be heated and to warm the near surface atmosphere, activating the destruction of the nocturnal regime. It then triggers the nocturnal inversion breakup, the sign reversal of the heat fluxes (and their intensification), and finally the transition of the wind direction, resulting in the establishment of the diurnal regime, as we will se in the following sections.

The only instruments that measures solar irradiance in this area are the WS2 and the SAMS31 that is located between the two towers (See figure 4.5). Considering the evolution of radiation at WS2 and SAMS31 on IOP6 as example, during the first hour after astronomical sunrise (07:43 MDT) these instruments only receives diffuse radiation. Solar radiation jumps rapidly to higher values at 08:35 MDT at SAMS31 and then (08:45 MDT) at WS2, highlighting the upslope propagation of the sunlight front, that is the local sunrise on each instrument. This can be seen by looking at the net shortwave radiation K (K_{SAMS31} is the shortwave radiation at SAMS31) in figure 4.3. K is the sum of upwelling K $\uparrow$ and downwelling K $\downarrow$ shortwave radiation (the same applies to net longwave radiation I = I $\uparrow$ + I $\downarrow$). The rate of growth in time of K shown in figure 4.4, together with the decrease (increase in absolute value) of net longwave radiation I, gives a further confirmation of the timing of the local sunrise at WS2. Being such an important feature of the transition (Nadeau et al., 2020), the local sunrise at the WS2 will be shown on every charts in the following sections. Figure 4.5 shows the west slope partially in the shade at 8:00 on 14 October 2012, slightly after the astronomical sunrise at 07:43. Looking at the distance between the instruments, it is reasonable to assume that the radiation reaches the WS1 quite earlier than the WS2. It is possible to estimate the relative position of the three instruments by projecting their longitudes on a horizontal axis (that is, an axis with constant latitude) so as to get an idea of the delay with which the two towers are illuminated by direct solar radiation. The distance to the east between

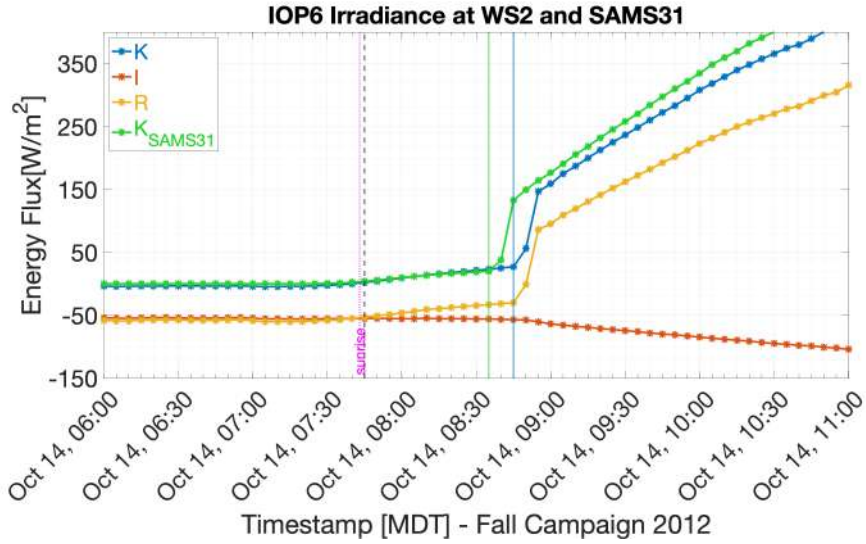

Figure 4.3: *Evolution of radiation during the morning transition on IOP6. K, I and R refers to the WS2 and are the net shortwave, the net longwave and the total net radiation ($R = K + I$) respectively (K_{SAMS31} refers to the SAMS31 shortwave radiation, the only radiation measurement at SAMS31).The black dashed line is at 07:45 when downwelling solar radiation K change sign, in accordance to the astronomical sunrise (07:43) identified by the pink vertical line. The green and the blue solid lines are the local sunrise at SAMS31 (08:35) and at WS2 (08:45)*

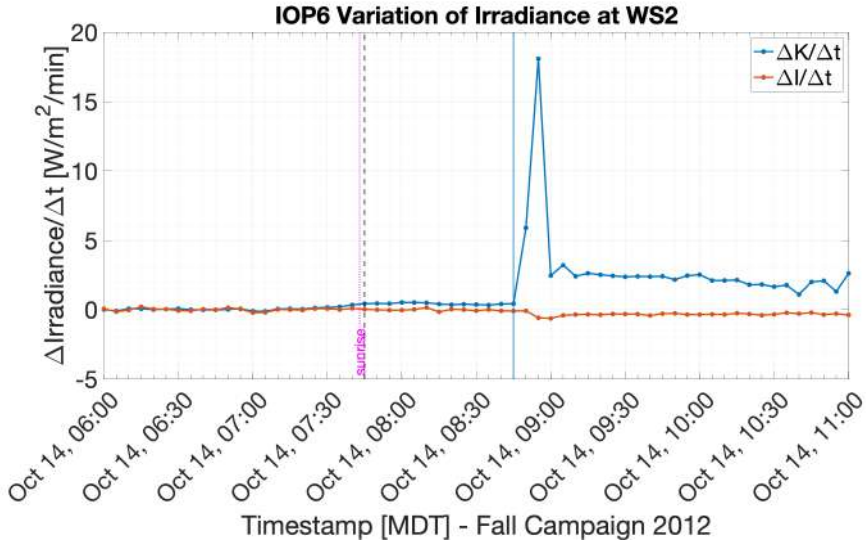

Figure 4.4: *Rate of variation in time of K and I during the morning transition on IOP6 at WS2*

the WS1 and the SAMS 31 is about 1082 m and there are about 416 m between the SAMS31 and the WS2. Since the direct radiation arrives on the WS2 about 10 minutes after reaching the SAMS3, it is reasonable that the radiation arrives on the WS1 at least 15 minutes before the SAMS 31. This hypothesis will be compared with the onset of the thermal inversion erosion at WS1 in section 4.2.2.2 and with the time of sign reversal of kinematic heat flux in section 4.2.2.7.

Figure 4.5: *Insolation on the WS1, WS2 and SAMS31 on 14 October 2012 at 08:00 MDT showing the presence of the shadow along the west slope after astronomical sunrise. Some sections on the steepest part of the slope get already illuminated. The horizontal axes used for the estimation of the relative position of the instrument is also reported. Other useful pictures showing topographic shading around this period are not available on Google Earth (Copyright Google Earth Pro.)*

4.2.2 Near-surface variables analysis

First of all, the transition is described by analysing the time series of temperature, humidity and wind. A 10-hours range of data, centered around the astronomical sunrise time, is chosen to analyse the variation in time of wind, temperature and humidity, in

order to have a comprehensive understanding of the transition development. This segment starts around 03:00 MDT, when the nocturnal boundary layer is well developed (i.e., the nocturnal flow and the thermal inversion are both present) and ends in the late morning, around 11:30 MDT, a few hours after the transition is over. Its description and analysis proceeds chronologically through three subintervals. The first one starts around 03:00 MDT and lasts until the onset of the nocturnal temperature inversion erosion. It is characterised by the absence of solar radiation, an almost undisturbed surface inversion and a downslope/down-valley flow. The second one spans from the initiation of inversion erosion (that is slightly before astronomical sunrise) to the local sunrise, identifying the period during which the diffuse solar radiation spreads on the experimental site. This affects the slope temperature but is not sufficient to erode the nocturnal temperature inversion[2]. The arrival of direct solar radiation identifies the beginning of the third subinterval, during which the nocturnal temperature inversion is completely eroded and the rotation of the wind take place. This period ends when the diurnal regime ia already established, coinciding with the conclusion of the analyzed 10-hours data segment.

4.2.2.1 Period 1 - Nocturnal boundary layer before the erosion

Time series of temperature, relative humidity and wind speed and direction at WS1 and WS2 on IOP2 and IOP6 around the morning transition time are shown in figure 4.6 and 4.7. Thermohygrometers data are not available at WS1 on IOP2, however the relatively low humidity on this IOP, due to the absence of precipitations in the preceding days (Jensen et al., 2017) makes the sonic temperature quite a good approximation of the absolute real temperature (Aubinet et al., 2012). The nocturnal boundary layer over the west slope is characterized by the presence of the thermal inversion and of a katabatic flow which is periodically replaced by the down-valley flow, interacting with the valley temperature inversion. Time series show an oscillatory behavior in all variables and the occurrence of some disturbances in the nocturnal flow, which affect the two towers differently. The easterly-northeasterly downslope is mainly visible in the lower layers at

[2]It should be mentioned that only during the spring campaign this period coincides with a further decrease in temperature at WS2. However, given the lack of data on the WS1, it is not possible to perform a complete description of the morning transition period, as mentioned earlier.

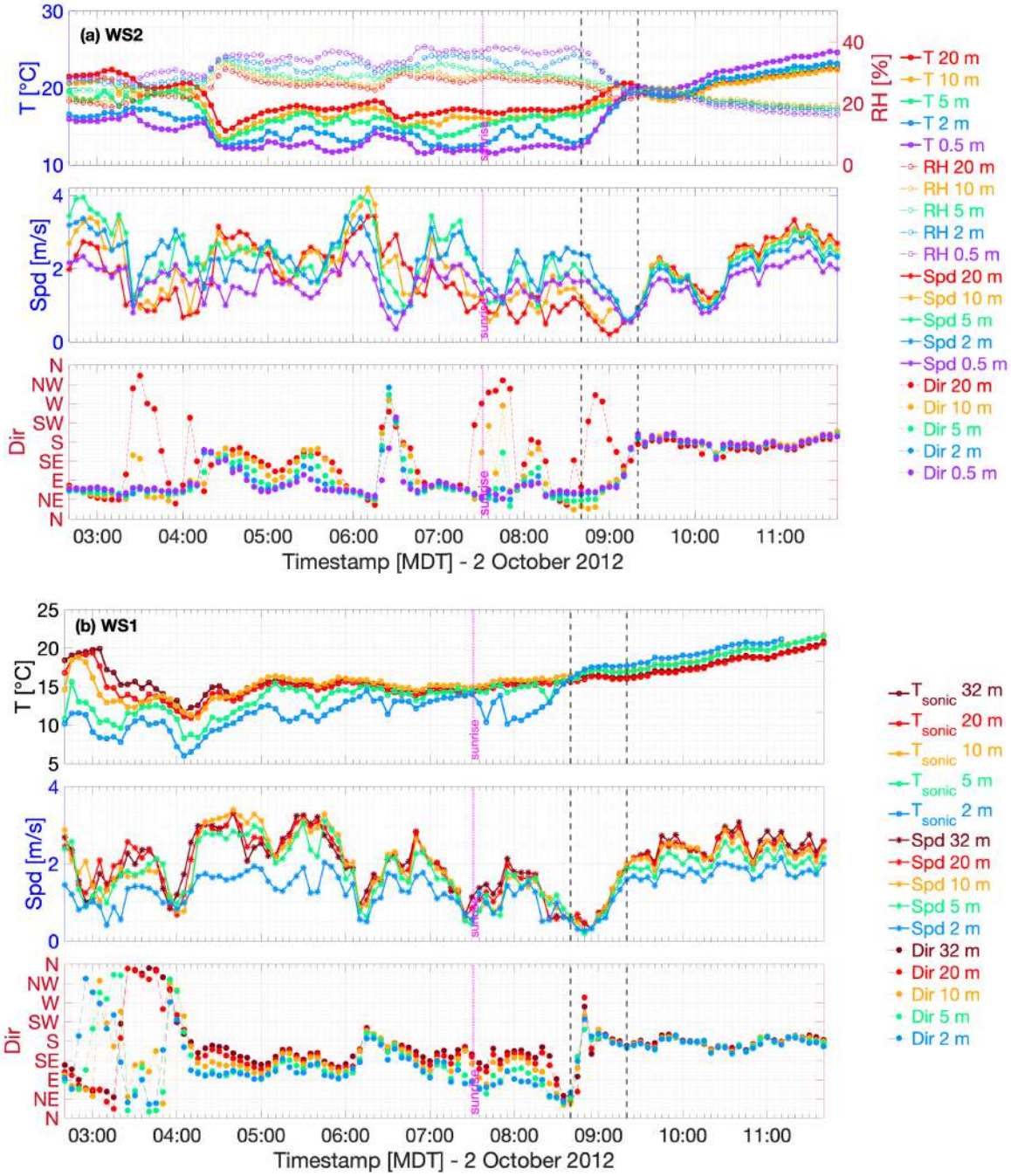

Figure 4.6: *Time series of T, RH, wind speed and direction at (a) WS2 and (b) WS1 on IOP2. The black dashed line identify the local sunrise (08:40) and the completed wind rotation at WS2 (09:20) respectively. The sonic temperature is the only temperature data available at WS1*

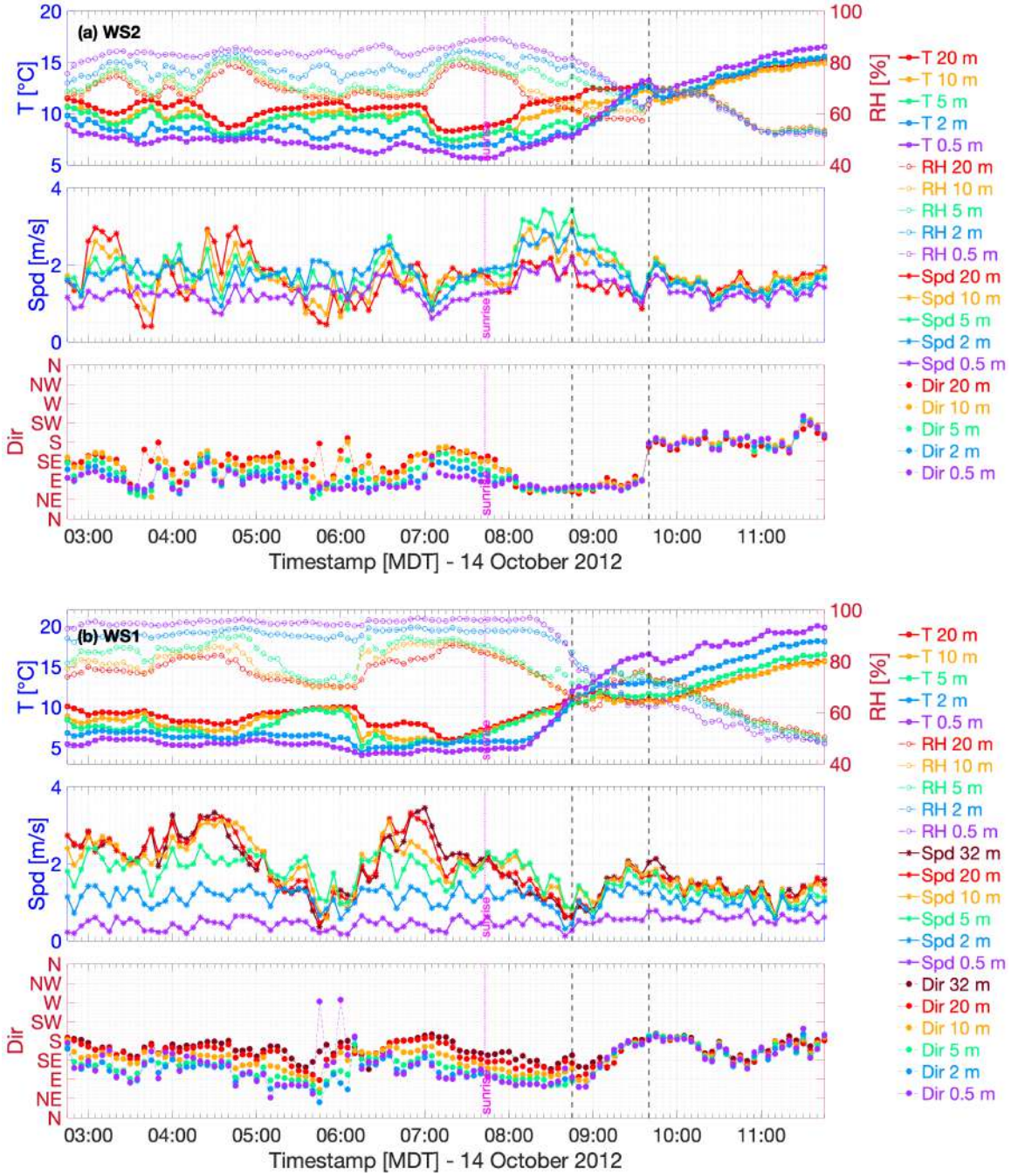

Figure 4.7: *Time series of T, RH, wind speed and direction at (a) WS2 and (b) WS1 on IOP6. The black dashed line identify the local sunrise (08:45) and the completed wind rotation at WS2 (09:40) respectively*

the WS2. Moving south-west towards the WS1, the downslope undergoes a slight rotation clockwise, becoming more easterly. Each tower level presents a slightly clockwise rotation of the wind direction with increasing height too. In fact, the wind oscillates around the southeast in the highest level of the WS2 (20 m) while the wind direction at the WS1 highest level (32 m) is more southerly, still turning clockwise compared to the WS2. The presence of a strong directional wind shear, caused by the interaction between the downslope and the down-valley mentioned in section 4.1, is also found in the east slope (Lehner et al., 2015) and in the Salt Lake Valley (Whiteman and Zhong, 2008). As a result, the downslope speed maximum blow at an angle relative to the local downslope topography gradient.

Two disturbances are visible in the IOP2, based on the rotation of the wind, the first one between 03:00-05:00 MDT and the second one between 06:00-07:00 MDT. The two IOP2 disturbances are similar, although the first is characterized by a complete rotation of the wind direction at WS1 that is not present on the second one. In figure 4.8 the 30 minutes average wind vectors and temperature at 2m AGL map shows the nocturnal wind and temperature development on IOP2. In this way it is possible to observe the wind and temperature variations neglecting the small ones. During both disturbances on IOP2, the downslope runs over the towers, interacting with (and progressively replacing) the down-valley wind. The surface temperature at WS2, on the steepest part of the slope, is higher than that at WS1 at that time. The temperature rising associated with the presence of the downslope during the night is due to a warm advection cased by the mixing with the warmer air from above (Papadopoulos and Helmis, 1999) and by compressional warming during the flow descent (Fleagle, 1950). Then, as the down-valley wind blowing from the south converges rapidly with the northeasterly downslope, the resulting 30 minutes averaged wind rotates from southeast and the colder air moves up the slope, also pushed by the westerly valley inversion (this is the westerly wind visible in the disturbances at around 03:30 MDT at WS1 and around 06:30 MDT at WS2), causing a temperature drop first on the WS1 and then on the WS2, as it is visible from IOP2 time series between 04:30 and 05:00 MDT.

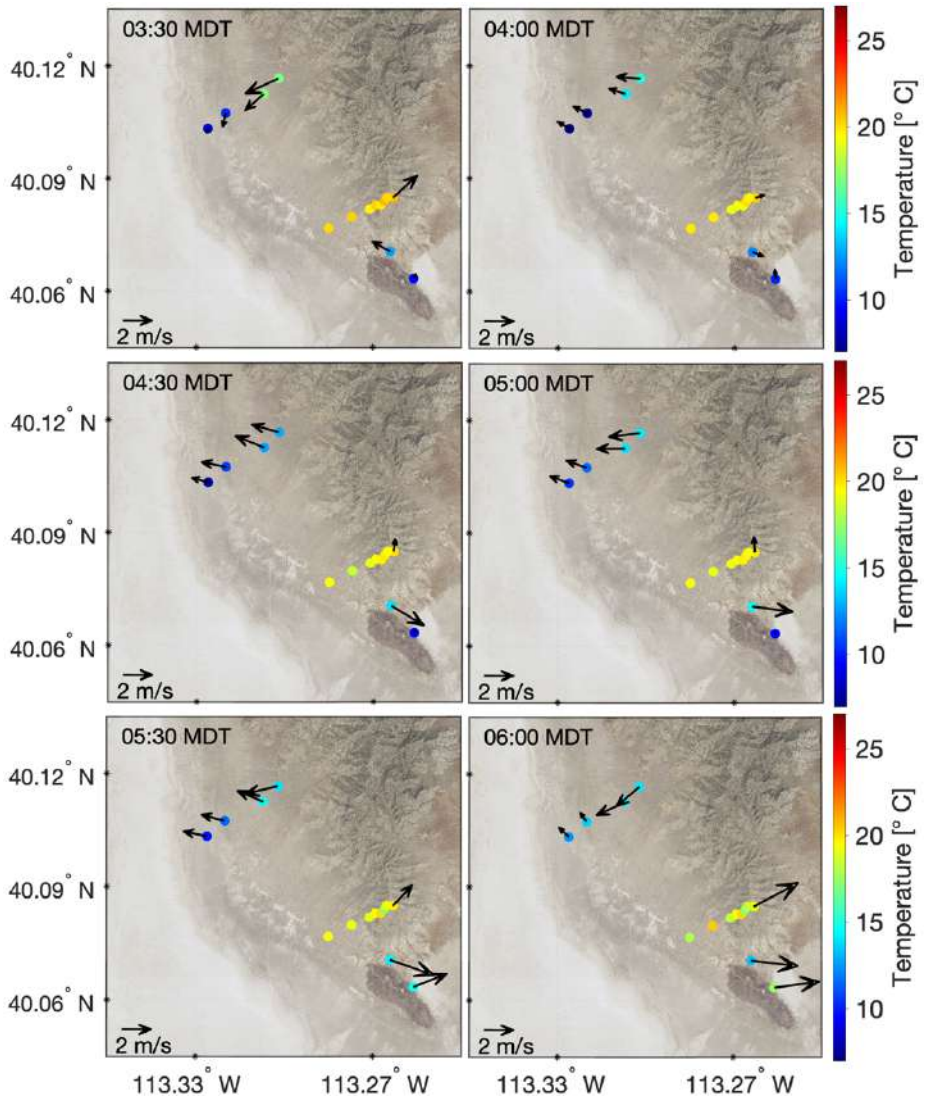

Figure 4.8: *30 minutes averaged wind vectors and temperature at 2 m during the late night of the 2 October 2012 (IOP2). In the upper part, starting from the right and going to the west, we find WS2 (1374 m ASL), SAMS31, WS1 and PWIDS59 (1309 m AGL). In the southern part are shown in line on the right the eight HOBOs temperature data-logger (the lowermost is the HOBO1 at 1325 m ASL and the topmost is the eighth, at 1657 m ASL), beyond which there is the PWIDS86 (on top, at 1636 m). The last two instruments are the sonic towers SG1 and SG2 (the latter is the southernmost instrument on the map). Note the extremely different temperature between the towers site and the HOBOs site, dew to their different altitude and exposure to the cold down-valley, with respect to the towers site. However, the lack of wind sensor on this area makes it difficult to understand this temperature differences.*

On the contrary, IOP6 appears to be less disturbed and all variables proceed with an oscillatory behavior, except for a relevant speed drop at WS1. This behavior and the absence of large disturbances could be caused by the high relative humidity, as a result of the increase in evaporation rate after the rainfall on 13 October 2012 (Hang et al., 2016). Sastre et al. (2015) found that the increased humidity at the surface would directly trigger lower cooling. In addition, looking at the occurrence of katabatic flows, they found more intense but less frequent katabatic events at the driest site of their experiment. Simulations of Banta and Gannon (1995) shows that the increased soil thermal conductivity, due to high values of soil moisture, allows for heat exchange with a deeper layer of soil and effectively reduces the cooling at the slope surface. The reduced near-surface cooling is responsible for reducing the strength of the katabatic flow. However, Jensen et al. (2017) have obtained contrasting results regarding the influence of humidity on the katabatic flow of the east slope, despite being unable neither to validate nor reject the findings of Banta and Gannon (1995). The IOP6 shows lower wind speed with smaller fluctuations than IOP2, a quite undisturbed surface inversion at WS1, especially in the lowest levels (0.5 and 2 m AGL) and some fluctuations in the WS2 temperature. The wind direction is quite undisturbed with a down-valley predominance above and a downslope predominance below. Moreover, as the IOP2 is an earlier autumn day, we aspect the temperature to be lower in the IOP6, as confirmed by data. However, temperature gradient reaches at most 4.5°C between the 0.5 m and 20 m AGL level at WS2 on IOP6 with respect to the 6°C temperature gradient at WS2 on IOP2 (temperature gradient at WS1 are not compared because of the lack of thermohygrometers data on IOP2). Thus, on IOP2 the stronger temperature gradient is associated with larger wind speed and direction variability and a more intense and more frequent katabatic events, in accordance with the work of Banta and Gannon (1995) but in contrast with Sastre et al. (2015). On IOP6 the only notable disturbance is the one visible around 06:00 MDT. Initially there is a wind speed decrease on the WS2 some minutes before 05:00 MDT, with the exception of 2 m and 5 m AGL levels. The WS2 is reached by the downslope, as evidenced by the easterly-northeasterly wind below the 10 m AGL level. Even the level at 10 m and 20 m AGL undergo a rotation to the east but with a very low wind speed, under 1 m/s. The cold down-valley is therefore replaced by downslope and this

causes a temperature increase of 2.5°C in 30 minutes from the 5 m AGL level up. The easterly-northeasterly downslope reaches the WS1 around 5:00 MDT, turning the wind and hindering the down-valley. This causes a temperature increase of at least 3 degrees in 30 minutes. The temperature increase is more pronounced in the 5 m AGL level on which the downslope has the maximum speed. However, all levels experience a decrease in speed during the rotation, especially the levels above 5 m AGL. After 06:00 MDT, as the wind turns southeasterly again on the WS1, the wind speed increases and the temperature drops. On the WS2, the downslope persists with higher speeds between 2 m and 5 m AGL and the temperature remains higher until 07:00 MDT, when the southeasterly downslope reach the tower again.

4.2.2.2 Period 2 - The onset of the nocturnal temperature inversion erosion and the arrival of the diffuse radiation

Two different types of erosion of the nocturnal temperature inversion are observed in the two fall IOPs analysed. In this period, the analysis starts at WS1 first, following the surface temperature inversion erosion which during the IOP2 takes place at this tower first.

Period 2 on IOP2 spans from 06:55 MDT to 08:10 MDT. The temperature rise starts from the WS1 around 06:50 MDT (Fig. 4.9), 40 minutes before astronomical sunrise, although the absence of thermohygrometer data makes the temperature on the WS1 quite unreliable. For this reason, we are not able to establish an exact onset time of temperature rise, which would help to identify how far in advance the direct radiation reaches the WS1 with respect to the WS2. However the nocturnal thermal inversion at WS1 seems to last until local sunrise at WS2, as the 2 m AGL temperature overcame the 32 m AGL temperature. Despite some fluctuations in the wind direction, the directional wind shear is clearly visible: as stated earlier, the lower level has an easterly wind and, going up along the tower, the wind direction rotates clockwise until the southerly wind at 32 m AGL level. At the end of this period, as the erosion of the nocturnal temperature inversion at WS1 is completed, the initiation of the transition is already taking place, only on this tower. For this reason, on this tower the Period 2 ends at 08:10 MDT and not at local sunrise at WS2. The description of the transition is postponed to the section

4.2.2.3, which addresses the features of the transition at every towers .

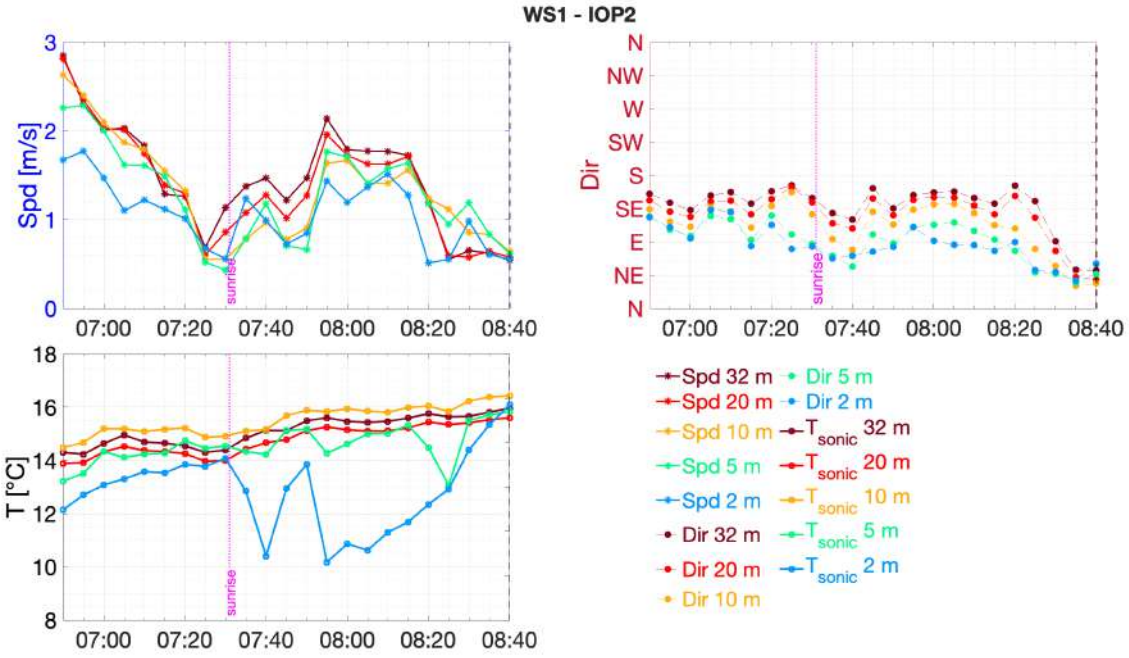

Figure 4.9: *Time series zoom on 2 October 2012 at WS1 during the period 2. Times are in local time (MDT)*

At WS2 (Fig. 4.10) the temperature shows a weak increase only in the 5 m AGL level, starting from 07:05 MDT, and an even weaker and temporary increase at 2 m AGL. The wind speed decreases slightly and the maximum speed is concentrated between 5 m and 2 m AGL. In these levels there is mainly a downslope, but where the southeasterly flow is predominant, the temperature stays constant. Figure 4.11 shows the 5 minutes average potential temperature vertical profile at WS2 before the morning transition takes place. The 05:45 MDT profile identifies one of the moments during which the surface inversion strength is maximum (i.e., $\theta_{20m} - \theta_{0.5m} = 5.9K$). Potential temperature shown up to 08:40 MDT (that is local sunrise time) exhibits a stable profile, which is typical of both the nocturnal period (Stull, 2015) and even the preceding morning transition period The temperature at 0.5 m AGL and 20 m AGL is almost constant between 07:05-08:45 MDT, while a very slight warming is observed mainly at 5 m AGL. At this height, as mentioned earlier, there is a downslope flow and the maximum wind speed. Thus in this case the warming associated to the presence of the downslope is modest and does not produce a

substantial temperature rise along the tower, except for the heating at 5 m AGL of 2.3 K

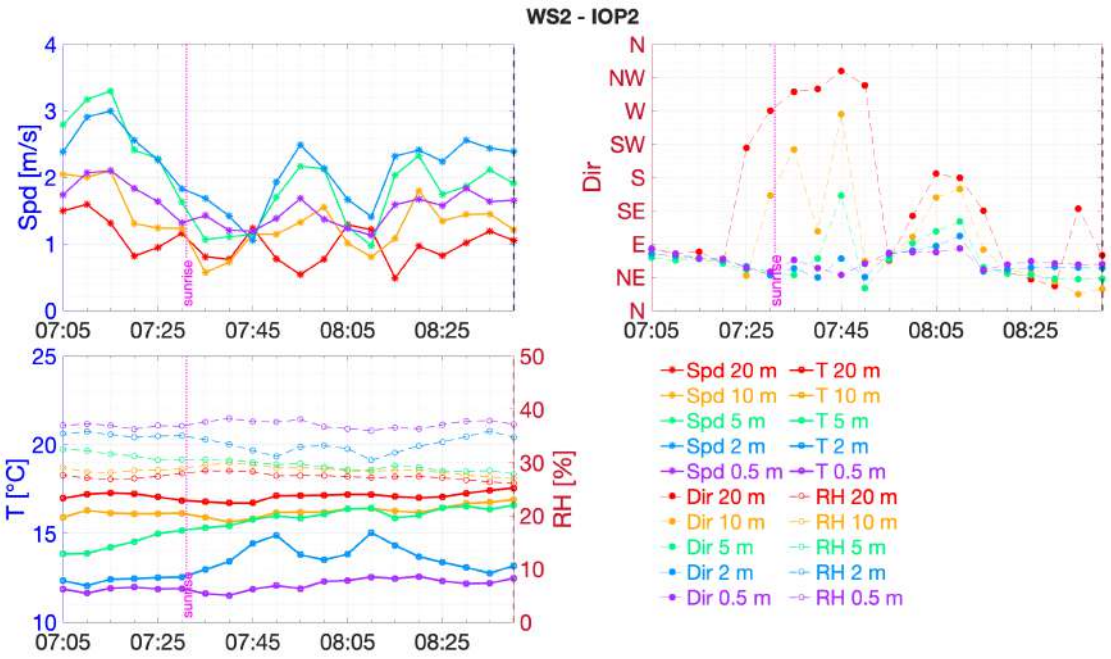

Figure 4.10: *Time series zoom on 2 October 2012 at WS2 during the period 2. Times are in local time (MDT)*

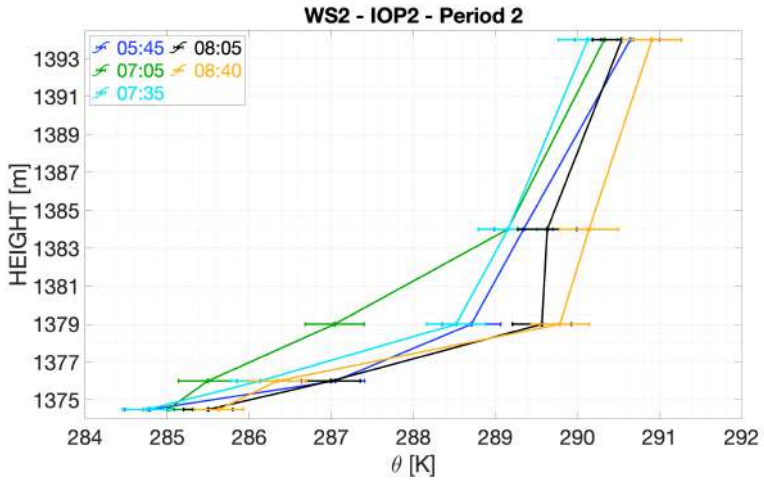

Figure 4.11: *Vertical profile of 10 minutes averaged potential temperature at WS2 on IOP2*

and of 1.5 k at 2 m AGL between 07:05-08:40 MDT, where the downslope is concentrated. To sum up, on IOP2 the temperature increase on the WS1 may depend on the arrival

of the radiation, which triggers a surface air heating, indicating that the onset of the warming is on the less steep part of the gentle west slope. The WS2 is less affected by the warming during this period.

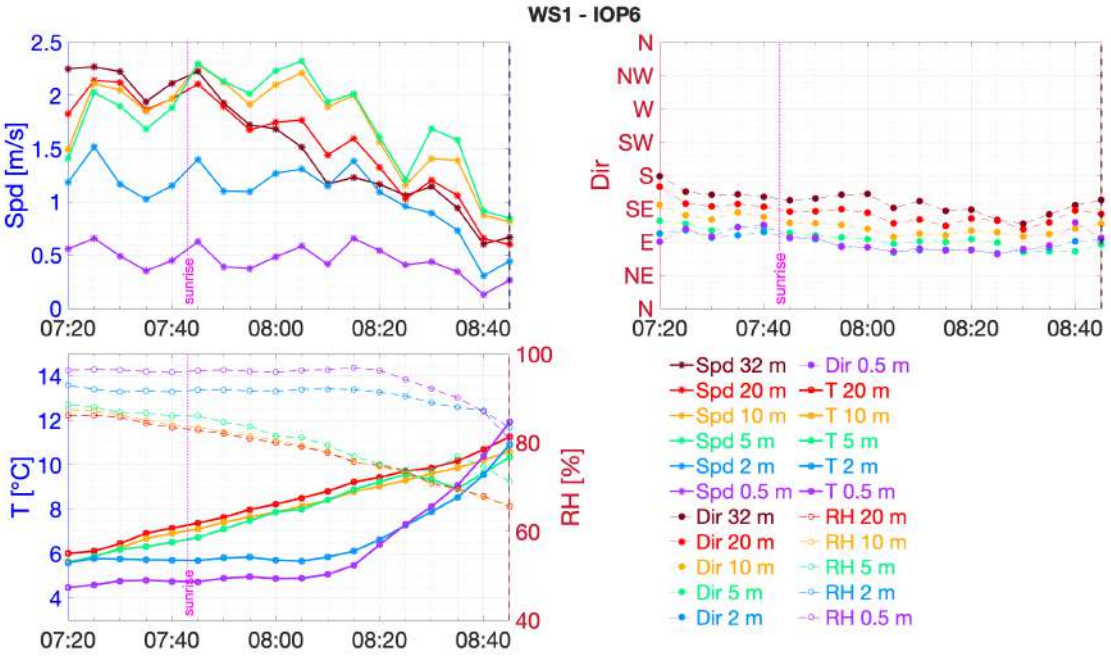

Figure 4.12: *Time series zoom on 14 October 2012 at WS1 during the period 2. Times are in local time (MDT)*

Period 2 on IOP6 spans from 07:20 to 08:45 MDT (i.e., local sunrise at WS2) The temperature rise on IOP6 starts, as opposed to the IOP2, at both towers at 07:20, about 20 minutes before astronomical sunrise (07:43 MDT) (Fig. 4.14 and fig. 4.12). The warming at WS1 is visible only from the 5 m AGL level up. The levels closer to the ground, indeed, show a constant temperature until 08:10 MDT, when the warming starts at 2 m and 0.5 m AGL simultaneously but at an higher rate at 0.5 m AGL. The wind direction shear is clearly visible here, as in the IOP2 at WS1, but in this case the wind direction is almost undisturbed and the speed is quite low. The maximum wind speed is 2.5 m/s at 5 m AGL, and the 10 m, 20 m and 32 m AGL speed values are found to be very close to it. The warming is concentrated in the layer with the wind speed maximum. Approaching astronomical sunrise the wind speed drops below 1 m/s. Looking at figure 4.13 the nocturnal profile (that is, the profile belonging to the Period 1 at 06:30 MDT)

shows an inversion strength of 3.5 K. Starting at 07:20 MDT, the heating at the top is

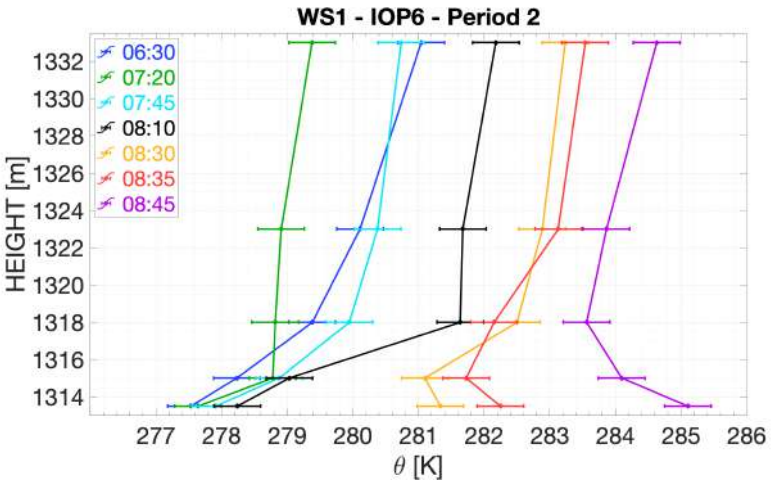

Figure 4.13: *Vertical profile of potential temperature on IOP6 at WS1. Times are in local time (MDT)*

initially more efficient than that at the surface until 08:10 MDT, contrary to what is seen at WS1 on IOP2, if the sonic temperature measurements validity is not disputed. The stable profile is found below 5 m AGL at 08:10 MDT, above which there is an almost neutral profile. Then, the temperature begins to rise also near the surface and with a rate higher than that above 5 m AGL. However the temperature still rises in the higher levels too. At 08:30 MDT the potential temperature profile becomes unstable under 2 m AGL. Between 08:30-08:35 MDT the 5 m AGL level undergoes a temporary slight cooling, as if the surface heating raises slightly higher the cooler air that stood near the ground until that moment. This cool air remains trapped due to the presence of warmer air above it. At 08:45 the surface temperature exceeds that at 20 m AGL. Surface heating begins to erode the nocturnal inversion from below, but the cooler air trapped in the mid levels keeps the profile stable between 5 m and 20 m AGL.

As already said, temperature increase starts at 07:20 MDT also at the WS2. At this tower a slight warming starts from the highest level (i.e., 20 m AGL). The temperature rise propagates down along the tower level, with a delay of 5 minutes each depending on the time interval used for the average, except for the 0.5 m AGL that continues to cool until exactly the astronomical sunrise (07:43 MDT) and except for the 5 m and 10 m AGL which have the same temperature and rise together. In addition, the temperature increases

by the same rate, ≈ 0.2°C/5 min, in each level, keeping the inversion strength almost unchanged until 08:00. During this phase the wind direction spans from southeasterly above and from easterly below. Then, at 08:05 MDT, the temperature above 10 m AGL experiences a rapid increase of about 1.5°C while the 2 m and 5 m AGL temperatures

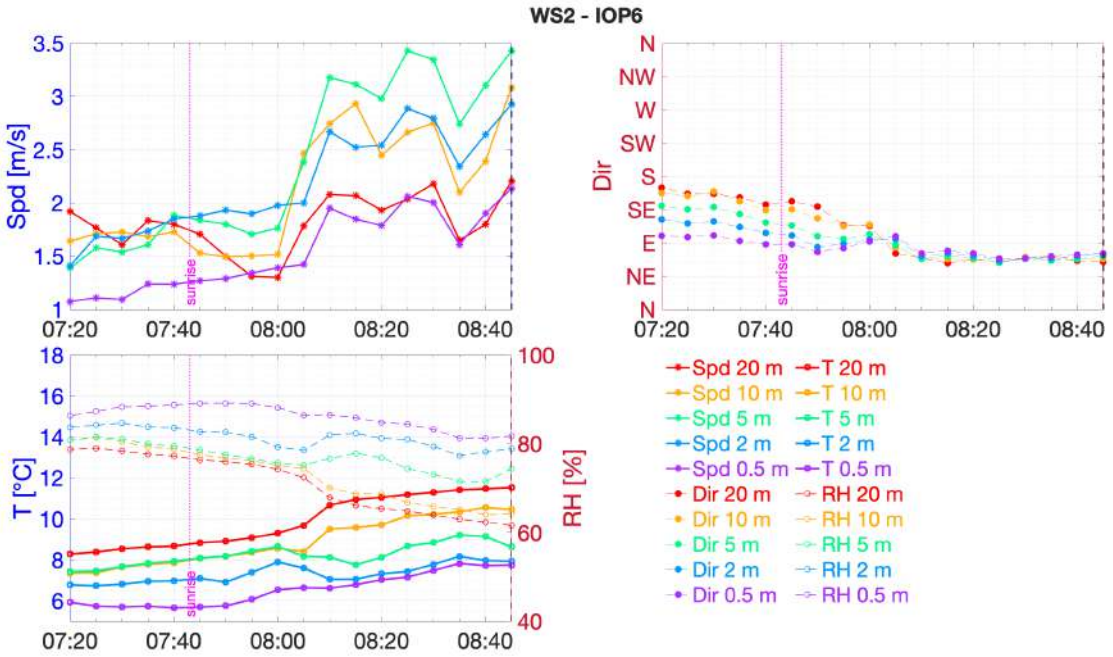

Figure 4.14: *Time series zoom on 14 October 2012 at WS2 during the period 2. Times are in local time (MDT)*

undergo a temporary slight decrease until 08:15 MDT. The wind, at the same time, rotates progressively from the southeasterly down-valley to the easterly-northeasterly downslope along all the tower levels, with a speed increase that is maximum at 5 m AGL, above 3 m/s. This clear wind rotation is not visible on the IOP2. After that, the temperature in all levels goes up again at the previous rate. Thus in this case the downslope reinforcement is responsible for a warming that raises the temperature above the nocturnal average values along all tower levels. The warming associated with downslope strengthening starting from the upper level of the WS2 could be explained by the heating occurring on some sections of the steepest part of the slope due to the direct solar radiation arrival in that area. This causes a warm advection from the upper part of the slope to the colder lower portion in a similar way to what happens on a gentle

east-facing slope (Papadopoulos and Helmis, 1999). In figure 4.15 the potential

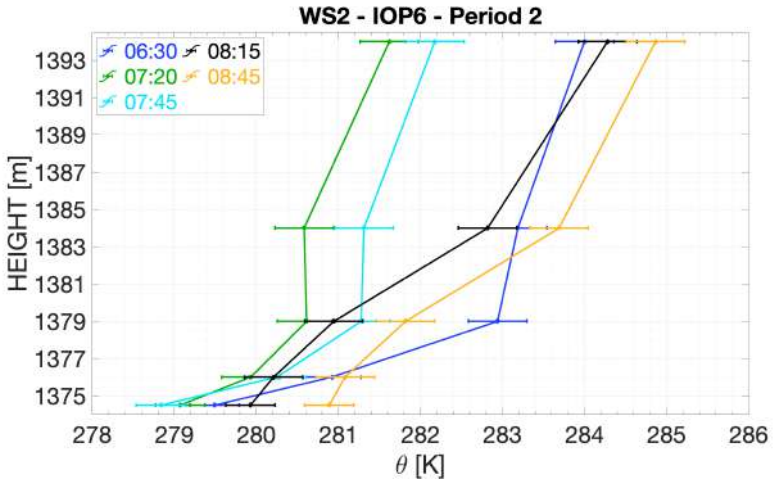

Figure 4.15: *Vertical profile of potential temperature on IOP6 at WS2. Times are in local time (MDT)*

temperature vertical profile, starting from the one with the stable nocturnal profile and the maximum inversion strength at 06:30 MDT(i.e., $\theta_{20m} - \theta_{0.5m} = 4.5K$). Between 07:20-08:45 MDT the heating is concentrated in the layers above 5 m AGL. The neutral profile visible up to 7:45 MDT between 5 m and 10 m AGL becomes very stable, as the heating at the top due to mixing with the overlying air reaches 5 m AGL, below which the warming due to surface heating is very small. The upper warming due to mixing with the overlying air is what Papadopoulos and Helmis (1999) called the top-down dilution which has been observed during the morning temperature inversion erosion on an east-facing slope. At 08:15, during the temporary slight cooling at 5 m AGL, the temperature increases by 2.5 K at 20 m AGL while at 0.5 m only by 1.1 K, with respect to the 07:20 profile. This cool air lifted up from the ground by surface heating, remains trapped due to the presence of warmer air above, as seen at the WS1 at 08:35. Thus, on IOP6, the warming is concentrated in the upper layers at both towers, suggesting the presence of horizontal heat transfer from the heated slope (De Wekker and Kossmann (2015) and Princevac and Fernando (2008)).

4.2.2.3 Period 3 - The morning transition

The Period 3 start at the WS2 local sunrise time and addresses the description of the morning transition, that is the rotation of the wind direction from downslope/down-valley to upslope/up-valley. We start from the description of the wind rotation at the WS1 on IOP2, which is the first to take place, as seen in the section 4.2.2.2. Since, only in this case, the rotation begins during the end of the Period 2, the time series and their description start 30 minutes before the local sunrise on the WS2. Looking at the time series in figure 4.16 the wind rotates from easterly to northeasterly starting from the level

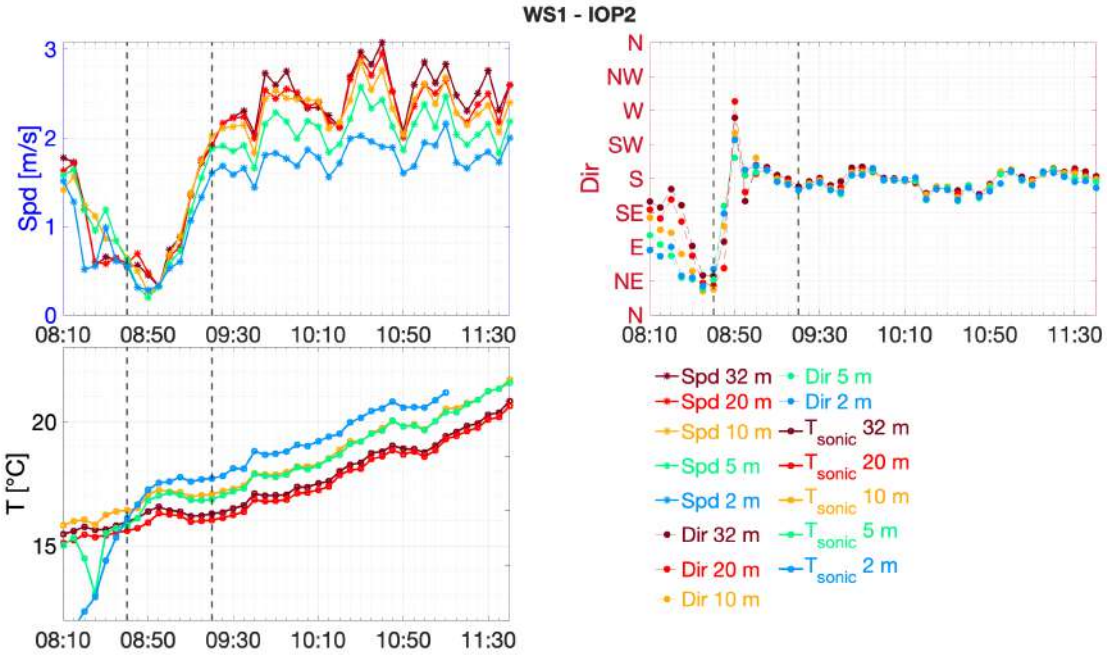

Figure 4.16: *Time series zoom on 2 October 2012 at WS1 during the Period 3 Times are in local time (MDT)*

at 10 m at 08:10 followed by the 5 m and 2 m AGL. The rotation proceeds going up along the tower levels, until the last level, at 32 m AGL, which turns from a southeasterly to a northeasterly wind starting from 08:20 MDT. At 08:40 the transition from the nocturnal downslope to the diurnal flow takes place suddenly, starting from the level at 2 m AGL. At 08:50 the wind is southerly-southwesterly at 5 m AGL and westerly-northwesterly at 20 m AGL. The other levels shows intermediate directions. Then, at 08:55 MDT a second abrupt but less wide rotation is observed at 20 and 32 m AGL, from the south-southeast

while at 2 m and 5 m AGL the transition is already concluded. At 09:00, five minutes later, the transition is over even at 20 m and 32 m AGL. The wind is coming southerly from now on, with very small fluctuations around this direction. The transition from southeasterly to a southerly wind takes place in 45-50 minutes, depending on which level is taken into account. These very large fluctuations in the wind direction during the transition can be explained by the extremely low wind speed, which is close to 0 m/s at the transition onset and always below 1 m/s during the entire process. This behavior is observed at this tower on this IOP only. The other transitions take place much more gradually and in longer times, or rapidly but with higher wind speed, as we will see soon. During the transition the wind speed drops in every levels, experiencing the so-called "morning calm period". The section aimed to its description is the 4.2.2.5. The speed drop is followed by a rapid increase in wind speed, which, at the end of the transition, has higher speeds going up along the tower levels. However, the wind speed maximum stays below the nocturnal one.

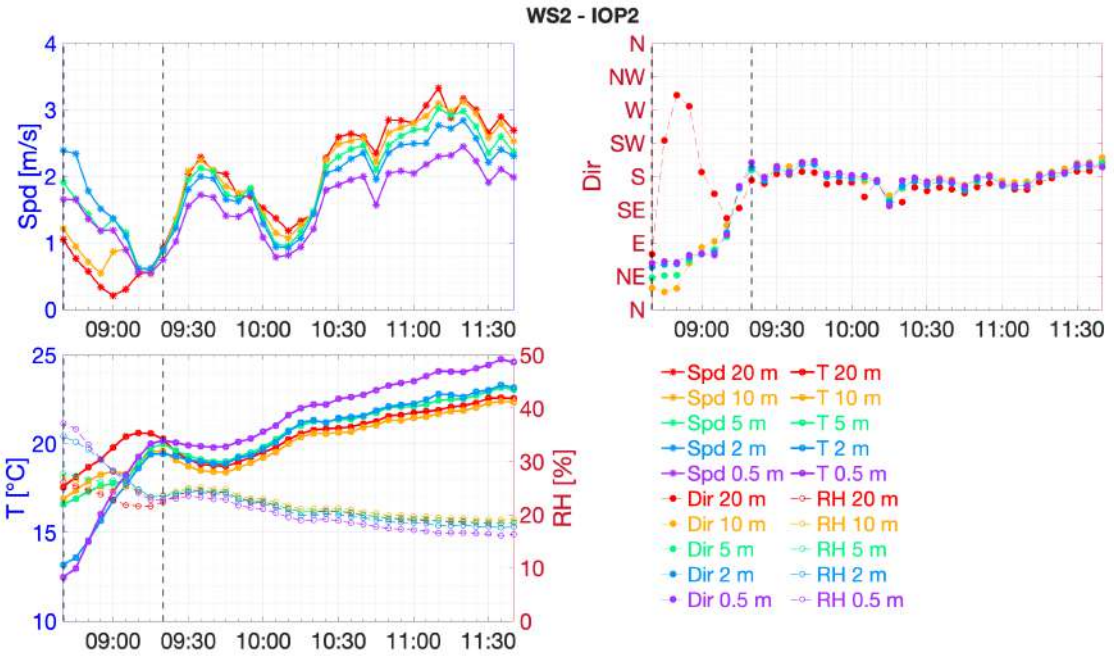

Figure 4.17: *Time series zoom on 2 October 2012 at WS2 during the Period 3. Times are in local time (MDT)*

At the WS2 (Fig. 4.17) the wind is easterly-northeasterly at 0.5 m and 2 m AGL at

08:40 MDT (local sunrise at this tower), while an counterclockwise rotation is observed going up along the tower levels, contrary to what is usually observed, until the 10 m AGL which has a northerly-northeasterly wind. At 20 m AGL the wind becomes westerly but with a wind speed below 1 m/s. However, this wind configuration is temporary. As the wind speed already drops, the transition begins at 08:55 MDT, 45 minutes after the transition onset at WS1, starting from the 5 m and 10 m AGL level that have the more northeasterly direction. At 09:10 MDT the 20 m level wind has the same direction as the others and at 09:20 the rotation from a northeasterly to a southerly wind is over, 20 minutes after the end of the WS1 wind rotation, revealing an up-slope propagation of the transition development. The speed drop is followed by a rapid increase in wind speed, which, at the end of the transition, has higher speeds going up along the tower levels but with a weaker shear with respect to the WS1. At WS2 the transition takes a shorter time than that at WS1, showing a 25 minutes length. As a the similar heating process from below is visible at both tower, the different duration of the transition depends exclusively on the different position of the towers along the slope, which makes the warming onset starting from the flattest part of the slope. The vertical profiles of potential temperature in figure 4.18 during the Period 3 clearly show that the warming and the consequently erosion of the nocturnal temperature inversion are concentrated in the layer below 5 m AGL. The surface heating due to the solar radiation absorption occurs after local sunrise

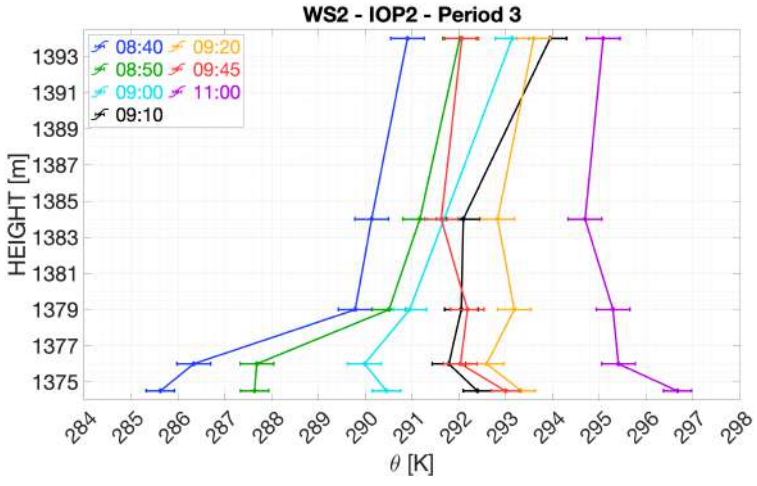

Figure 4.18: *Vertical profile of potential temperature on IOP2 at WS2 during the Period 3. Times are in local time (MDT)*

at 08:40 is the most responsible for heating the near-surface air layers. In fact, between 08:40-09:00 MDT, as the potential temperature profile that has been so far stable becomes unstable between 0.5 m and 2 m AGL, the temperature rises of 4.8 K at 0.5 m AGL, 1.1 K at 5 m AGL and 2.2 K at 20 m AGL. Between 09:00-09:10 MDT the heating rate continues to be greater near the surface than above 10 m AGL. Then, between 09:20-09:45 MDT a temporary cooling, especially from 2 m AGL up but even near the surface, which can be attributed to the arrival of cool air carried by southerly wind activated just after the transition. The 11:00 MDT profile is an example of the early morning potential temperature profile. It shows that the unstable stratification is growing from the surface up, above which there is a shallow unstable profile topped by the stable profile which as not already eroded. To sum up, on IOP2 the warming process and thus the transition is triggered by surface heating starting from the flattest part of the west slope. This type of temperature inversion destruction resemble the one that occurs over flat terrain and leads to an upward growth of the CBL (Whiteman (1982) and De Wekker and Kossmann (2015))

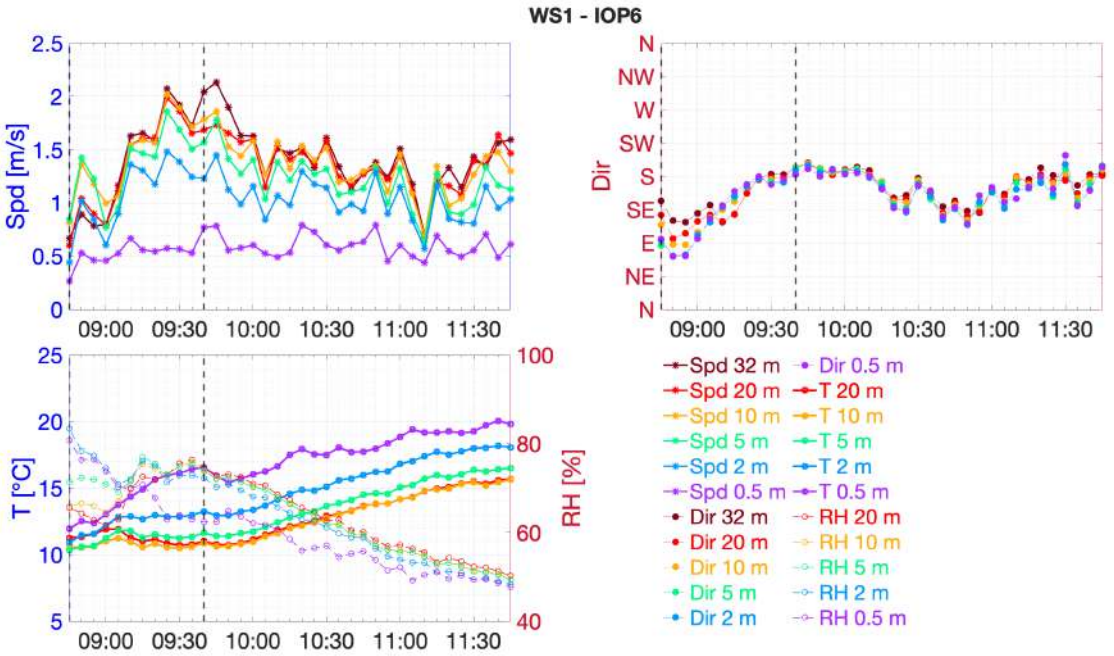

Figure 4.19: *Time series zoom on 14 October 2012 at WS1 during the period 3. Times are in local time (MDT)*

Period 3 on IOP6 spans from 08:40 MDT (that is local sunrise at WS2) to the end of the 10-hours range of data analyzed, around 11:30 MDT. On IOP6 at 08:45 (i.e., the final time instant of Period 2) the WS1 surface temperature inversion is already eroded, since the 0.5 m AGL temperature exceeds that at 20 m AGL. Looking at the time serie of period 3 (Fig. 4.19), the wind speed, dropped below 1 m/s at the end of Period 2, halts and begins to rise steadily. The wind direction shear, seen before, lasts until 09:00 MDT, when the wind rotation starts in every level simultaneously. The transition takes place gradually and is not as abrupt as in the IOP2, and is accompanied by an increase in wind speed. At 09:40 the transition is over, the wind is from the south and the wind speed reaches a maximum at 32 m AGL of $\approx$ 2 m/s. The wind speed has the same shear of the IOP2 but, after 09:40 MDT, with a lower values, below 1.5 m/s. Vertical profiles of potential temperature, shown in figure 4.20, exhibit a strong near-surface heating which propagates along the levels. The stable potential temperature profile above 5 m AGL is gradually eroded from below, as the surface warming rises the cooler air upwards, as shown by the slight temperature decrease above 10 m AGL between 09:05-09:40 MDT At 11:00 MDT the stable layer has been almost completely eroded even above 10 m AGL.

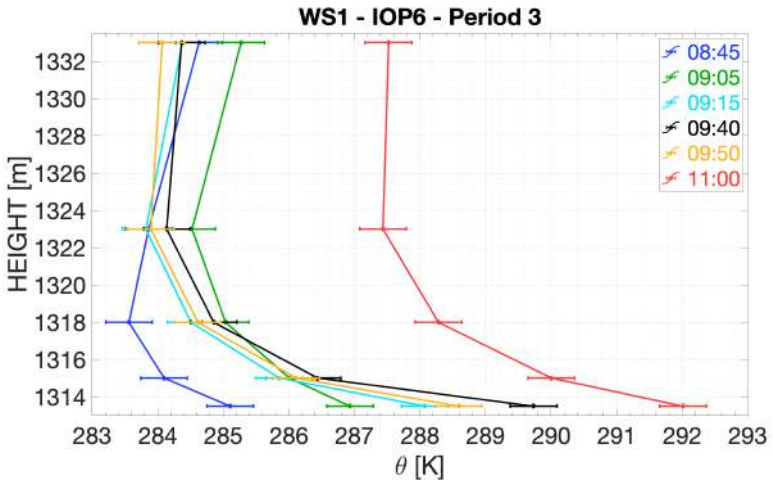

Figure 4.20: *Vertical profile of potential temperature on IOP6 at WS1 during the Period 3. Times are in local time (MDT)*

At WS2 on IOP6 the heating rate increases sharply with the arrival of direct radiation (i.e., at local sunrise at 08:45 MDT), especially in the levels closer to the ground (Fig. 4.21). At the same time the wind speed decreases gradually along all the tower levels,

always showing the highest speed at 5 m AGL. The easterly-northeasterly downslope is still present. The temperature at 0.5 m AGL exceeds that at 20 m AGL at 09:30, 45 minutes after the surface inversion break-up at WS1. Then between 09:35-09:40 MDT, a

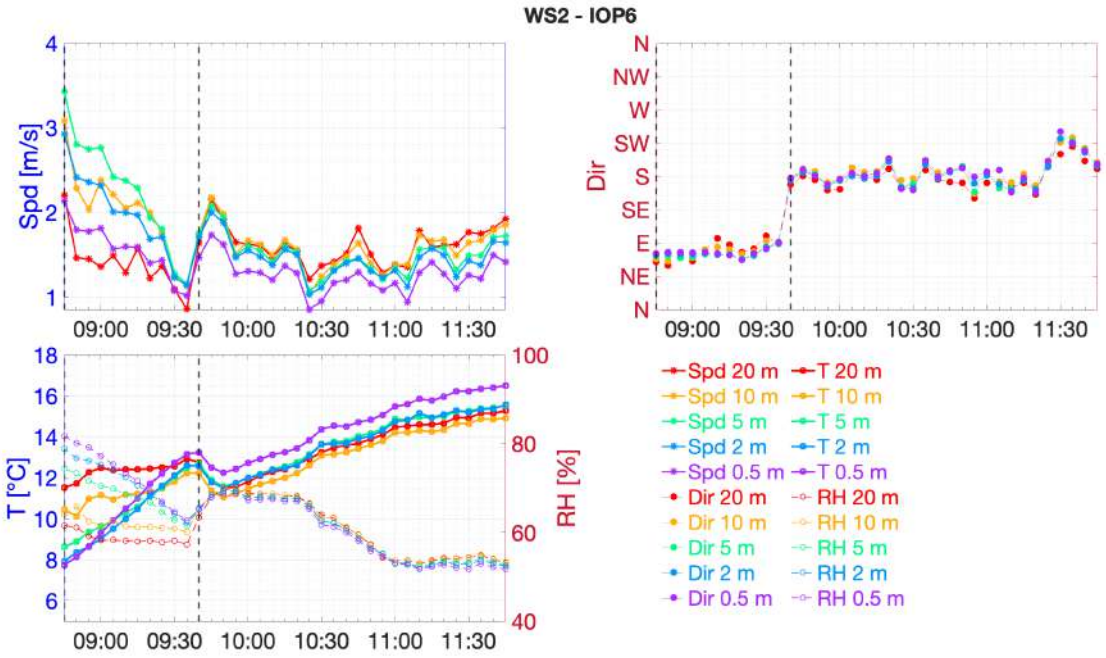

Figure 4.21: *Time series zoom on 14 October 2012 at WS2 during the period 2. Times are in local time (MDT)*

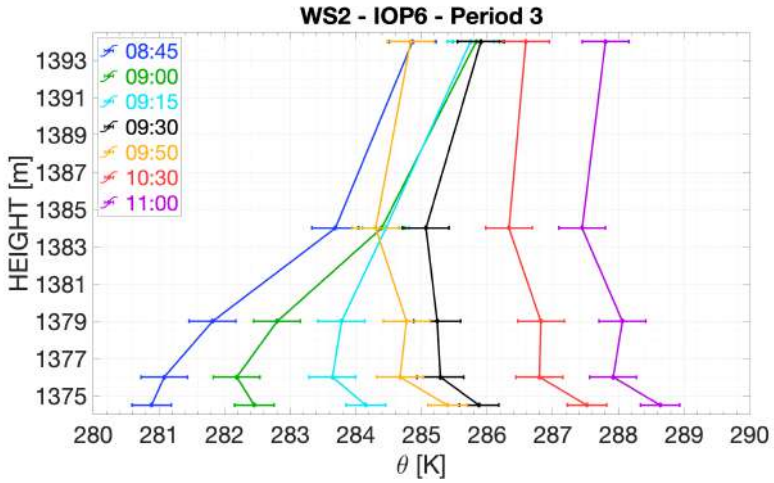

Figure 4.22: *Vertical profile of potential temperature on IOP6 at WS2 during the Period 3. Times are in local time (MDT)*

very fast wind rotation takes place, which ends at the same time as it ended on the other tower. Between 09:40-09:55 MDT a temporary cooling take places along the tower, exactly as seen in the IOP2 on this tower. As already said, it can be attributed to the arrival of cool air carried by southerly wind activated just after the transition. After the initial cooling from above, experienced during the Period 2, potential temperature profiles (Fig. 4.22) shows the erosion of the nocturnal temperature inversion from below. Between the local sunrise (08:45 MDT) and the end of the transition (09:30 MDT) the temperature increases of only 1 K at 20 m AGL, while at 0.5 m AGL temperature rise of 5 k. At 09:50 MDT is visible the temperature drop,due to the activation of the southerly wind, especially at 20 m AGL. The last two potential temperature profile exhibit a quite unstable stratification, although the presence of some small temperature fluctuations and the absence of an heating as efficient as that on the WS1, causing a neutral and at times slightly stable stratification above 2 m AGL. To summarise, on IOP6 the initial heating from above visible during Period 2, is gradually replaced by the efficient heating from the surface. The transition starts at all levels contemporaneously, in contrast to what is observed on IOP2, where the extremely efficient surface heating triggers the transition from below at both towers. Thus, on IOP2, the diurnal warming and the transition are driven firstly by horizontal heat transfer from the slope and then by surface heating, but only after local sunrise.

4.2.2.4 Early morning surface wind on the west slope

An important feature must be emphasized at the end of period 3, i.e. after the transition ending at each tower. Usually, as stated by theory, the morning transition marks the beginning of the diurnal circulation associated with the development of an upslope flow in the near-surface layer that becomes an up-valley flow during the daytime. However, on the west slope the wind blows from the south in the early morning, possibly flowing once again from the valleys south of the Granite Mountain. In fact, during the night and before the morning transition the southeasterly flow on the west slope arises from the interaction between the southerly down-valley from the valley south of the Granite Mountain and the easterly-northeasterly downslope (as seen in section 4.1), After the transition, the southerly down-valley does no undergoes any deviation, blowing

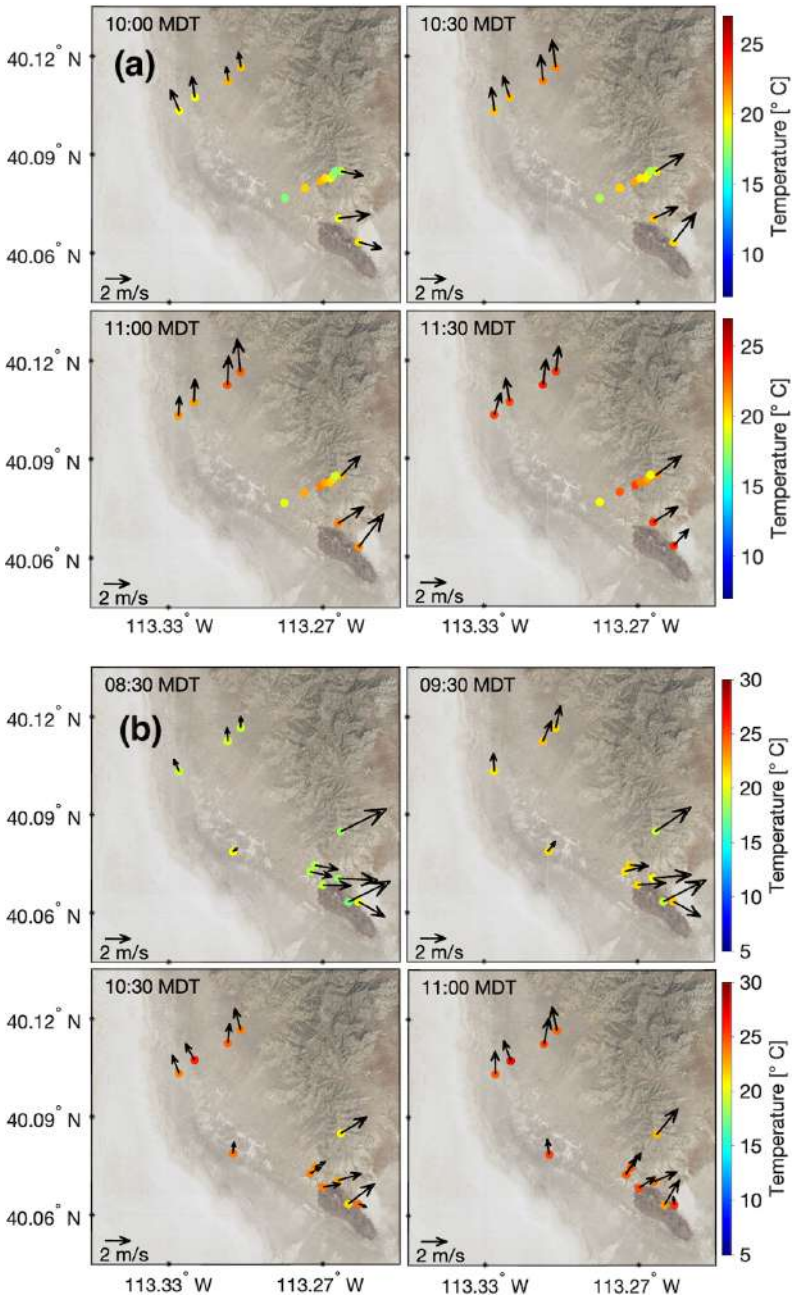

Figure 4.23: *30 minutes averaged wind vectors and temperature at 2 m during the early morning on IOP2 (a) and IOP4 (b). Instruments shows on IOP2 are the same as fig. 4.8. On IOP4: the HOBOs are not present, PWIDS53 is located southwest of the slope and near the Small Gap (south fo the Granite Mountain) are found PWIDS61, PWIDS63, PWIDS64, SG1, SG2, SG3.*

undisturbed from the south. Due to its direction, this early morning wind cannot be an upslope, that for opposition to the downslope should comes from the southwest, and not even an up-valley, which for opposition to the down-valley should comes from the northwest. The persistence of the down-valley wind during the early morning is observed for example by Papadopoulos and Helmis (1999) and is also reported by De Wekker and Kossmann (2015).

4.2.2.5 The morning calm period

During the morning and the evening transition, the winds undergo a quiescent period that is called "morning (or evening) calm period" (De Wekker and Kossmann, 2015). Usually the calm period has large variability in terms of duration, and the reason are still unclear. According to Nadeau et al., 2020, during the morning transition this period takes place between local sunrise and the onset of the upslope/up-valley winds, when wind speeds are below 1 m/s. In their work, they consider the speed drop at 1.5 m AGL. Nevertheless, considering in our data the presence of the wind speed shear and on the basis of the usual occurrence of the wind speed maximum at 5 m AGL due to the downslope presence before the transition, we choose to analyze the wind speed drop at this level.

On 2 October (IOP2) the morning calm period with a 5 m AGL speed below 1 m/s lasts 30 minutes at WS1 (08:35-09:05 MDT) and 15 minutes at WS2 (09:10-09:25 MDT).The morning calm period at both towers covers the second half of the transition and ends 5 minutes after the transition is over. The onset of the morning calm period at WS2 is 5 minutes after the end of the WS1 speed drop. On 14 October (IOP6) the mean speed is higher than that on IOP2, so the wind speed never drops below 1 m/s at 5 m AGL, except for two single moments, at 08:45 and 09:00 MDT, at the WS1. However, since a wind speed drop is present on IOP6 too, choosing as a threshold 1.5 m/s, the morning calm period lasts 30 minutes at WS1 (08:40-09:10 MDT), and 10 minutes at WS2 (09:30-09:40 MDT), on which the drop occurs 20 minutes after. In this case the morning calm period starts before the onset of the transition, ending 10 minutes after the onset of the transition at WS1. At WS2 the morning calm period and the transition end together. Thus the occurrence of the morning calm period seems

to depends on the heating mechanism, showing an earlier occurrence when the surface heating is predominant (that is on IOP2) with respect to the warming of the air from above (i.e, on IOP6).

4.2.2.6 TKE and its components

This section addresses the TKE and its components description during the morning transition time. Given the focus only on the morning transition processes, the TKE and its components time series in figure 4.24 and 4.25 do not show the entire analyzed period of section 4.2.2.1

Before local sunrise, when the slope-normal component is very small due to stable stratification and the TKE results mainly from the other two components, the spanwise component at WS1 (Fig. 4.24(g) and fig. 4.25(g)) is the most similar to the TKE, emphasizing the importance of the valley influence on this tower. At the same time, the streamwise component (Fig. 4.25(b)) at WS2 is almost equal to the TKE, which confirms the presence of a stronger slope regime at this tower. During this same period, the TKE is on average larger and more variable during the IOP2, which in fact is the one that has the greatest fluctuations of wind speed and direction. In this context, an high and very localized increase in the TKE at WS2 on IOP2, which has been cut to preserve the signals resolution detail, is observed between 06:00-06:30 MDT which is visible in both the TKE and its streamwise components, and corresponds to the second of the two nocturnal fluctuations that occur during the IOP2 (Section 4.2.2.1). At WS1 there are also significant variations in TKE around this time, but the variation in this case is mostly visible in the spanwise component and is very similar to the wind speed fluctuations on this tower.

Around astronomical sunrise the TKE and its components drop. On IOP2 at WS1 they reach the minimum around local sunrise (local sunrise is referred to WS2 as usual) as soon as the transition starts on this tower and at the wind speed minimum is reached. At WS2 the minimum values are found a little later, during exactly the wind speed drop and the rotation of the wind. The TKE and its component minimum coincides with the wind speed minimum that is reached just before the transition at both tower even on IOP6. However at WS2 there is a small increase around local sunrise, during the

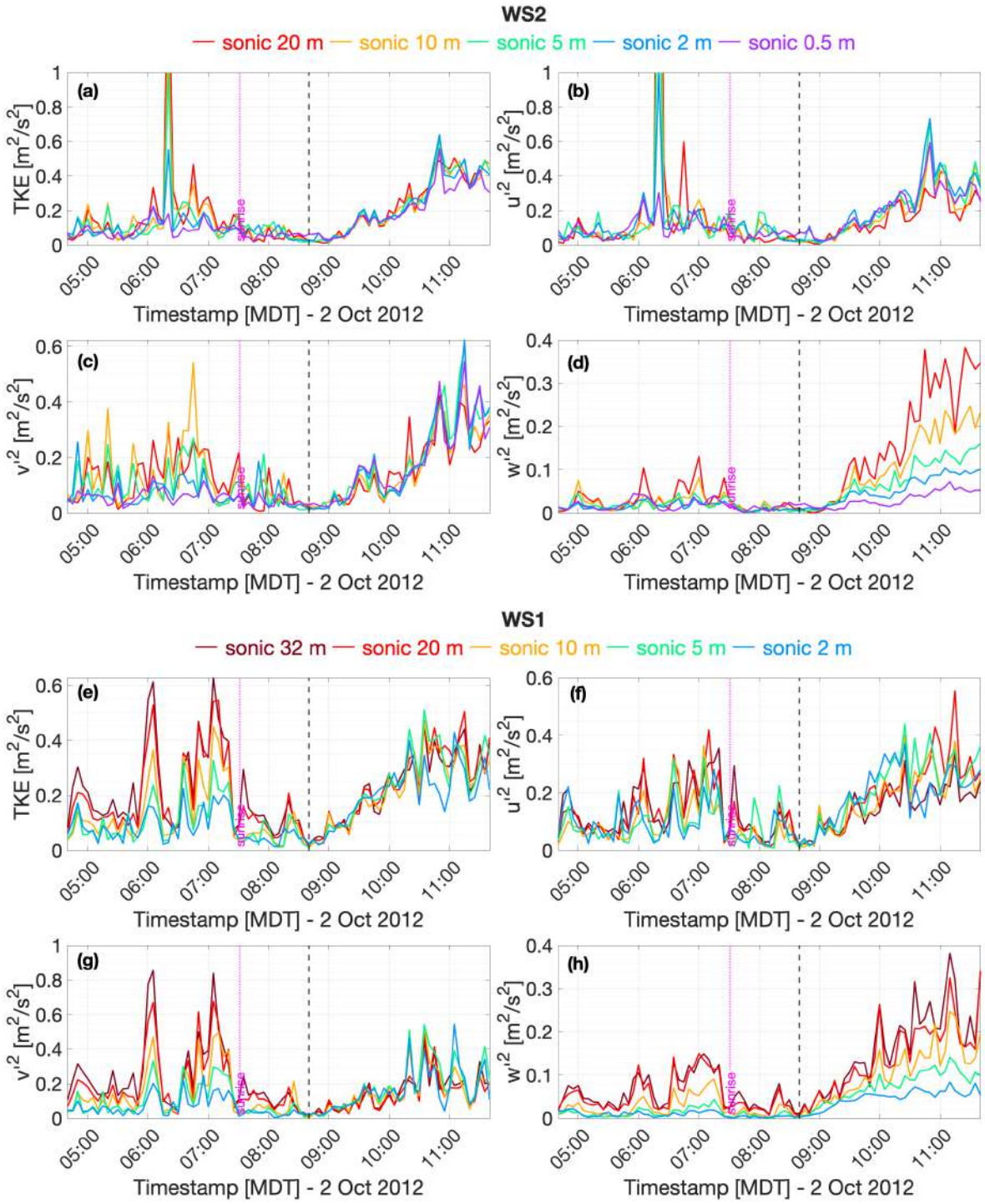

Figure 4.24: *Turbulent kinetic energy and its streamwise, spanwise and slope-normal components at WS2 ((a), (b), (c), (d)) and at WS1 (e), (f), (g), (h)) on IOP2*

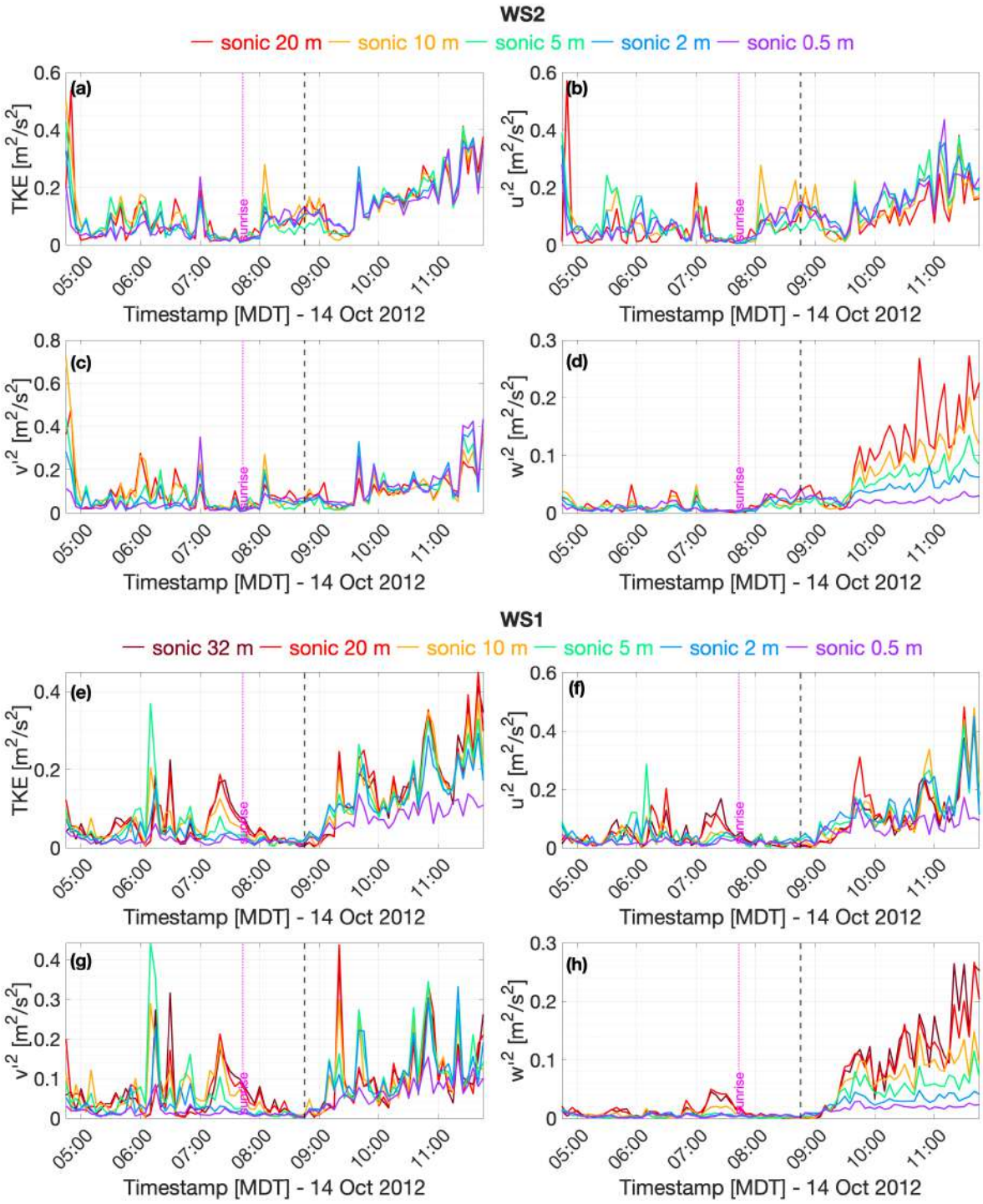

Figure 4.25: *Turbulent kinetic energy and its streamwise, spanwise and slope-normal components at WS2 ((a), (b), (c), (d)) and at WS1 (e), (f), (g), (h)) on IOP6*

wind speed drop and the transition, especially in the streamwise and the slope-normal component. At tis moment also the temperature drops along the tower due to the arrival of cooler air from the south. we are not able to determine if this is the reason for the slight TKE increase as the same behavior is observed on this tower in the IOP2 but without the TKE increase.

To summarise, the katabatic flow regime is characterized by elongated eddies in the streamwise and spanwise directions, with a modest slope-normal TKE component. From the morning transition on, the anisotropy between both the slope-parallel components and the slope-normal component decreases as atmospheric stratification goes from stable to unstable. This is consistent with the morning transition cases reported in Nadeau et al. (2020)

4.2.2.7 Kinematic Heat Flux

In this section the variations of kinematic heat flux are analyzed in order to identify the time of their sign reversal. In fact during the night, while the kinematic heat flux $\overline{w'T'}$ is negative due to the stable stratification, when the stratification becomes unstable due to diurnal heating, the kinematic heat flux becomes positive. We define PSR (Period of Sign Reversal) the period during which the kinematic heat flux changes sign from 0.5 m to 20 m AGL (we consider only the moment after which the flux is no longer negative, neglecting any previous fluctuations around zero), in order to compare it,in the following section, with the Transition Length (TL) and with the Time of Surface Inversion Breakup (TSIB), that is the time at which the temperature at 0.5 m AGL exceeds that at 20 m AGL.

On IOP2 (Fig. 4.26) the PSR at WS1 at the 2 m level starts at 08:40 MDT and lasts 35 minutes. At the WS2 the PSR starts at 09:00 MDT and lasts 20 minutes.

On IOP6 (Fig. 4.27) the kinematic heat flux changes sign first at WS1 at 08:45 MDT, exactly when the transition starts, and the PSR lasts 40 minutes. The PSR onset at WS2 is at 09:00 MDT and ends after 35 minutes.

During both the IOPs, as we expect, the sign reversal proceeds along the tower levels from the lowest to the higher and propagates along the slope from the WS1 to the WS2, as the transition and the surface inversion breakup.

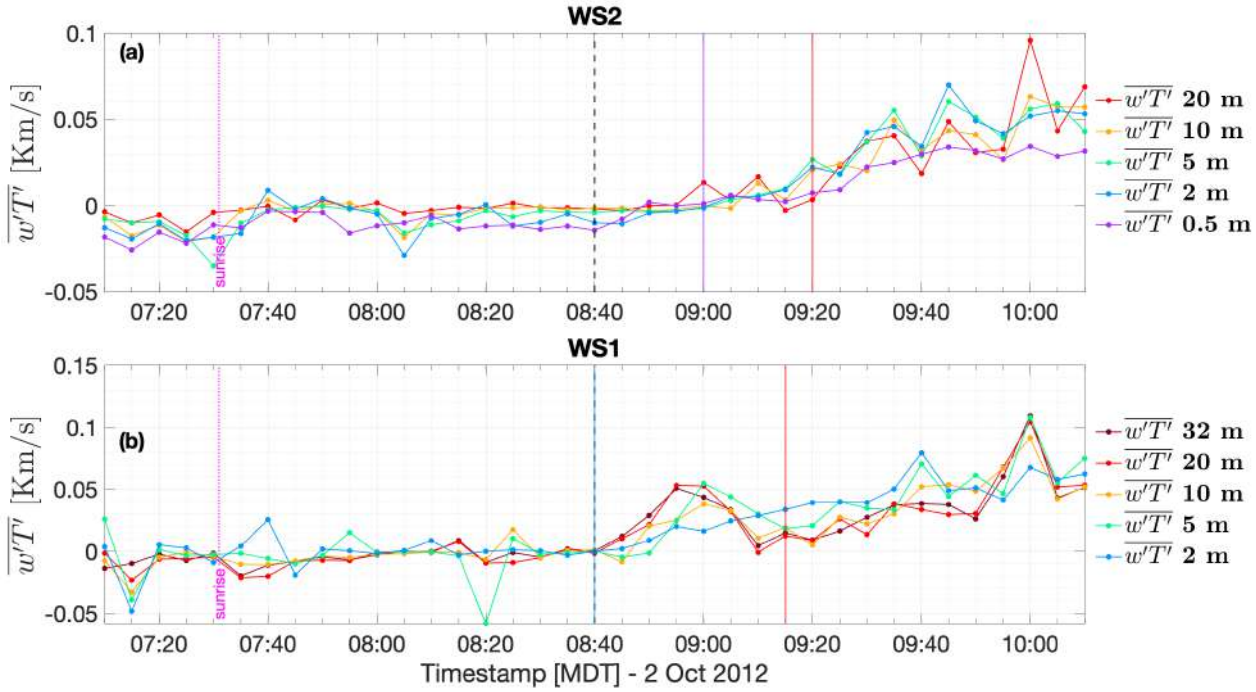

Figure 4.26: *Evolution of the kinematic heat flux around the time of local sunrise on IOP2 at (a) WS2 and (b) WS1. Black dashed line, as in all charts, identify local sunrise at WS2. Purple and red vertical lines identify the PSR at WS2 between 0.5 m and 20 m AGL. Light blue and the red vertical lines identify the PSR at WS1 between 2 m and 20 m AGL. At WS1 the kinematic heat flux at 2 m AGL change sign at local sunrise.*

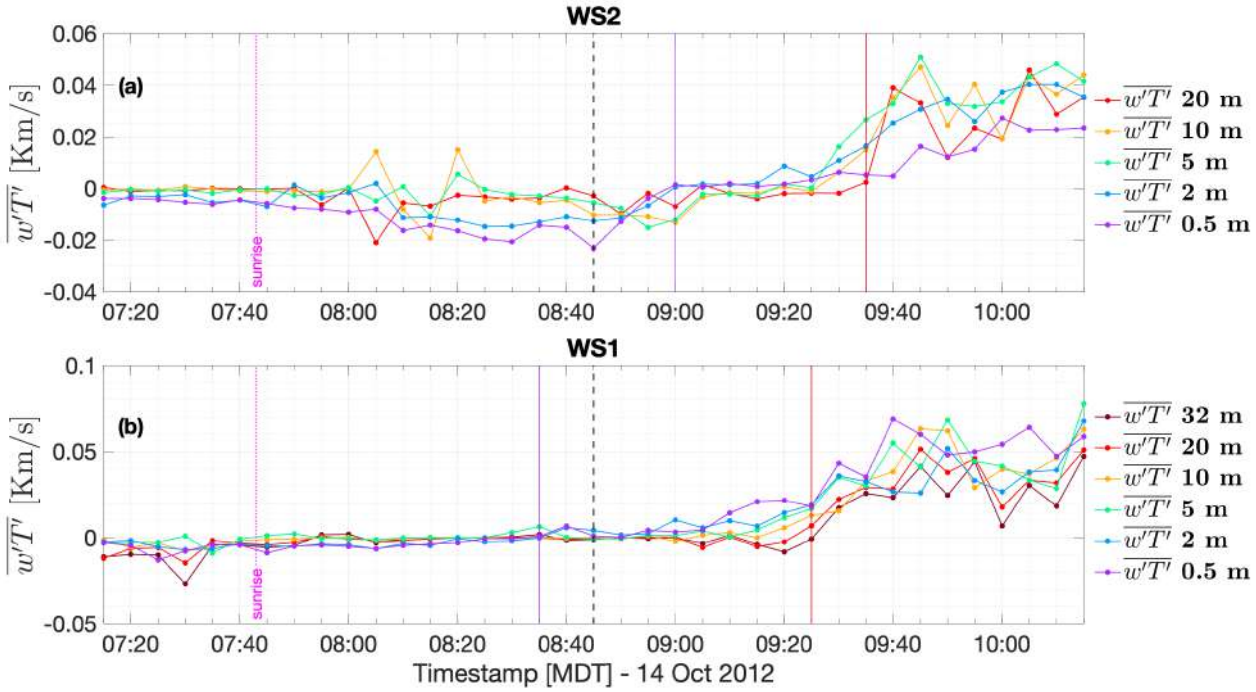

Figure 4.27: *Evolution of the kinematic heat flux around the time of local sunrise on IOP6 at (a) WS2 and (b) WS1. Black dashed line, as in all charts, identify local sunrise at WS2. Purple and red vertical lines identify the PSR at WS2 between 0.5 m and 20 m AGL. Light blue and the red vertical lines identify the PSR at WS1 between 2 m and 20 m AGL*

4.2.3 Transition Length

The characteristic parameters of the morning transition are shown in table 4.2. The transition takes place in both cases first at WS1 and then at WS2.

To summarize, on IOP2 the warming starts from the WS1 and is more efficient in the lower layers, while initially the WS2 turns out to be unaffected by the warming at all, until local sunrise. This highlights that the near-surface air heating is mainly due to surface radiation absorption that triggers the air warming starting from the less steep part of the slope. This type of warming resemble the one that occurs over flat terrain and affects also the transition onset. In fact, the transition take place starting from the lower levels at WS1. In addition, the onset of the transition at WS1 is 30 minutes before the WS2 local sunrise and at WS2 is 15 minutes after local sunrise.The PSR onset at

WS1 is at the WS2 local sunrise, 10 minutes before the transition conclusion, lasting for 20 minute after the end of the transition. At WS2, the PSR is in good agreement with the transition onset and its duration. Moreover, at WS2 the PSR and the transition end approximately at the TSIB.

IOP	TL WS1	TL WS2	WS1 TSIB	WS2 TSIB	PSR WS1	PSR WS2
IOP2 0840	40-45 min [0810]	25 min [0855]	-	0925	35 min[3] [0840]	20 min [0900]
IOP6 0845	40 min [0900]	5 min [0935]	0845	0930	50 min [0835]	35 min [0900]

Table 4.2: *Characteristic parameters of the morning transition. Local sunrise time is shown under each IOP name. TL: transition length (The onset time is reported below the length). TSIB: Time of Surface Inversion Breakup ($T_{0.5m} > T_{20m}$). PSR: Period of Sign Reversal of kinematic heath flux. For the TL and the PSR the onset time of the process are shown in square brackets. Times are in MDT.*

In contrast, on IOP6 the destruction of the surface inversion starts at both towers at the same time from above and is initially exclusively due to the mixing with the air from above, possibly for the presence of horizontal heat transfer from the heated slope. Nevertheless, while at the WS2 the thermal inversion is not consumed and the heating is almost exclusively confined at the top, at WS1, as soon as the surface heating rate exceeds the heating rate from above, the inversion is completely eroded at the time of local sunset at WS2. The different heating development between the two IOPs is possibly due to the different soil moisture content (and different relative humidity of the air), which is higher on IOP6 and leads to higher albedo, causing a less efficient absorption of the solar radiation and a slower ground warming. The main difference with respect to the IOP2 is that the transition onset at both tower is delayed with respect to the time of local sunset, especially at WS1, and that the transition at WS2 lasts only 5 minutes. The transition at WS1 starts 15 minutes after local sunrise, and at WS2 35 minutes after local sunrise. In addition, the PSR onset with respect to the transition onset is anticipated at

[3]In this case the PSR is estimated using the 2 m AGL time of kinematic heat flux reversal sign due to a lack of data at 0.5m AGL at WS1 on IOP2

WS1 and delayed at WS2, if compared with IOP2. In fact, the PSR onset at WS1 is 25 minutes before the transition onset. The PSR lasts for 50 minutes and ends 15 minutes before the transition conclusion. The transition at WS2 does not take place at the onset of the PSR. This difference could be attributed to the activation of the strong downslope flow which delay the transition until 09:35 MDT and makes it happen in only 5 minutes. However, the time of the transition conclusion is in good agreement with the PSR end and with the TISB, as in IOP2.

4.3 Characterization of the Evening Transition

The description of the evening transition on the west slope focuses on the variation between the diurnal and nocturnal regime that occurs during the IOP6 (2012 fall campaign) and the IOP4 (2013 spring campaign). In the case of IOP6, the evening transition corresponds to the evening of the day whose morning transition was analyzed in the previous section. The description proceeds chronologically in the same way and using the same near-surface variables as the morning transition. Starting as always from the evolution of radiation (Section 4.3.1), which we have already seen to be of crucial importance in the morning transition and it is supposed to be the same in the evening, the description continues with the analysis of the near-surface variables and their time evolution (Sections 4.3.2), with the TKE and kinematic heat flux variations analyses (Sections 4.3.2.4 and 4.3.2.5) and with a final summary of the main characteristics of the evening transition (Section 4.3.3).

4.3.1 Evolution of solar radiation at sunset

The evening transition on the west slope, contrary to what is observed on the east slope or in a narrow alpine-like valley, is not characterized by the movement of a shadow front and therefore the radiation does not undergo sudden drops. In the east slope case the cooling rate is initially much more efficient on the steepest slope (where the shadow comes first) than at the foot. The absence of topography to the west of the Granite Mountain determines nevertheless a gradual and progressive decrease of the shortwave solar radiation. However the progressive radiation decrease due to the sun fading is faster over the valley and on the less inclined area of the slope than on the steepest part, on which solar radiation persist up to astronomical sunset. Nevertheless, as it was during the morning transition, some section of the steeps part go in the shade far before the astronomical sunset, due to the specific topographic configuration.

Figure 4.28 shows the variations of the net shortwave radiation K (i.e., the sum of upwelling K $\uparrow$ and downwelling K $\downarrow$ shortwave radiation), of the net longwave radiation I (i.e., I = I $\uparrow$ + I $\downarrow$) and of the total net radiation R (i.e., $R = K + I$) during the IOP4. The time at which the shortwave solar radiation becomes negative is reported, identifying

the local sunset on WS2, which takes place only 10 minutes before the astronomical sunset (i.e., at 20:39 MDT) due to the absence of the shadow front. For this reason, the local sunset time is quite reasonable for the WS1 too, thus it will be shown on every charts.

It should be noted that during the IOP4 the fluctuations visible in the figure (4.28) suggest the presence of cloud cover during the day. In contrast, the IOP6 the radiation (not shown) shows the classical clear-sky pattern, with a slow and progressive decline of the radiation up to the local sunset.

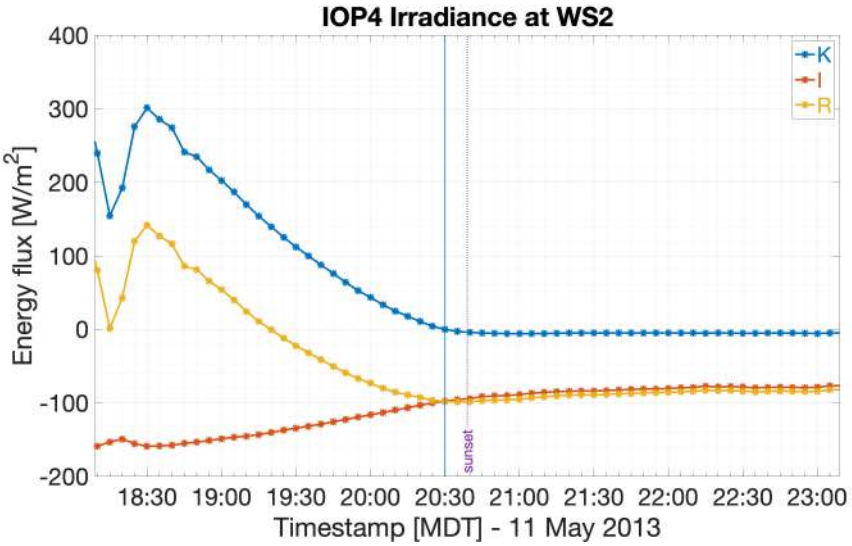

Figure 4.28: *Evolution of radiation during the evening transition on IOP4. K, I and R refers to the WS2 and are the net shortwave, the net longwave and the total net radiation respectively.The black solid line is at 20:30 when downwelling solar radiation K change sign, in accordance to the astronomical sunset (20:39 MDT) identified by the purple dashed line. the radiation fluctuation (observed also in the hours preceding those shown in the figure) indicate the presence of cloud cover during the IOP4.*

4.3.2 Near-surface variables analysis

The description of the evening transition starts from the analysis of the temperature, humidity and wind time series (Fig. 4.29 and 4.30). In this case we choose an 11-hour data segment to observe all the physical processes in the near-surface layer that precede and follow the evening transition. This interval begins in the early afternoon, 4 hours

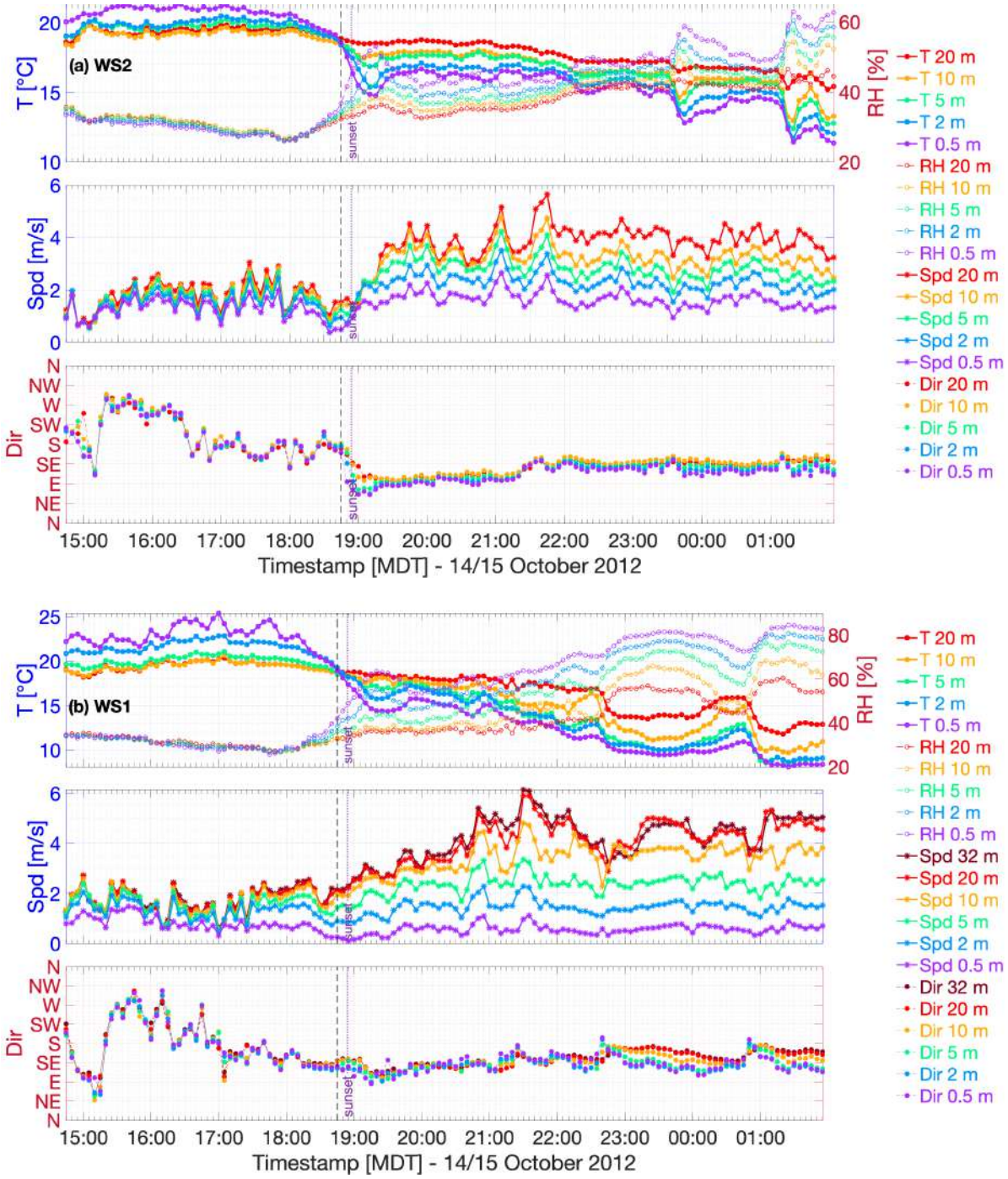

Figure 4.29: *Time series of T, RH, wind speed and direction at (a) WS2 and (b) WS1 on IOP6. The black dashed line identifies the local sunset (18:45 MDT)*

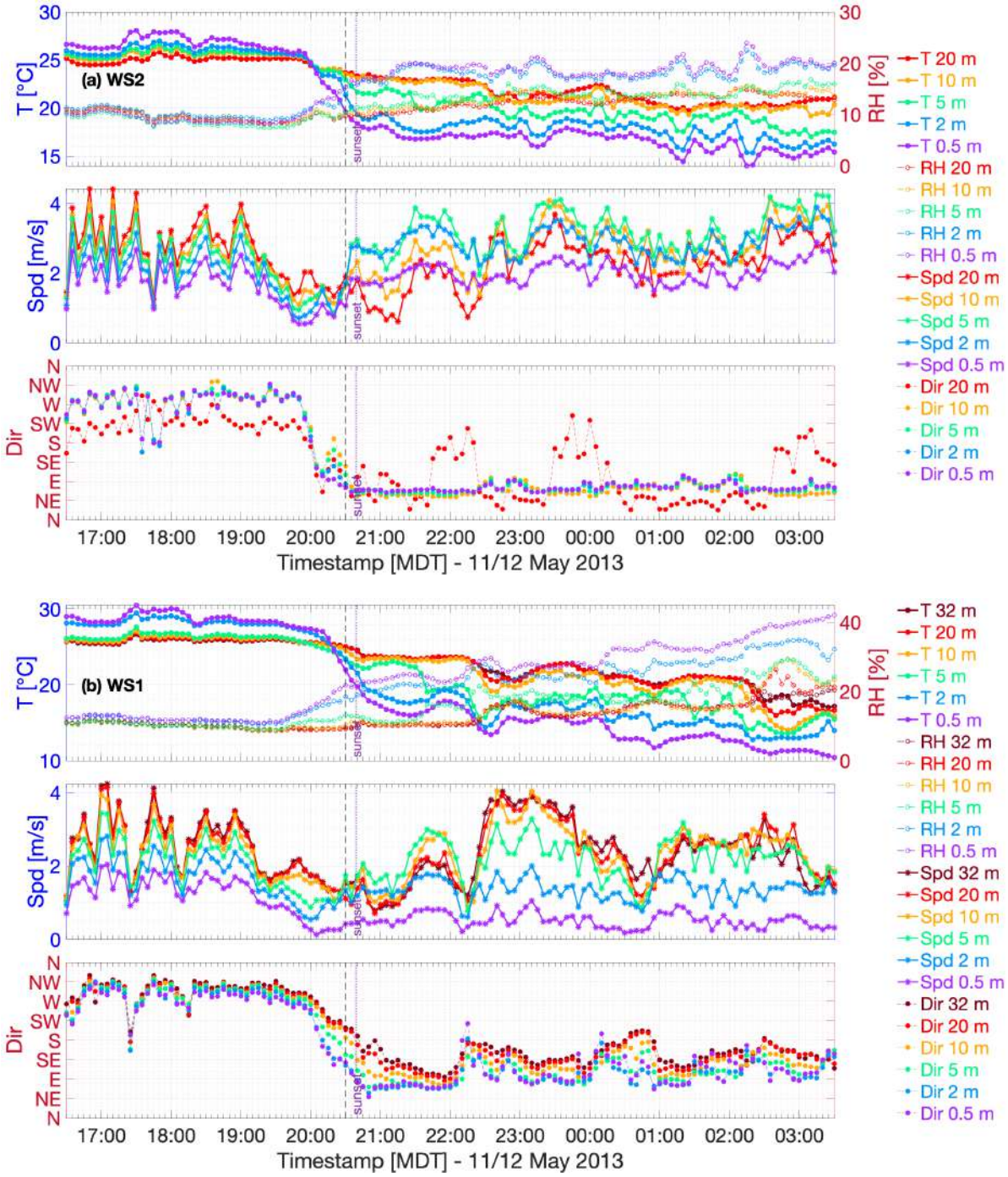

Figure 4.30: *Time series of T, RH, wind speed and direction at (a) WS2 and (b) WS1 on IOP4. The black dashed line identifies the local sunrise (20:30 MDT)*

before the local sunset, when the convective boundary layer is well developed and the daytime flow regime is already established, and ends about 7 hours after the local sunset, when the nocturnal flow and temperature inversion are both present. The description and the analysis proceeds chronologically through 3 subintervals. The beginning of the first subinterval coincides with the beginning of the 11-hours data segment, and describes the decay of the afternoon CBL, ending just before the onset of the temperature inversion. The second subinterval includes the onset of the katabatic flow and lasts until the transition is over at both towers. The last subinterval spans from the end of the transition to the end of the 11-hour data segment, describing features of the nocturnal boundary layer.

4.3.2.1 Period 1 - Afternoon CBL decay

We decide to begin with de description of the WS1 first because the sectioning of the 11-hour data segment in subinterval is also in this case based on the variations of the variables at WS2

Period 1 on IOP6 spans from 14:45 MDT to 18:45 MDT. At WS2 (Fig. 4.31) the wind direction is highly variable. During the early evening of the IOP6 upslope or up-valley wind are almost absent, contrary to what we would expect. In fact, during the afternoon the insolation has already been present for several hours and the air warming has reached its maximum. Thus the afternoon of a sunny day with low synoptic forcing is the time of the day during which the upslope becomes an up-valley (Zardi and Whiteman (2013) and De Wekker and Kossmann (2015)). A westerly wind, which is a middle way between upslope and up-valley, is visible only between 15:20-16:25 MDT. Despite the difficulty in identifying the onset of the transition due to the wind direction fluctuation, we decide to take the transition onset at 16:30 MDT, that is the first one moment after which the wind is no more from an upslope direction. The absence of a persistent upslope and/or up-valley during the afternoon and before the evening transition is a relevant characteristic of the IOP6 only. On the contrary, during the afternoon and the early evening of the IOP2 and of the spring IOPs (IOP4 and IOP7), the northwesterly up-valley is present and persistent. Moreover, in the case of IOP6, the wind speed reaches maximum values (below 3 m/s) which are the lowest among all IOPs, confirming that in this case

the evening surface flow is weak and can possibly present variable direction. This weak near-surface flow is not associated with an absence or a decrease in the solar irradiance. In fact, the radiation patter (not shown) suggests the absence of clouds during both fall IOPs and their presence only during the spring IOPs, and thus the different wind direction behavior during the early afternoon of the IOP6 may depend neither on seasonal variation of solar radiation nor on clouds presence, but it is a specific characteristics of the IOP6 only. The wind speed shear (i.e., increasing wind speed with increasing height, typical of the CBL) is also weak, with a difference of at most 1 m/s between 0.5 m and

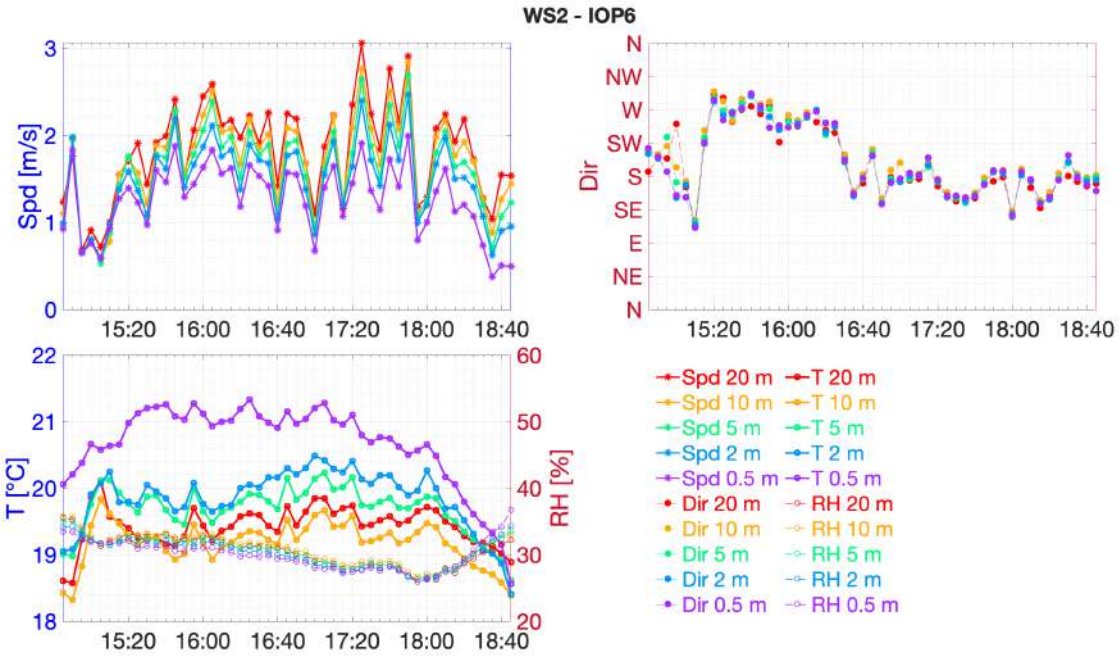

Figure 4.31: *Time series zoom on 14 October 2012 at WS2 during the Period 1. Times are in local time (MDT)*

20 m AGL. After 16:25 MDT the wind direction oscillates from the south-southeast, possibly due to the presence of a surface pressure gradient near the west slope. Potential temperature profiles in figures 4.32 show an unstable stratification under 10 m AGL with a statically stable profile between 10 m and 20 m AGL. This also suggests the absence of a strong convective structure which is instead characterized by the presence of a well mixed layer (i.e. neutral stratification) above the near-the-ground unstable profile (that is the usual potential temperature profile in the slope surface layer in the

late morning/early evening, according to De Wekker and Kossmann (2015)) and and this can further confirm the absence of a well developed diurnal near-surface flow. After approximately 15:30 MDT, potential temperature start to decrease near the ground and at 18:30 MDT the 0.5 m AGL potential temperature already drops below the 20 m AGL one and the temperature inversion begins. The surface inversion onset (that is when the 0.5 m AGL temperature drops below the 20 m AGL temperature), according to thermohygrometer data, is at 18:45 MDT and this is the time that will be reported in the summary table at the end of the evening transition analysis (4.3).

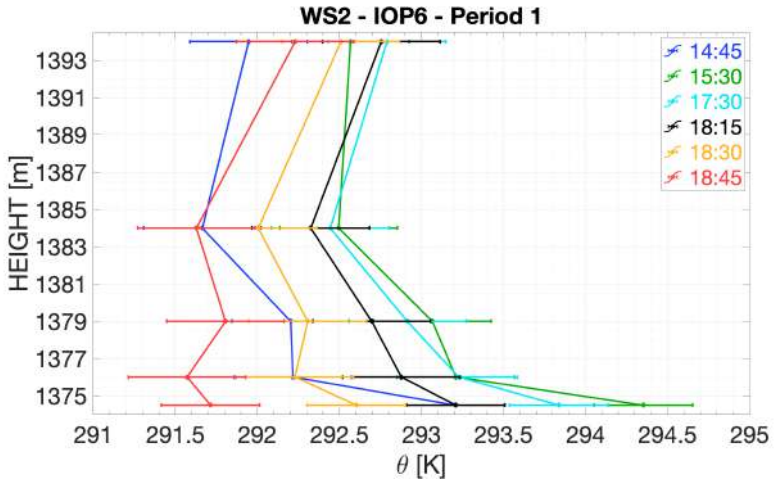

Figure 4.32: *Vertical profile of potential temperature on IOP6 at WS2 during the Period 1. Times are in local time (MDT)*

At WS1 the wind direction is even more variable than at WS2 (Fig. 4.33) showing a northeasterly wind between 15:10-15:20 MDT and then a westerly-northwesterly wind (that is an upslope/up-valley) between 15:30-16:10 MDT only for a few moments. From 16:10 MDT on the wind begins to rotate progressively from the northwest to the southeast with several fluctuations. At 16:50 the wind is from an upslope westerly direction for the last time, so we decide to take this instant to be the onset of the transition. The wind speed highest values are slightly lower than those at WS2 and every time the wind direction changes, the wind speed only drops instantaneously. The gradual rotation of the wind is not accompanied by a wind speed decrease. At WS1 the humidity is slightly higher and temperatures are on average higher of about 4 K than those at WS2 (Fig. 4.34) due to the WS1 position farther down the slope. The potential temperature shows

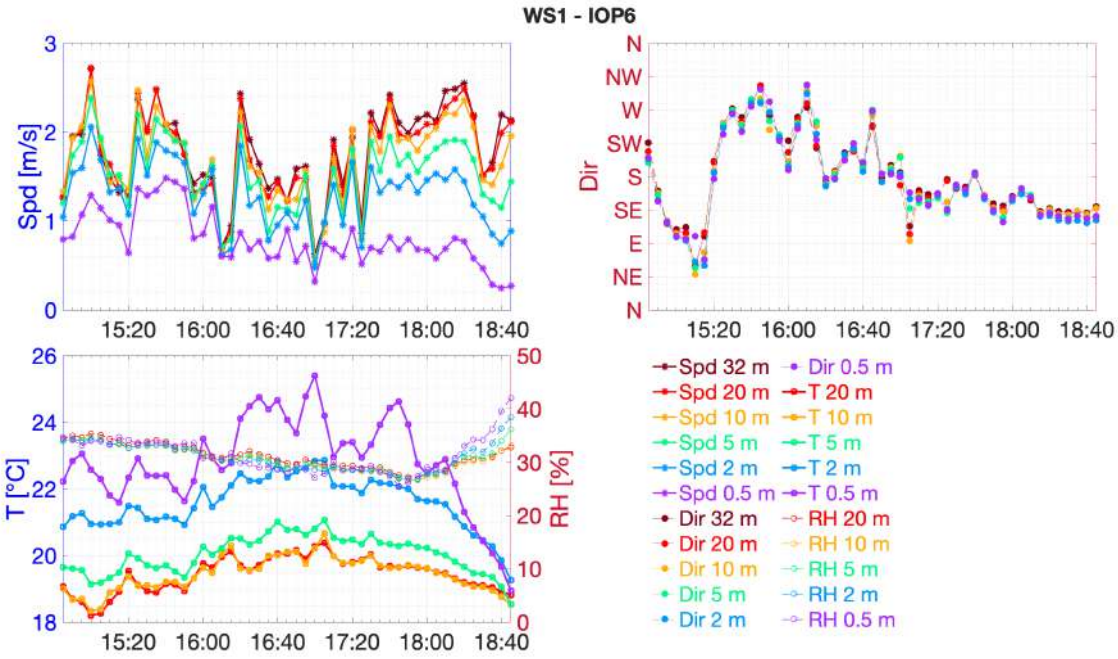

Figure 4.33: *Time series zoom on 14 October 2012 at WS1 during the Period 1. Times are in local time (MDT)*

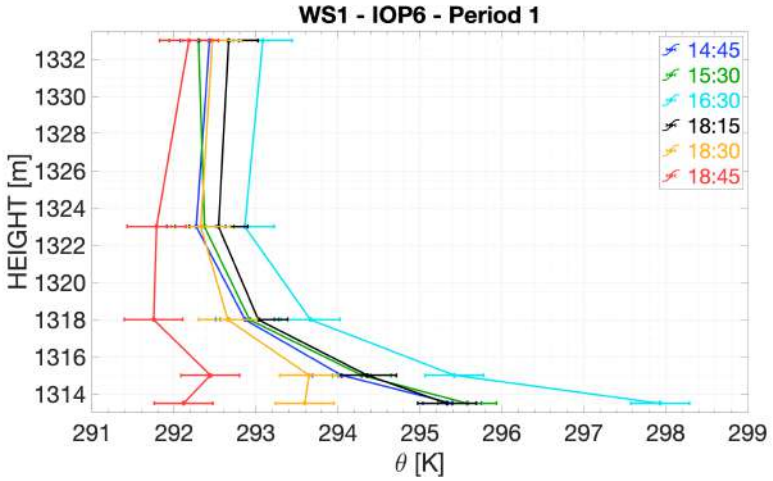

Figure 4.34: *Vertical profile of potential temperature on IOP6 at WS1 during the Period 1. Times are in local time (MDT)*

a progressive cooling approaching the sunset time. The unstable stratification is found only below 10 m AGL also in this case, while above the profile is slightly stable or almost neutral. The absence of well-mixed potential temperature profiles in the valley

atmosphere has been attributed to heat transfer from the valley sidewall surfaces to the valley atmosphere (De Wekker and Kossmann, 2015). This heating process was exactly the one mentioned in 4.2.2, according to what has been observed during the morning transition on IOP6. This also explains the potential temperature profile at WS2 (in figure 4.32 that is similar to the WS1 one) and confirms the hypothesis that the heating process during the morning transition on IOP6 is not driven by surface heating. In the specific case of IOP6, this involves the development of a weak near surface flow and a weak and intermittent upslope and up-valley, as stated earlier. At 18:30 cooling near the ground is already present, below 2 m AGL, and at 18:45 MDT the 0.5m AGL potential temperature drops below the 20 m AGL one (The onset of the surface inversion, according to the thermohygrometer data, is at 18:50 MDT, during Period 2). At that time the stratification is stable between 0.5 m and 2 m AGL and between 5 m and 20 m AGL, while the unstable stratification persists between 2 m and 5 m AGL.

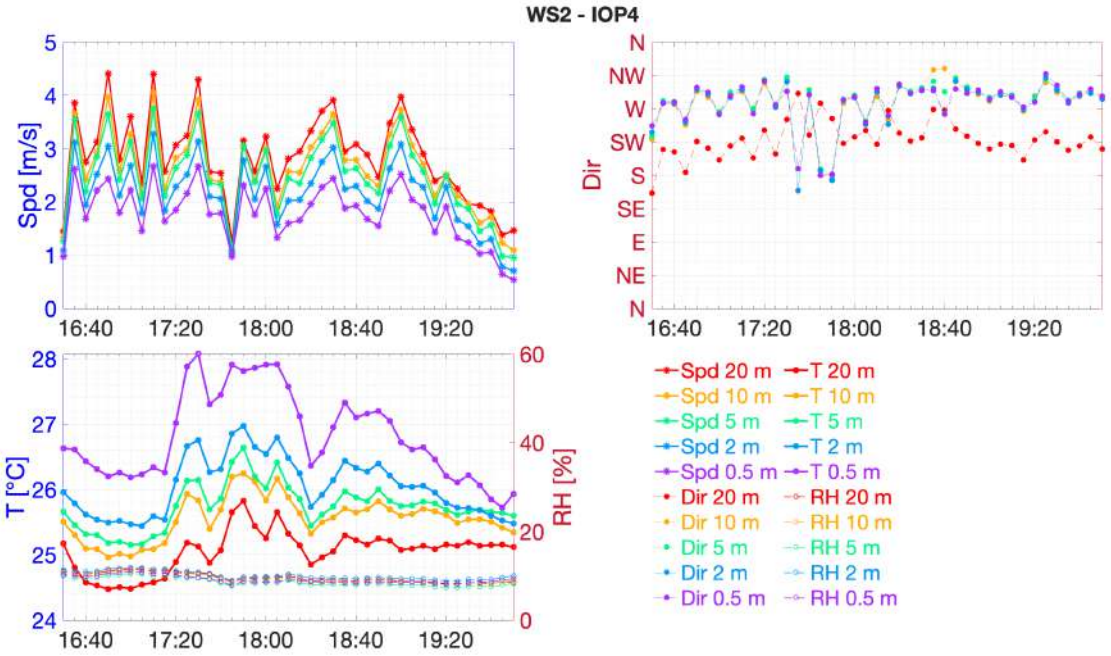

Figure 4.35: *Time series zoom on 11 May 2013 at WS2 during the Period 1. Times are in local time (MDT)*

Period 1 on IOP4 spans from 16:30 to 19:50 MDT. The diurnal near surface wind are well developed on IOP4, contrary to IOP6. The wind speed at WS2 is larger than

that on IOP6 and so is the wind speed shear (Fig. 4.35). In fact, differences of about 2 m/s are reached between the near-surface level wind speed and the 20 m AGL level. The wind direction initially oscillates around the west (upslope) with a slight and progressive rotation to the northwest (up-valley) except for the 20 m AGL level. In fact the direction at 20 m oscillates from the south and rotates slightly to the southwest, still oscillating slightly. The different direction of the wind between this and the lower levels (including those at WS1 where there are no differences in wind direction between the levels), may be due to the presence of an ambient or background wind above the surface layer, but the absence of data above the 20 m AGL cannot confirm this hypothesis. The wind speed shows the same oscillations along all levels excluding that there is a malfunctioning of the sonic at 20 m. At the end of Period 1, approaching sunset, the wind speed starts to decrease but no wind direction variation are shown. The relative humidity is lower than that during the night, in accordance with the presence of high temperatures due to the insolation. In figure 4.36 the potential temperature profiles are unstable along the whole tower and in particular near the ground, emphasizing that in this case warming rises from of the ground. The cooling starts after 18:00 MDT in the lower layers and at 19:50 MDT there is already a hint of stable stratification between 2 m and 5 m AGL.

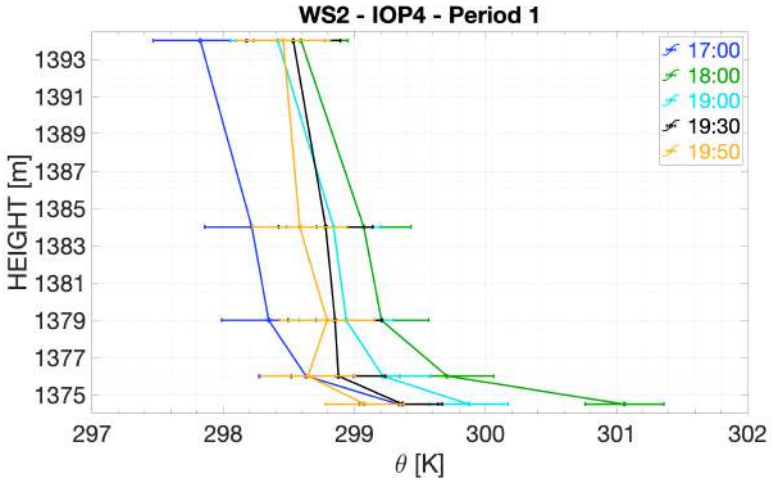

Figure 4.36: *Vertical profile of potential temperature on IOP4 at WS2 during the Period 1. Times are in local time (MDT)*

At WS1 on IOP4 (Fig. 4.37) the wind speed shear is even stronger than that at WS2. The temperature shows a strong difference between the levels below 2 m AGL,

very warm, and those above that certainly confirms the presence of a very well developed CBL in the lower layers. Nevertheless the wind direction is more variable than that at WS2 showing a northwesterly up-valley wind which turns southwesterly-southerly in some moments, during which a slight temperature decreases takes place. This behavior may depend on the formation of a pressure gradient near the flattest area of the west slope. The shear in wind direction is visible throughout the entire Period 1, with the wind in the higher levels slightly clockwise rotated with respect to the lower ones. Wind direction shear increases approaching sunset times (i.e., 20:39 MDT), together with a slight speed decrease. Potential temperature profiles in figure 4.38 confirm the presence of the unstable stratification below 5 m, which becomes almost neutral above 10 m AGL

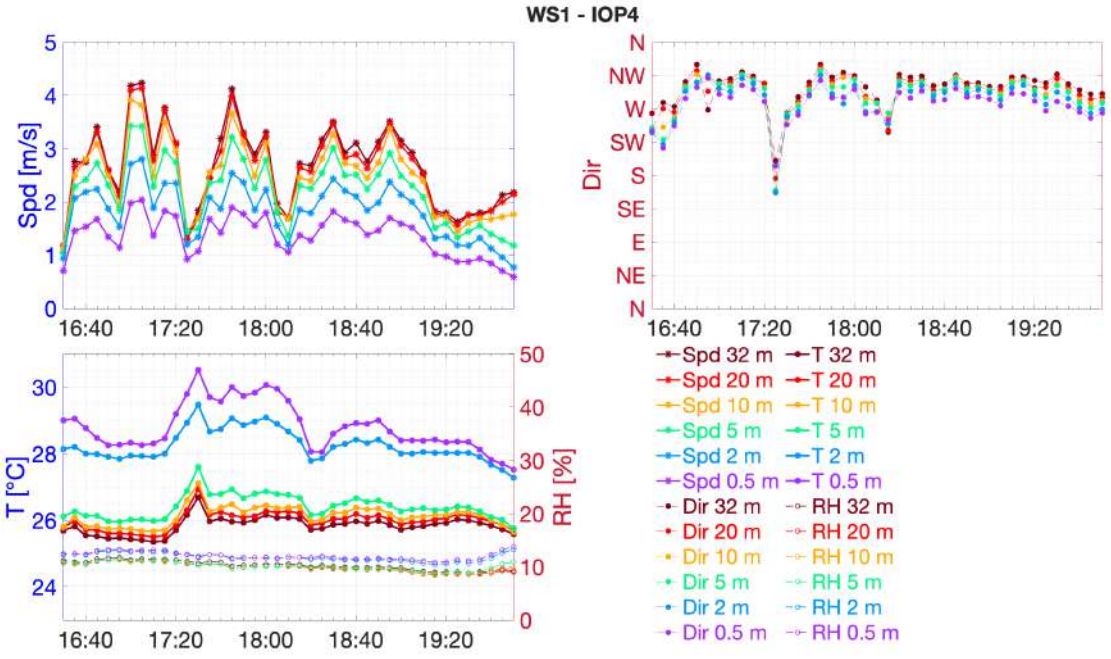

Figure 4.37: *Time series zoom on 11 May 2013 at WS1 during the Period 1. Times are in local time (MDT)*

(i.e., a well-mixed layer above the unstable one, showing the predominance of surface heating, typical of the valley CBL (De Wekker and Kossmann, 2015)) explaining the presence of wind direction shear. After 18:00 MDT the cooling begins in all levels, especially near the surface, and at 19:50 MDT neutral stratification starts to become stable between 10 m and 20 m AGL.

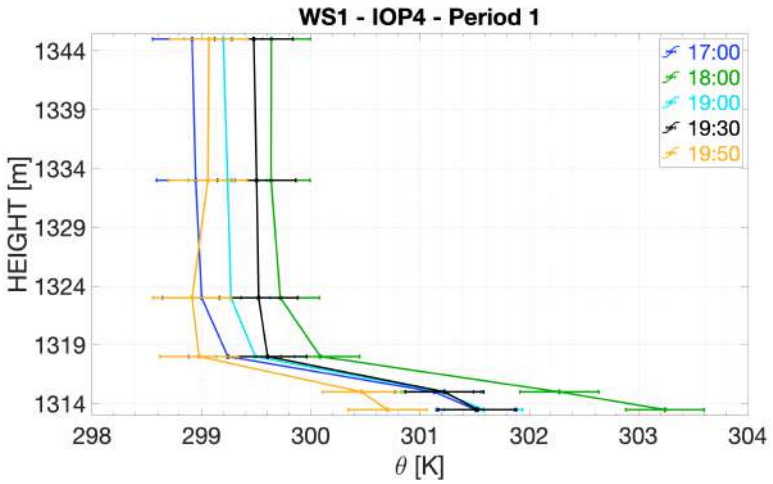

Figure 4.38: *Vertical profile of potential temperature on IOP4 at WS1 during the Period 1. Thermohygrometer data are available even at 32 m AGL. Times are in local time (MDT)*

4.3.2.2 Period 2 - The strengthening of the thermal inversion and the downslope onset

Period 2 on IOP6 spans from 18:45 (i.e., local sunset) to 19:20 MDT and is identified by solid black vertical lines in figure 4.39 and 4.41. Since this time interval is very short, the figures will show a wider time interval to better illustrates the variable variations. At WS2 the wind speed dropped below 2 m/s at the end of Period 1 and the progressive rotation of the wind direction has already made the wind blowing from the south. As the wind speed reaches the minimum value below 1 m/s at 18:30 MDT, the wind speed increases mainly at 2 m and 5 m AGL, where it rises of about 1 m/s between 18:50-19:00 MDT. The downslope is activated exactly during this time interval, when, starting at 0.5 m AGL up, the wind shifts towards the easterly flow. Below 5 m AGL the wind shift towards the northeast firstly and then, at the end of Period 2, towards the east. Above 5 m AGL the wind shift from the south towards the easterly downslope without passing from the northeast. At 19:20 MDT the transition is concluded. Thus the so-called "evening calm period", that is the "morning calm period" counterpart, that takes place on the east slope before the transition usually with a speed under 1 m/s lasting even tens of minutes (Jensen et al. (2017) and Lehner et al. (2015)), does not occur (except for the

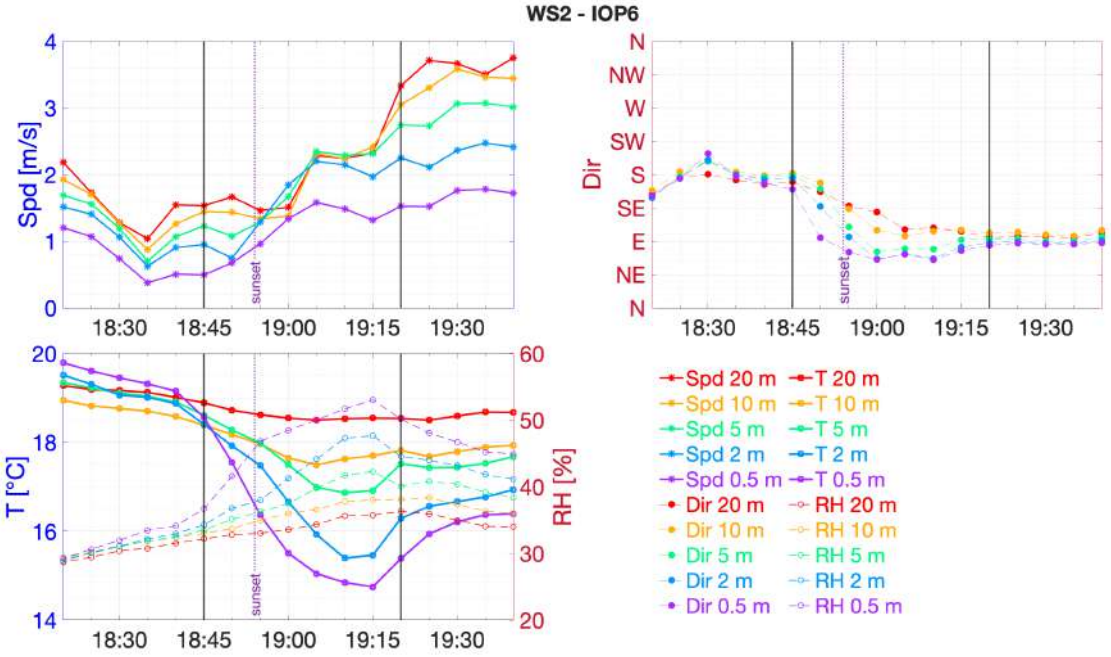

Figure 4.39: *Time series zoom on 14 October 2012 at WS2 during the Period 2. Times are in local time (MDT)*

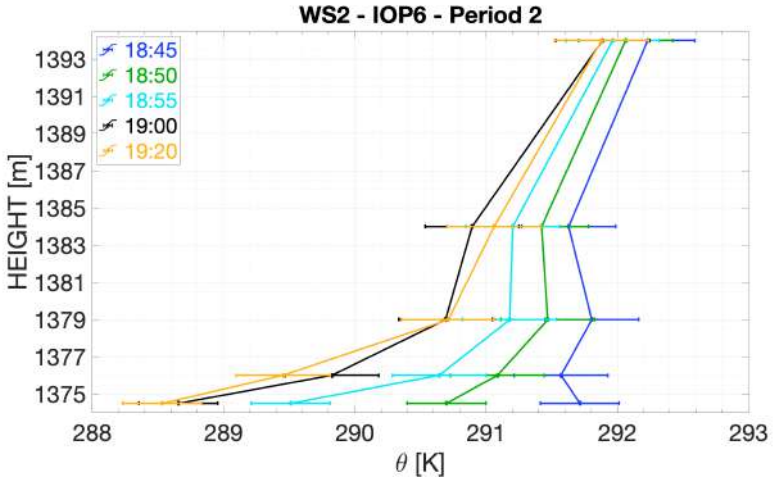

Figure 4.40: *Vertical profile of potential temperature on IOP6 at WS2 during the Period 2. Times are in local time (MDT)*

speed minimum at 18:35 MDT which is almost instantaneous). This may depend on the absence of distinct wind transition, due to both the absence of a strong convective structure and to the absence oh the shadow front, if compared with the east slope. The

activation of the downslope below 5 m AGL is accompanied by a significant decrease in the air temperature, contrary to what usually happen during the night, when the downslope is accompanied by a warm advection that rises the temperature due to mixing with the warm air from the upper part of the slope (Papadopoulos and Helmis, 1999) and due to compressional warming during the flow descent (Fleagle, 1950), as seen in section 4.2.2.1 before the morning transition. The fact that the cooling below 10 m AGL is due to the downslope and not exclusively to the decrease in SW radiation that has already become negative, is confirmed by the fact that the sudden drop in temperature is followed by an increase. The temperature drop and the increase in wind speed coincides with the occurrence of a downslope acceleration with frontal characteristics at the foot of a mountain described by Papadopoulos and Helmis (1999). At 18:50 MDT the potential temperature profile is stable between 0.5 m e 5 m AGL and above 10 m AGL, with a nearly instable profile in between (Fig. 4.40). The downslope activation cools the level below 5 m AGL and mixed the layer between 5 and 10 m AGL, making it nearly neutral between 18:55-19:00 MDT and showing a thickness of about 5 m. The occurrence of a downslope acceleration with frontal characteristics at the foot of an east facing slope is described by Papadopoulos and Helmis (1999), who argue that downslope flow originates in a very high and cool area where the shadow already take place. This could mean that even in the west slope case, some section of the steepest slope go in the shade well before the towers area.

At the beginning of Period 2 the wind direction is already from the southeast at WS1 (Fig. 4.41). The wind shifts from the southeast to east. The wind speed increases especially above 5 m AGL, having reached a minimum just before the end of Period 1, as at WS2. Above 10 m AGL the wind speed exceeds 2 m/s. The onset of surface inversion takes place at 18:50 MDT. The wind direction, initially the same in all levels, shows a weak shear. From 19:05 MDT the temperature stay almost constant above 5 m AGL, while the temperature continues to fall until 19:15 MDT below 2 m. At the same time, the wind turns east below 2 m AGL and is slightly clockwise rotated above. This differences between the levels is perhaps due to the arrival of the downslope from the WS2 below 2 m AGL. Its arrival is hidden by the presence of the southeasterly wind but can be confirmed by fact that the temperature drop below 5 m AGL is followed by an

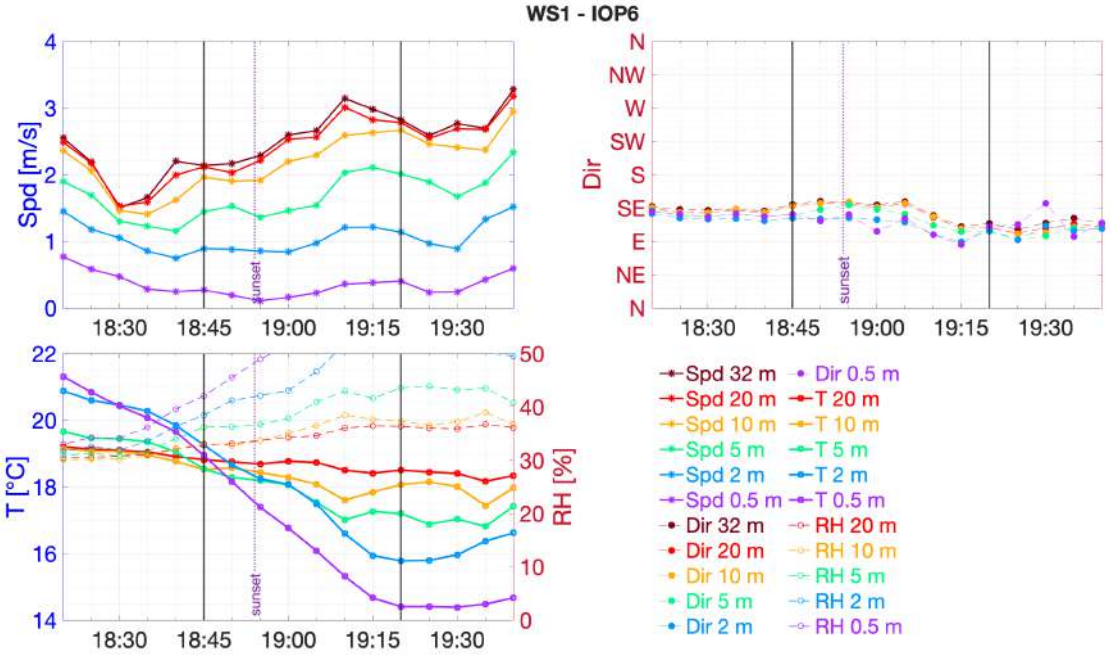

Figure 4.41: *Time series zoom on 14 October 2012 at WS1 during the Period 2. Times are in local time (MDT)*

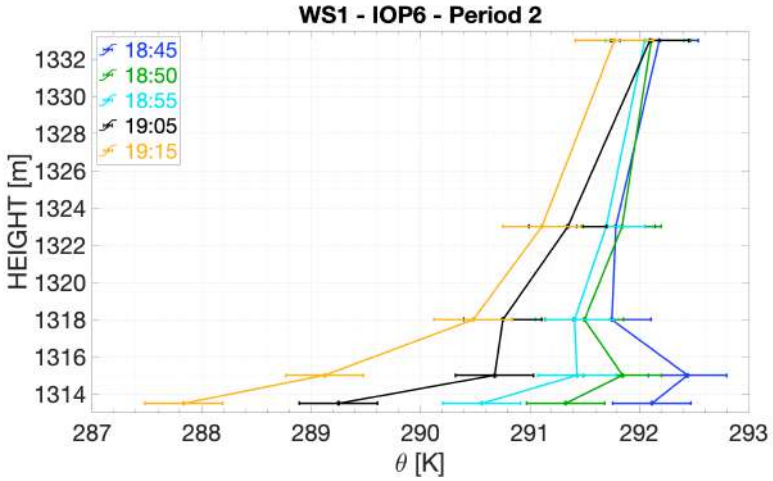

Figure 4.42: *Vertical profile of potential temperature on IOP6 at WS1 during the Period 2. Times are in local time (MDT)*

increase, as seen on the WS2 during the arrival of the downslope. In this case the downslope is confined only under 2 m AGL. The unstable stratification (Fig. 4.42) between 2 m and 5 m AGL with and almost neutral stratification above are progressively

replaced by the stable stratification induced by the arrival of the downslope. Above 10 m AGL there is almost an absence of cooling. The transition end at 19:20 when the wind is easterly/northeasterly along all the tower level. The evening calm period with speed under 1 m/s is absent also at WS1, even if there is a speed drop concentrated in the upper layer around 18:30 MDT (just before the end of Period 1) and even if the speed below 5 m AGL is practically under 2 m/s between 18:20-19:14 MDT.

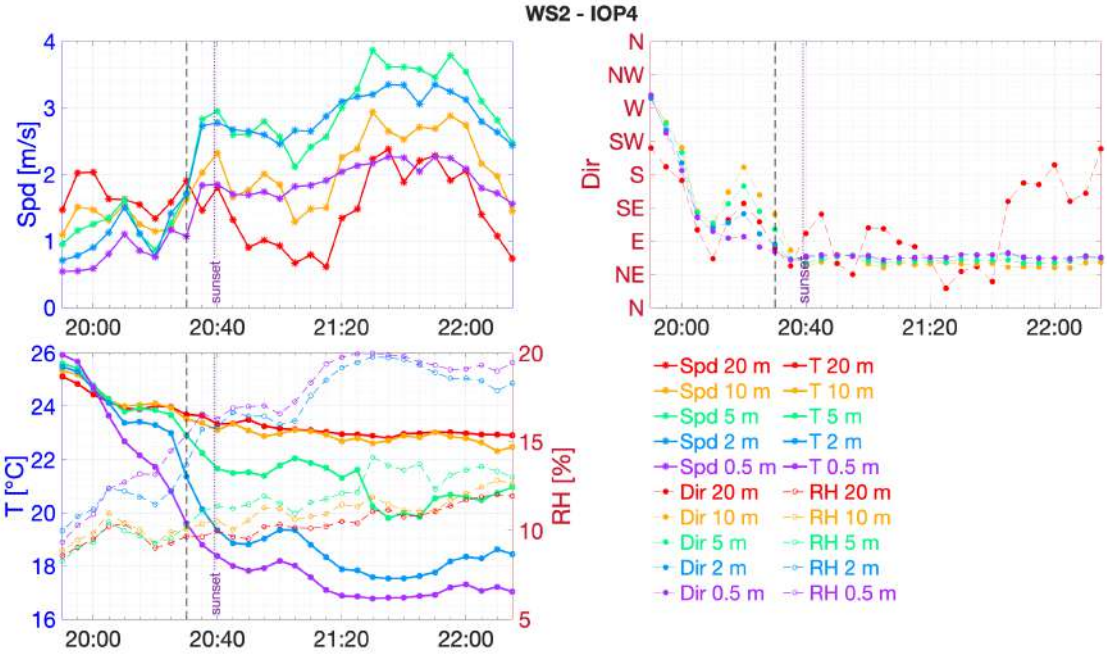

Figure 4.43: *Time series zoom on 11 May 2013 at WS2 during the Period 2. Times are in local time (MDT)*

Period 2 on IOP4 spans from 19:50 to 22:15 MDT. At WS2 (Fig. 4.43) the wind shifts counterclockwise between 19:55-20:10 MDT from the west to the east-southeast in all levels except for the 20 m AGL, where the wind rotates from southwest to northeast. During the rotation the wind speed undergoes a slight decrease with values under 2 m/s. At the same time the temperature drops slowly above 10 m and faster below, dew to surface cooling. The onset of the temperature inversion is at 20:05 MDT. Between 20:20-20:35 MDT a slight clockwise rotation of the wind from the east-southeast to the south occurs, especially at 10 m AGL (the 20 m AGL wind shifts from the northeast to southeast) during which the wind speed rises sharply below 10 m AGL, especially at 2 m

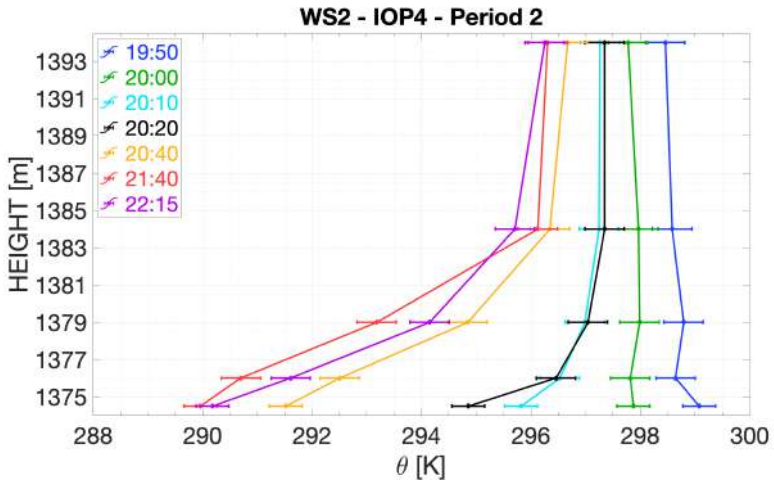

Figure 4.44: *Vertical profile of potential temperature on IOP4 at WS2 during the Period 2. Times are in local time (MDT)*

and 5 m AGL where it increases by 2 m/s in 15 minutes, highlighting the downslope activation. In fact the temperature drops sharply below 5 m AGL 5 minutes after the speed increase. At 20:35 MDT, 5 minutes after local sunset, the wind is an easterly-northeasterly downslope and the transition is over. The very low speed values at 20 m AGL, under 1 m/s, and the highly variable wind direction, which spans from the northeast to the southeast, suggests the absence of the downslope above 10 m AGL, even if the wind speed variations at 20 m are exactly the same as those at 10 m and 5 m AGL. Excluding the wind variations at 20 m, the shear in wind direction is almost absent, confirming the predominance of the downslope. At 21:15 MDT the speed increases from the 5 m AGL up but the wind direction does not undergo any significant change, except for the level at 20 meters that, from 21:45 MDT on, shows a flow that oscillates around the south. Figure 4.44 shows that the almost neutral stratification becomes progressively stable below 10 m AGL, while above this level the neutral stratification persists. At the downslope onset (20:20 MDT) the potential temperature profile is almost neutral above 5 m AGL, nearly stable between 2m and 5 m AGL and very stable near the ground. So on IOP4 the downslope front has to move through a less stable environment compared to the IOP6 case which was almost stable everywhere, and thus it develops faster and covers a deeper surface layer (Papadopoulos and Helmis, 1999). In fact, the wind speed rise associated to the downslope activation is of about 2 m/s while on IOP6 is less than

1.5 m/s. The different downslope acceleration can thus leads to a deeper downslope layer depth on IOP4, at least 10 m deep, that is the thickness of the layer below the one with a stable stratification.

The transition at WS1 begins in Period 1 (Fig. 4.37) with the decrease in wind speed and the increase in wind direction shear. in fact, at 19:30 the wind begins to rotate progressively from the westerly-northwesterly down-valley 4.45. As the wind speed keeps decreasing at all levels, at 20:05 MDT the wind speed starts to increase at 2 m and 5 m AGL. At the same time the temperature begins to decrease between 0.5 m and 5 m AGL, while initially above 5 m AGL it stays almost constant. The onset of the temperature inversion is at 20:20 MDT and at 20:30 MDT (i.e., local sunset) the wind speed at 5 m AGL exceeds that at 32 m AGL. At that time the wind is southeasterly at 05 m and 2 m AGL and, rotating clockwise along the tower, it is southwesterly at 20 m and 32 m AGL. The decrease in temperature proceeds at an high rate below 5 m AGL but then, at 20:45 the decrease ends from 5 m AGL up while the cooling continues below. The easterly downslope is activated at about 20:40 (10 minutes after local sunset) below 5 m AGL. At 20:50 MDT the wind is easterly-northeasterly below 5 m AGL, where the transition is already conclude, and southerly at 32 m AGL, always rotating clockwise going up along the tower. At the same time the speed begins to increase at all levels, especially above the 2 m AGL and with the maximum speed at 5 m AGL, highlighting a strengthening of the downslope. As the temperature decrease proceeds below 2 m AGL, a considerable temperature drop occurs at 5 m AGL while the temperature above 10 m AGL stays constant until the end of Period 2. The last part of the transition occurs while the wind speed exceeds 2 m/s from the 2 m AGL level up. Thus, we do not observe an evening calm period also in this case. At 21:55 the transition is over and at 22:00 the wind direction shows the first night fluctuation, shifting towards the south. The potential temperature profiles in the figure 4.46 show the surface cooling below 5 m AGL. The stratification becomes stable at 20:10 MDT between 5 m and 20 m AGL, topped by a neutral profile. The onset of the temperature inversion is at 20:20 MDT. At 20:40 MDT the potential temperature profile is completely stable along the whole tower. Between 20:40-21:40 MDT the cold advection associated with downslope cools the layers below 2 m AGL before and then below the 5 m AGL, showing a deepening of downslope depth.

During the same period the frontal passage associated with upward mixing makes the profile stable above 10 m AGL.

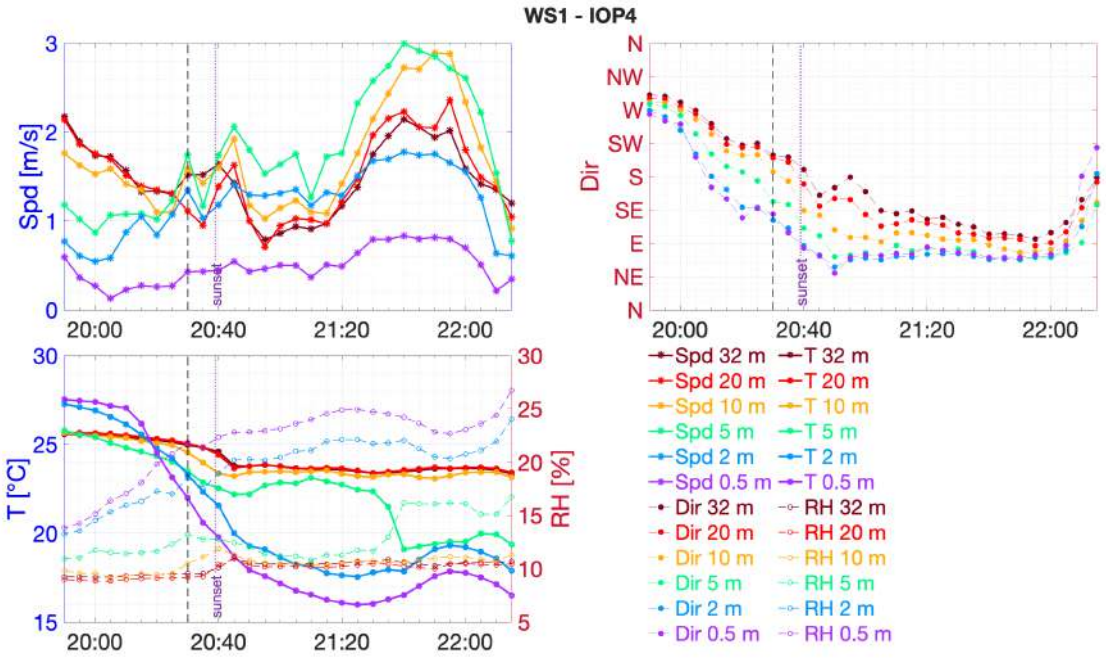

Figure 4.45: *Time series zoom on 11 May 2013 at WS2 during the Period 2. Times are in local time (MDT)*

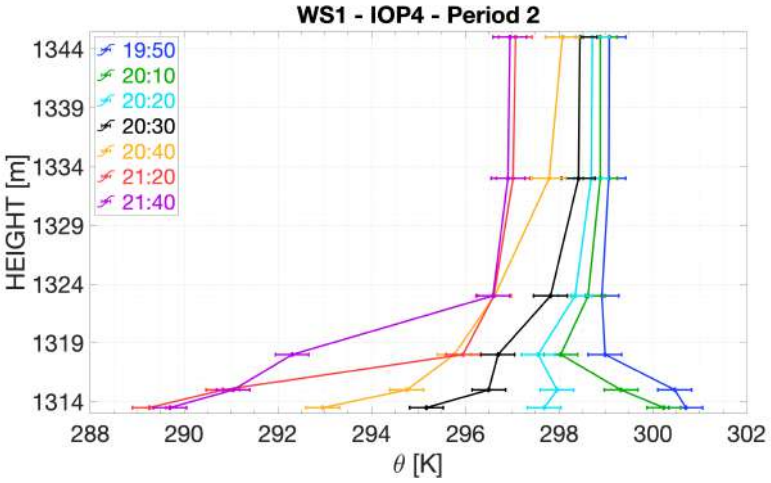

Figure 4.46: *Vertical profile of potential temperature on IOP4 at WS1 during the Period 2. Times are in local time (MDT)*

4.3.2.3 Period 3 - The nocturnal boundary layer after the evening transition

The description of the nocturnal boundary layer is performed outlining the characteristics of the time series at both towers simultaneously, as in section 4.2.2.1.

Period 3 on IOP6 spans from 19:20 MDT to the end of the 11-hour data segment, around 02:00 MDT (Fig. 4.47 and 4.48).The nocturnal boundary layer during Period 3 of IOP6 is characterized by strong wind shear in speeds, similar to a daytime situation, with maximum values reaching 6 m/s at WS1 and slightly lower values at WS2. An important feature that distinguishes the early stages the nocturnal boundary layer from that described in the section 4.2.2.1 that refers to the late night and early morning, is the decrease in temperature. Moreover, the early-night boundary layer is initially undisturbed until about 22:30 MDT. There is only a progressive wind speed increase at WS1, especially above 5 m AGL, followed by a decrease. The presence of the undisturbed nocturnal boundary layer after the evening transition is also found on the east slope (Lehner et al., 2015). During this period the wind direction shear is practically absent. The wind is easterly at WS2 and slightly clockwise rotated (i.e., easterly-southeasterly) at WS1, underlining the prevailing influence of slope flows at WS2 and of valley flows at WS1. The wind rotates progressively at both tower to the southeast throughout this period . Thus, as the air cools, the wind rotates from downslope to down-valley. At 22:40, the calm period ends. The wind rotation at WS1 occurs at the same time as the wind speed reaches a minimum, while at WS2 the wind does not undergo significant changes. Both towers, however, show a decrease in temperature. The down-valley decreases the temperature at WS1, especially in the higher levels, of about 3 ^{o} C, while at WS2 the temperature falls of about 2 ^{o} C. Therefore the valley inversion push up the slope the cold valley air, influencing more the tower on the lower part of the slope. From this moment on the influence of the down-valley produces the wind direction shear at WS1. As the wind becomes more southeasterly at WS2, temperature fluctuation becomes more frequent, with a stronger temperature drops. When the wind direction at WS1 is southeasterly, the temperature drops, but when the the tower is reached by the downslope, the temperature rise, as already seen before the morning transition.

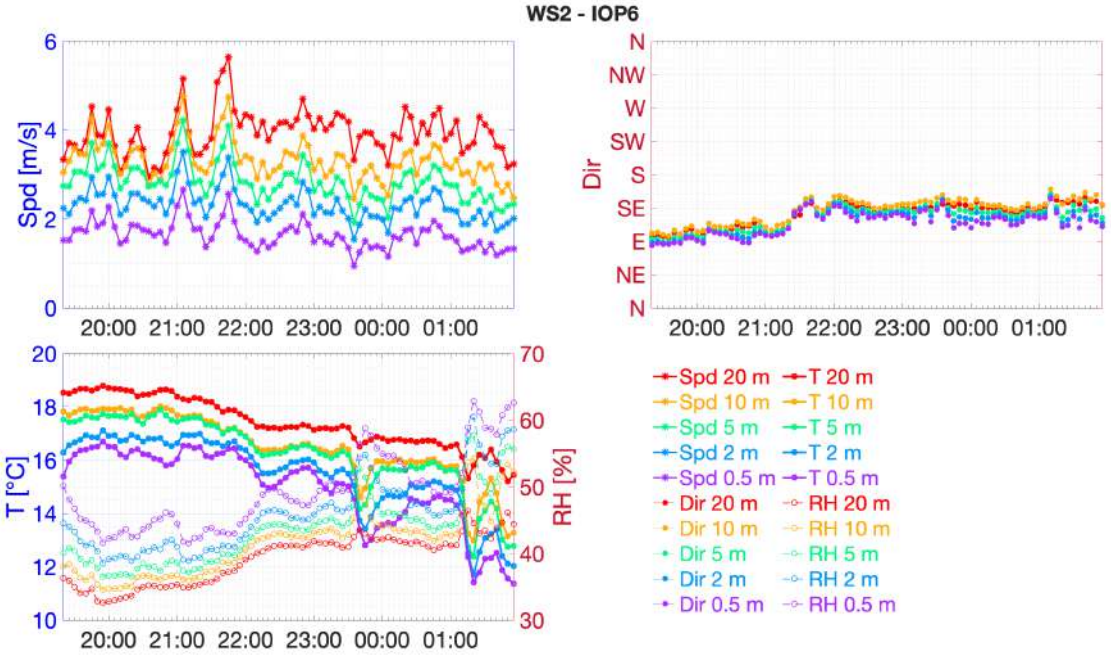

Figure 4.47: *Time series zoom on 14/15 October 2012 at WS2 during the Period 3. Times are in local time (MDT)*

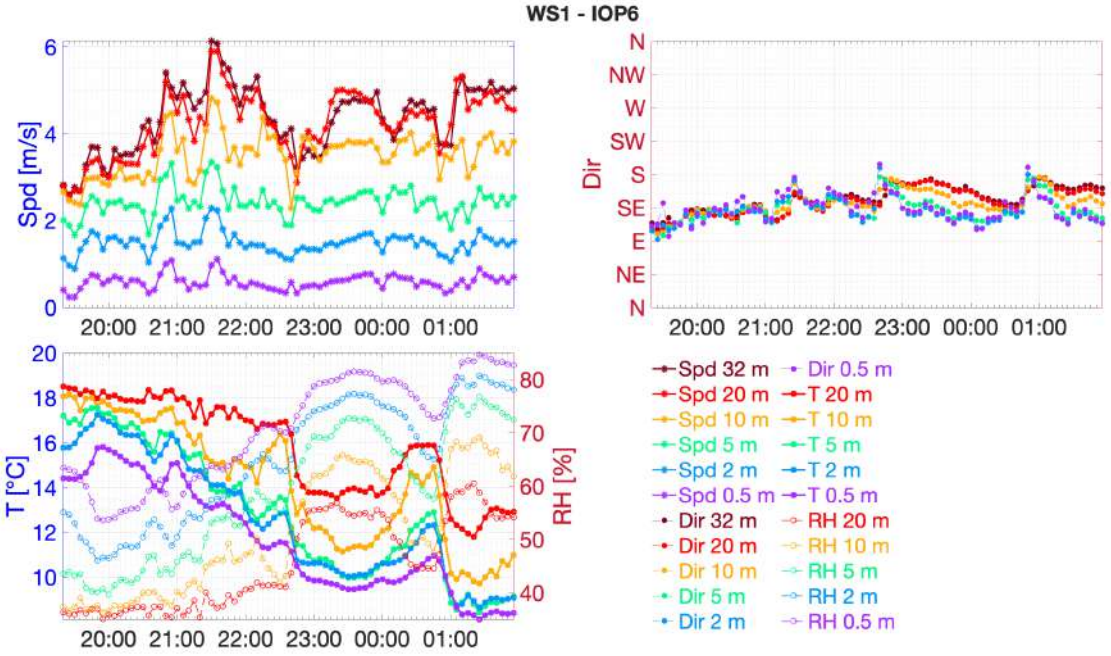

Figure 4.48: *Time series zoom on 14/15 October 2012 at WS1 during the Period 3. Times are in local time (MDT)*

Period 3 on IOP4 spans from 22:15 MDT to the end of the 11-hour data segment, around 03:30 MDT. During this period the wind shows a very different behavior at the two towers (Fig. 4.49 and 4.50). The wind direction at WS2 is almost undisturbed throughout the period, with a northeasterly downslope sometimes replaced by an easterly wind only. When the wind is from the northeast, at 20 m it rotates to the south, and when it is from the east, at 20 m it rotates to the north-northeast. The wind direction shear is almost absent. The maximum speed is at 5 m AGL and the 2 m and 10 m AGL levels show wind speeds close to the 5m level. The temperature gradually decreases with very limited fluctuations. At WS1 the wind direction has an oscillatory behavior and the shear is very strong both in direction and in speed. The average temperature gradient is about 8°C, while at WS2 only 5°C, and at this tower the temperatures are about 2°C higher than that at WS1. The temperature drops at WS1 occur when the wind rotates from south-southeast also in this case, while the temperature remains almost constant when the wind turns more from the east. The presence of such a strong wind shear at WS1, with maximum speed values reaching 4 m/s above 10 m AGL, together with a strong temperature gradient indicate the presence of a very intense valley flow. This can cause the wind direction changes at 20 m AGL at WS2 when this interacts with the down-valley flow. In fact, when the wind at 20 m AGL at WS2 comes from the northeast, the interaction with the valley flow makes it rotate from the south-southeast.

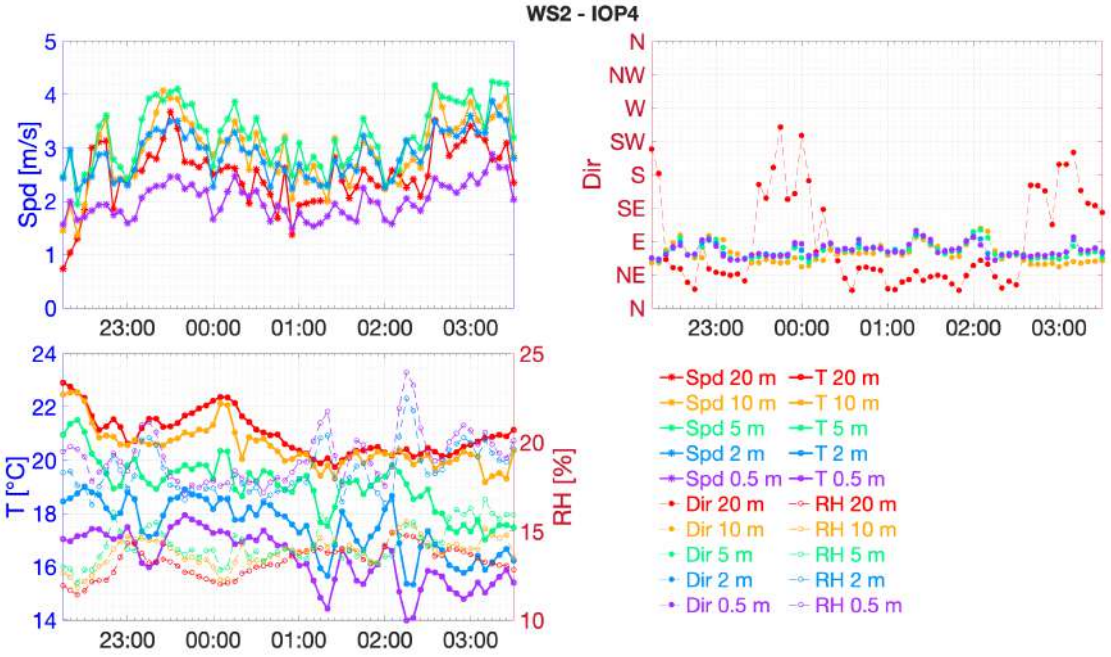

Figure 4.49: *Time series zoom on 11/12 May 2013 at WS2 during the Period 3. Times are in local time (MDT)*

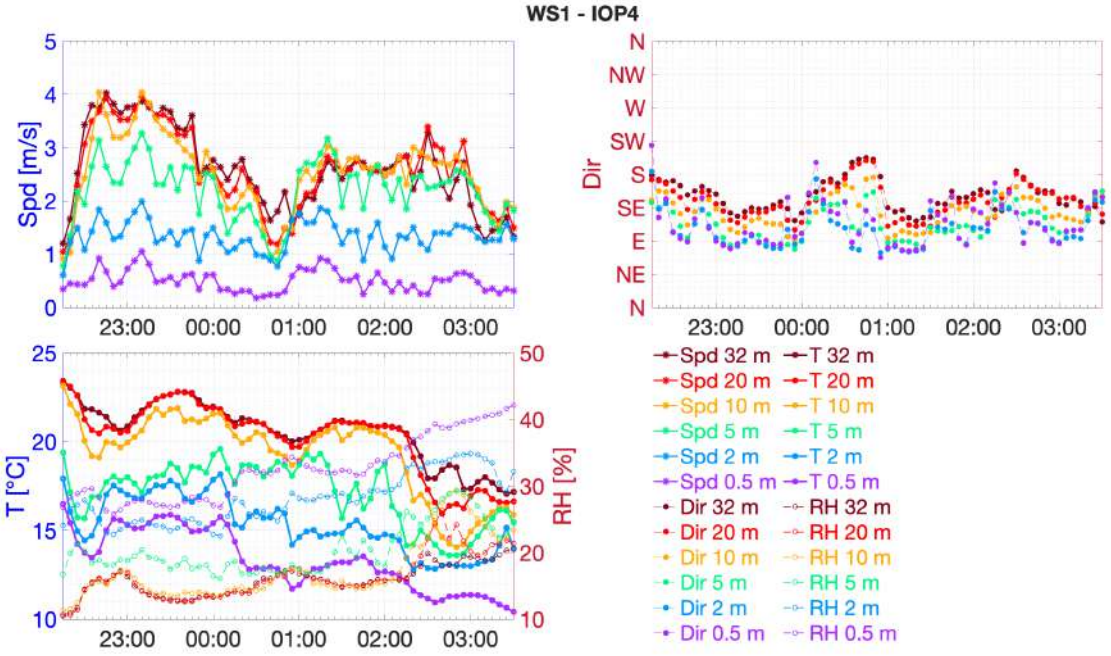

Figure 4.50: *Time series zoom on 11/12 May 2013 at WS2 during the Period 3. Times are in local time (MDT)*

4.3.2.4 TKE and its component

This section addresses the TKE and its components description during the morning transition time. Given the focus only on the morning transition processes, the TKE and its components time series in figure 4.51 and 4.52 do not show the entire analyzed period of section 4.3.2.1. Before sunset, the TKE and its components show the characteristic CBL turbulence. In fact, the highest values are reached during this period. The unstable stratification of CBL is clearly visible in the slope-normal component, but the higher values, comparable with those of the TKE, are reached by the streamwise and spanwise component. The TKE values during the CBL are higher on IOP4, during which evening near surface flows are well developed and the wind speed is higher than that on IOP6. Despite the absence of a persistent evening calm period, both because of the relatively high speed values and because of the short duration of the wind speed decrease throughout the transition, the TKE and its components drop and reach the minimum value right between the astronomical and the local sunset also in the case of IOP6 where the transition proceeds as a slow but continuous wind rotation. The TKE and both the slope-parallel components observed during the IOP4 shows slight fluctuations just before local sunrise at WS2 and immediately after at WS1, which may depend on the downslope activation that propagates from the WS2 to the WS1.The slow and gradual transition on IOP6 with low wind speed values leads to lower TKE values. The downslope on IOP6, which has a lower speed values than that on IOP4, is hidden by the fluctuation of the TKE, except for maximum value reached just after sunset in the TKE and in the spanwise component that is at the same time as the downslope onset at WS2. The anisotropy between both the slope-parallel components and the slope normal component increase after sunset, with the strengthening of the nocturnal stable stratification.

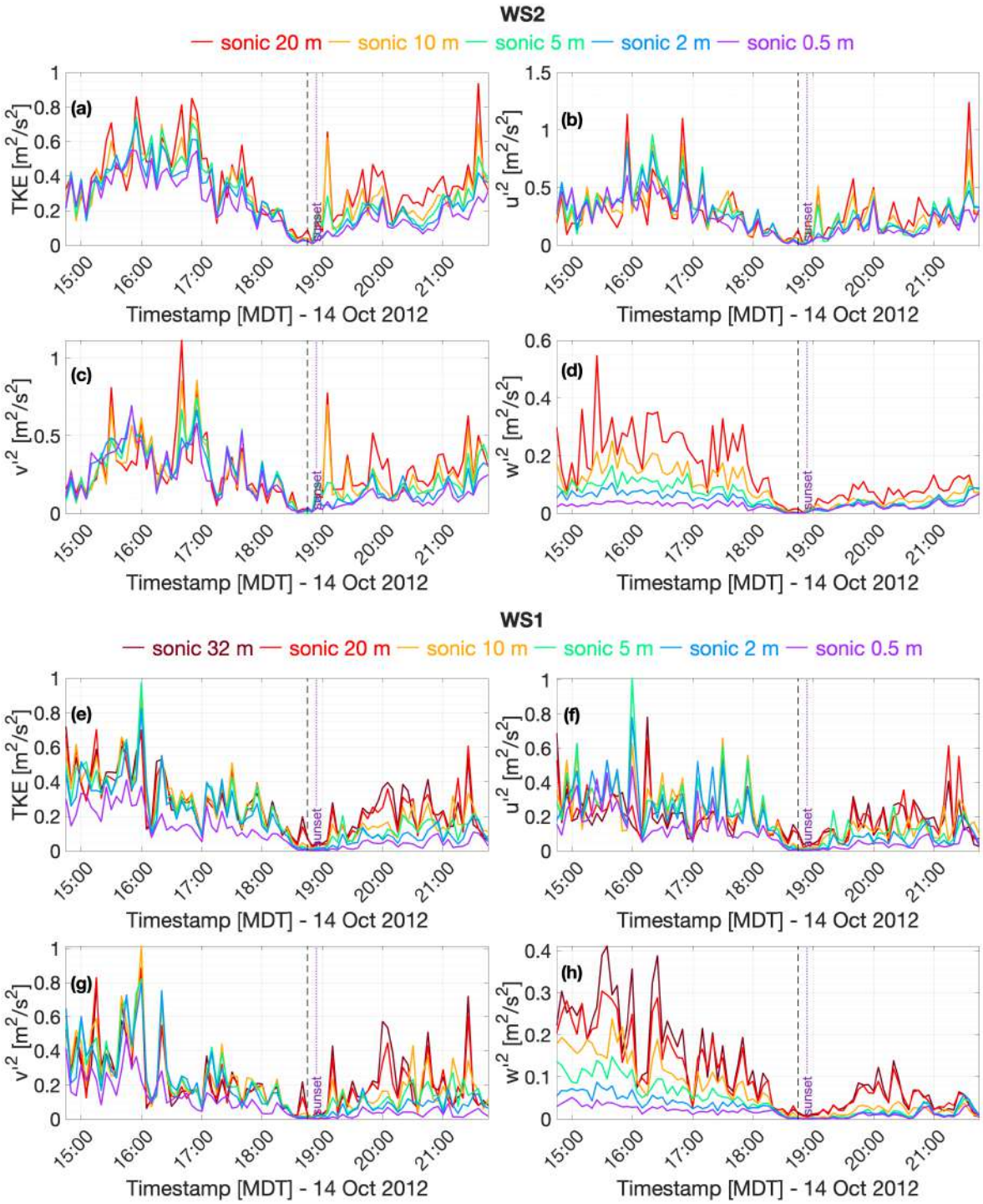

Figure 4.51: *Turbulent kinetic energy and its streamwise, spanwise and slope-normal components at WS2 ((a), (b), (c), (d)) and at WS1 (e), (f), (g), (h)) on IOP6 (14 October 2012). Vertical dashed line identify local sunset. The purple dotted line is at astronomical sunset*

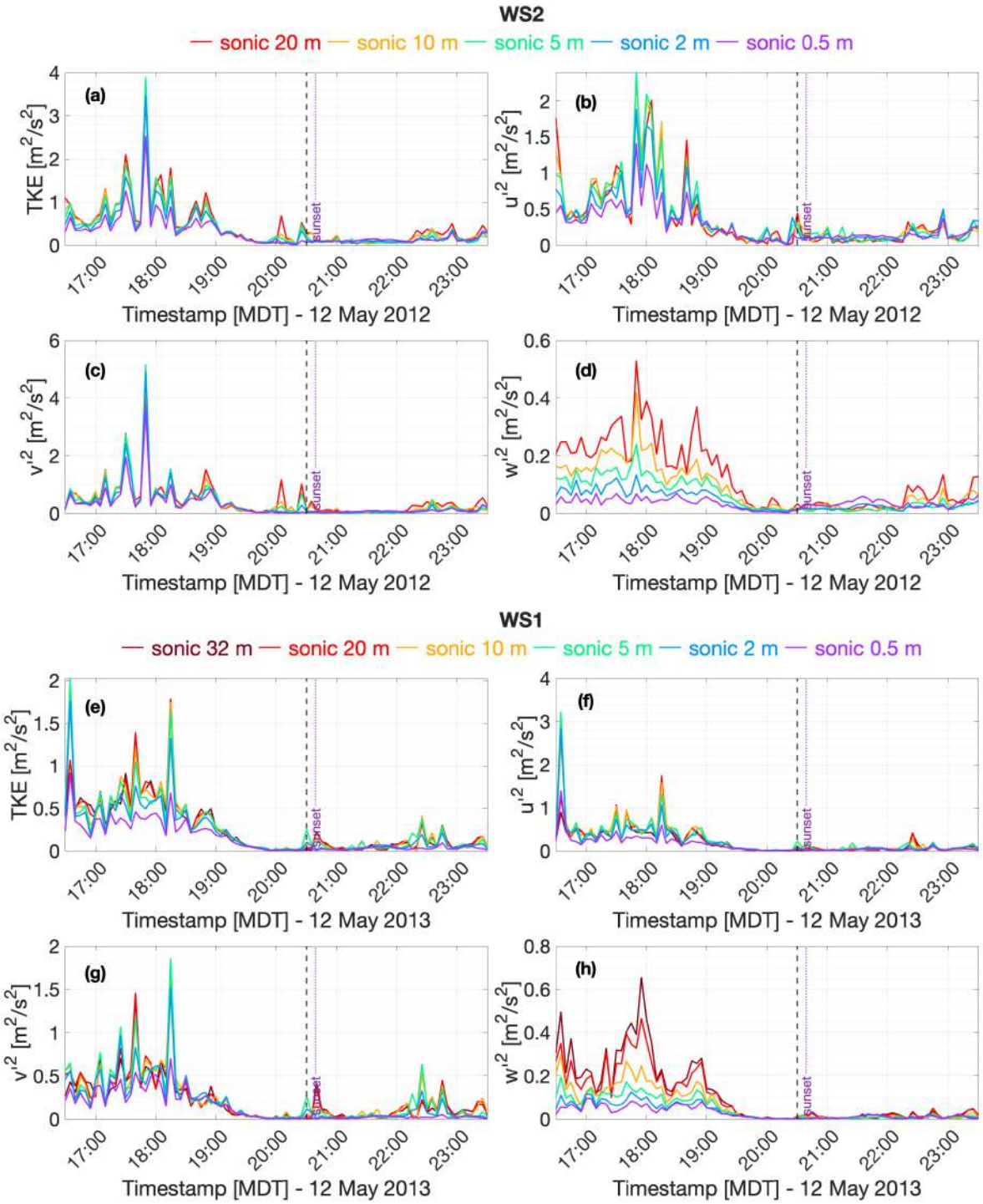

Figure 4.52: *Turbulent kinetic energy and its streamwise, spanwise and slope-normal components at WS2 ((a), (b), (c), (d)) and at WS1 (e), (f), (g), (h)) on IOP4 (11 May 2013)Vertical dashed line identify local sunset. The purple dotted line is at astronomical sunset*

4.3.2.5 Kinematic heat flux

As the shortwave radiation falls gradually during the evening transition, the unstable diurnal stratification becomes progressively stable. Thus the kinematic heat flux $\overline{w'T'}$ change sign from positive to negative. The PSR is longer on IOP6 and shorter on IOP4, showing the same pattern as the transition

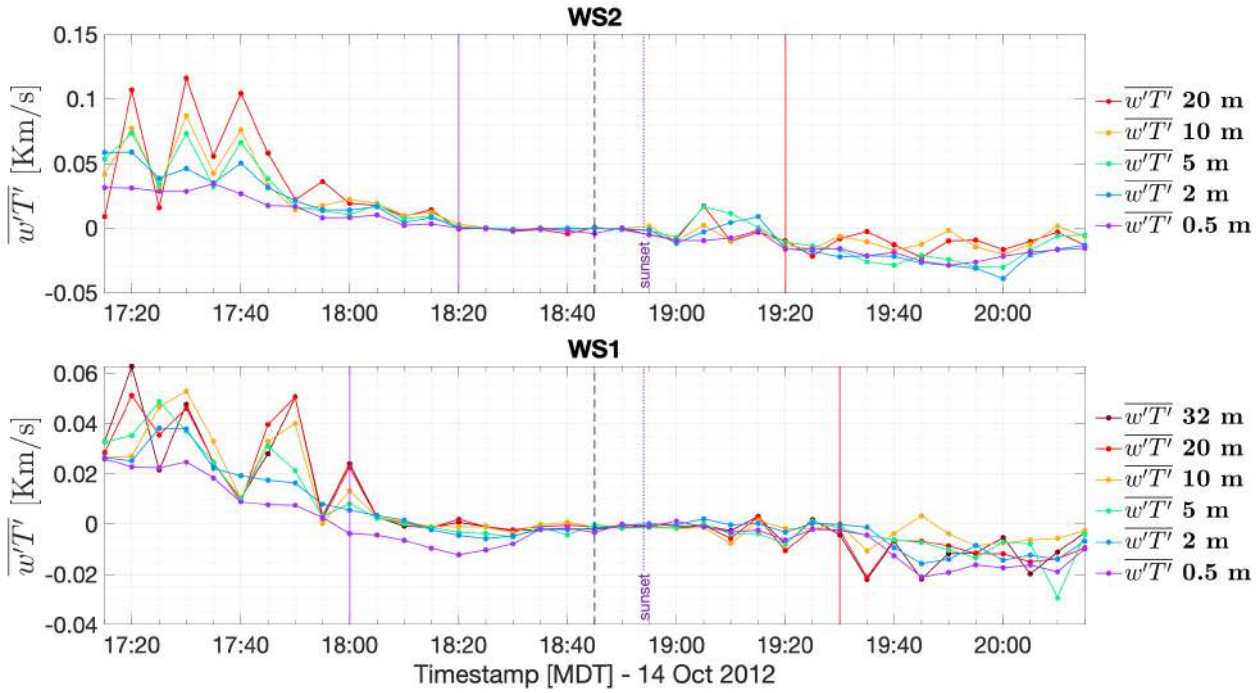

Figure 4.53: *Evolution of the kinematic heat flux around sunset on IOP6 (14 October 2012) at (a) WS2 and (b) WS1. The central dashed line, as in all charts, identify local sunset at WS2. The purple and the red vertical lines identify the PSR at WS2 between 0.5 m and 20 m AGL.*

The PSR identification is affected by many fluctuation in the kinematic heath flux. For example, on IOP6 between 19:00-19:20 MDT (Fig. 4.53) when the fluxes show an increase. This period coincides with the onset of the downslope at WS2, slightly before the transition end. Thus it is reasonable that the PSR ends after thi fluctuation, at the end fo the rotation. On the contrary, at WS1 there is only an instant, at 19:15 MDT, during wich the fluxes become positive, but this fluctuation is instantaneous and localized

only above 10 m. Looking at the WS1, the cooling process above 5 m AGL during the spring IOP is almost absent. This is in accordance with the downward propagation of the transition

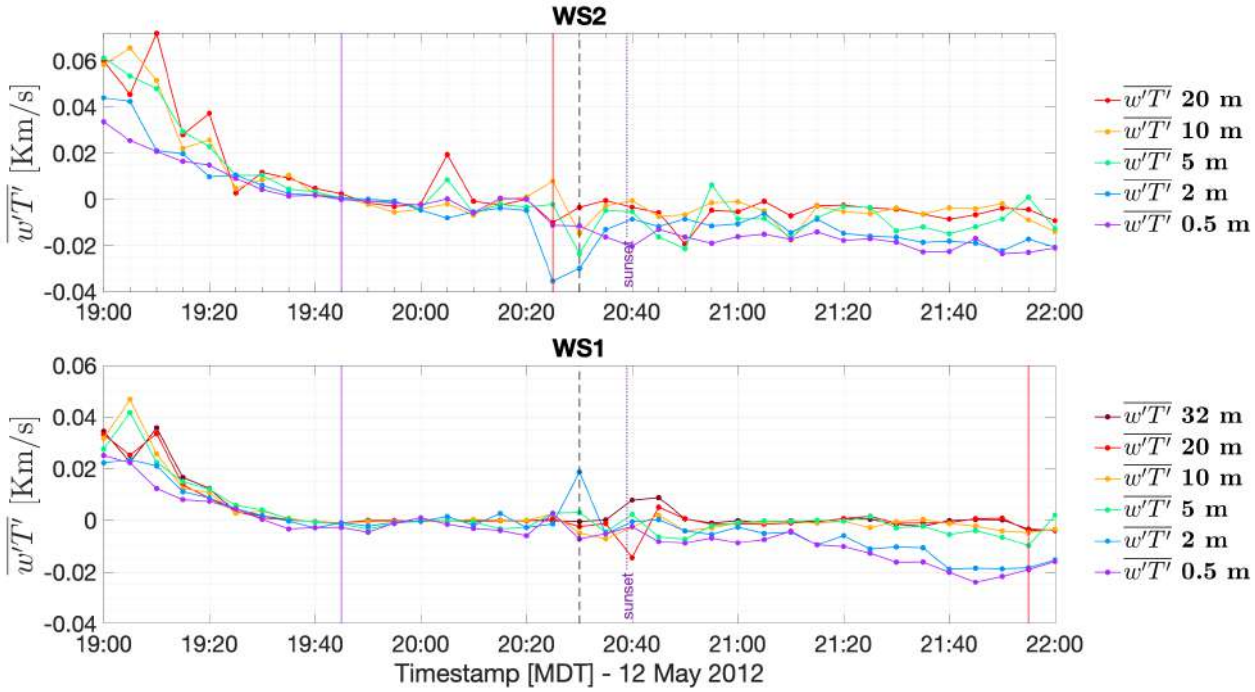

Figure 4.54: *Evolution of the kinematic heat flux around sunset on IOP4 (11 May 2013) at (a) WS2 and (b) WS1. The central dashed line, as in all charts, identify local sunrise at WS2. The purple and the red vertical lines identify the PSR at WS2 between 0.5 m and 20 m AGL. Times are in MDT*

4.3.3 Transition Length

The evening transition occurs very differently in the two IOPs analyzed. On IOP6 the wind transition occurs at the highest tower first, while on IOP4 the transition occurs from the one on the lowest part of the slope. These two wind direction behaviors are associated with two different types of CBL strength.

On IOP6 the CBL is weakly developed and the near surface flows are weak, with an upslope at WS2 and an upslope/up-valley at WS1 only hinted. The transition starts at WS2, 2 hours and 15 minutes before the local sunset. On WS1 the transition begins 1

hour and 55 minutes before the local sunset. First the kinematic heath fluxes are reversed at WS1, then at WS2, while the onset of the surface temperature inversion takes place first at WS2 and then at WS1, following the transition development. The transition ends 35 minutes after local sunset. A weak CBL is thus in this case linked to an upslope weakening at WS2 before the down-valley wakening at WS1. The resulting downslope is weak and has a limited vertical extension.

In IOP4, CBL is well developed and up-valley is observed at both towers. The transition starts from below at WS1, 1 hour and 20 minutes before local sunset and at WS2 55 minutes before local sunset. The onset of thermal inversion is always from the WS2, as well as the PSR. The downslope that is generated is stronger and when it reaches WS1 the transition at WS2 is practically over. A well developed CBL is in this case is characterized first by an up-valley weakening starting at WS1, while on the WS2 the up-valley persists longer. The downslope developed in this case is stronger and has a larger vertical extension.

IOPs	**TL WS1**	**TL WS2**	**WS1 TSIO**	**WS2 TSIO**	**PSR WS1**	**PSR WS2**
IOP6 1845	2h30min [1650]	2h50min [1630]	1850	1845	1h30min [1800]	60min [1820]
IOP4 2050	2h25min [1930]	40 min [1955]	2020	2005	2h10min [1945]	40 min [1945]

Table 4.3: *Characteristic parameters of the evening transition. Local sunrise time is shown under each IOP name. TL: transition length (The onset time is reported below the length). TSIO: Time of Surface Inversion Onset ($T_{0.5m} < T_{20m}$). PSR: Period of Sign Reversal of kinematic heath flux. For the TL and the PSR the onset time of the process are reposted in square brackets. Times are in MDT.*

Chapter 5

Summary and conclusion

The results presented in this thesis work are based on the data collected during the Mountain Terrain Atmospheric Modeling and Observations field campaign (MATERHORN) that took place in Utah near the Granite Mountain between 2012 and 2013. The analysis of the morning and of the evening transition concerned the near surface branch of the thermal circulation that develops on the gentle isolated slope on the west side of the mountain during four quiescent IOPs, based on the 700 hPa wind speed $v < 5m/s$. The west slope was the less instrumented site of the field campaign and for this reason it has never been studied. The choice of the IOPs was strongly affected by the availability of the data. In fact, the morning transition was characterized through the analysis of two fall IOPs (IOP2 and IOP6) while the evening transition was characterized by the analysis of a fall IOP (IOP6) and of a spring IOP (IOP4), but with a comparison between them and other two IOPs (IOP2 of the fall campaign and IOP7 of the spring campaign).

Firstly the characterization of the transitions was made with the analysis of the evolution of solar radiation, highlighting the differences between the west and the east slope insolation. Secondly, the transitions characterization was performed trough a range of data which spanned from several hours before to several hours after the transitions occurrence, in order to have a comprehensive understanding of the processes. Finally, the transitions were characterised by the TKE and kinematic flux of heath variation.

The flux Towers show that during the quiescent IOPs both slope and valley winds develop on the west gentle slope. The upper part of the slope is more exposed by the along-

slope wind and during the night the wind is from a northeasterly downslope direction, while during the day the wind is a southwesterly upslope. As far as the slope becomes more gentle and the valley opens up, the slope-valley wind is slightly clockwise rotated showing predominantly a southeasterly down-valley during the night and a northwesterly up-valley during the day. During the night, when the stratification is stable and the wind speed is low the winds that blow on the west slope arises from the interaction between the slope and the valley flow, showing a strong directional wind shear at both tower, as for example on the east slope (Lehner et al., 2015) and in the Salt Lake Valley (Whiteman and Zhong, 2008). The interaction between the downslope and the valley inversion causes an intermittent cooling-warming process. The temperature rising associated with the presence of the downslope during the night is due to a warm advection cased by the mixing with the warmer air from above (Papadopoulos and Helmis, 1999) and by compressional warming during the flow descent (Fleagle, 1950). As the down-valley wind blowing from the south converges rapidly with the northeasterly downslope, the resulting wind rotates from southeast at both towers, and the cooler air moves up the slope, also pushed by the westerly valley inversion, causing a temperature drop that climbs the slope, just like in the east slope (Lehner et al., 2015).

Before the morning transition, once the sun rises, the west side of an isolated mountain is not immediately illuminated by direct light but undergoes a period of twilight that lasts more than an hour, characterized by the presence of diffuse radiation only that is not observed on the east side. In fact after astronomical sunrise the west slope gets illuminated at its top and then at its bottom, while the central sections of the steepest part remain in the shade even after several hours from astronomical sunrise. However, only the direct solar radiation provides enough energy for the ground to be heated and to warm the near surface atmosphere, activating the destruction of the nocturnal regime. In addition, direct solar radiation propagates from the flattest to the steepest part of the gentle slope.

During the morning transition, two main phenomena take place: the erosion of the temperature inversion and the rotation (i.e. transition) of the wind from the nocturnal to the diurnal regime. The two phenomena do not necessarily occur in order, and may even occur simultaneously depending on the warming process which in turn depends on

the nocturnal nocturnal boundary layer development. On IOP2 the stronger temperature gradient, with respect to the IOP6, is associated with larger wind speed and direction variability and with a more intense but less frequent downslope events, in accordance with the work of Banta and Gannon, 1995. On the contrary, on IOP6 the absence of large disturbances with the variables showing an oscillatory behavior throughout the night, could be caused by the high relative humidity, as a result of the increase in evaporation rate after the rainfall on 13 October 2012 (Hang et al., 2016), triggering lower cooling (Sastre et al., 2015).The increased soil thermal conductivity, due to high values of soil moisture, allows for heat exchange with a deeper layer of soil and effectively reduces the cooling at the slope surface. The reduced near-surface cooling is responsible for reducing the strength of the downslope flow (Banta and Gannon, 1995). The lower soil moisture on IOP2 leads to lower albedo values and thus on IOP2 he warming process and thus the transition is triggered by surface heating starting from the flattest part of the west slope. This type of temperature inversion destruction resemble the one that occurs over flat terrain and leads to an upward growth of the CBL (Whiteman, 1982; De Wekker and Kossmann, 2015). In this case the transition starts at within the valley before local sunrise, while on the slope the transition takes place before the surface inversion breakup. On the contrary the higher soil moisture and humidity of the air during the IOP6 leads to a less efficient absorption of the solar radiation and a slower, ground warming so in this case the heating process starts from above due to mixing with the overlying air, that is the top-down dilution (Papadopoulos and Helmis, 1999), and due to the presence of horizontal heat transfer from the heated slope (De Wekker and Kossmann, 2015; Princevac and Fernando, 2008). In this case the transition at WS1 is delayed, and the transition at WS2 is faster and takes place exactly at the surface inversion breakup. The transition length based on the wind rotation is in good agreement with the PSR of the kinematic heat flux, that is the period between the sign reversal of the kinematic heat flux at 0.5 m and at 20 m. The morning transition is also characterized by the presence of the so called “morning calm period” (De Wekker and Kossmann, 2015; Nadeau et al., 2020) that is the wind speed drop which usually occurs during the rotation of the wind. The occurrence of the morning calm period seems to depends on the heating mechanism, showing an earlier occurrence when the surface heating is predominant (on IOP2) with respect to the

warming of the air from above (on IOP6). Before local sunrise, when the slope-normal component is very small due to stable stratification and the TKE results mainly from the horizontal components, the spanwise component in the valley is the most similar to the TKE, emphasizing the importance of the valley influence on this tower. At the same time, the streamwise component on the slope is almost equal to the TKE, which confirms the presence of a stronger slope regime and the quasi-2D nature of the flow. During this same period, the TKE is on average larger and more variable during the IOP2, which in fact is the one that has the greatest fluctuations of wind speed and direction.

The evening transition on the west slope, contrary to what is observed on the east slope or in a narrow alpine-like valley, is not characterized by the movement of a shadow front and therefore the radiation does not undergo sudden drops. In every topographical configuration on which the shadow front develops, the transition and the cooling process are triggered by differential heating dew to the shadow propagation and develop following its upward or downward propagation (Nadeau et al., 2013; Lehner et al., 2015; Jensen et al., 2017; Nadeau et al., 2020). The absence of topography to the west of the Granite Mountain determines a gradual and progressive decrease of the shortwave solar radiation. However the radiation decrease due to the sun fading is faster over the valley and on the less inclined area of the slope than on the steepest part, on which solar radiation persist up to astronomical sunset. Nevertheless, as it was during the morning transition, some sections of the steeps part go in the shade far before the astronomical sunset, due to the specific topographic configuration.

The temperature variation and the wind rotation occurs even during the evening transition, but in this case the two processes are reversed. The air cools reaching the surface temperature inversion onset and the wind shift from diurnal to nocturnal direction. The two phenomena do not necessarily occur in order, and may even occur simultaneously, as for the morning transition, depending on the cooling process, which however depends on the CBL decay.

The evening transition takes place in a very different way during the two IOPs analyzed. During the IOP6 the warming process from above due to the mixing with the overlying air and heat transfer from the valley sidewall surfaces to the valley atmosphere, (De Wekker and Kossmann, 2015) leads to an unstable profile topped by a stable stratification

developed in the early evening. This type of stratification suggests the absence of a strong convective structure, which is instead characterized by the presence of a well mixed layer (i.e., neutral stratification) above the near-the-ground unstable profile (that is the usual potential temperature profile in the slope surface layer in the late morning/early evening, according to De Wekker and Kossmann, 2015. The weakly developed CBL leads to both an upslope on the slope and an upslope/up-valley at the slope foot only hinted during the evening, and is linked to the occurrence of an upslope weakening along the slope before the down-valley wakening. In fact, the transition starts along the slope and takes place long before the local sunset. The rotation of the wind is slow and very gradual. The onset of the surface temperature inversion takes place first on the slope and then within the valley, following the transition development. The unstable stratification topped by the stable one is linked to the occurrence of a modest downslope acceleration with frontal characteristics that has a limited vertical extension, accompanied by a warm advection that rises the temperature due to mixing with the warm air from the upper part of the slope (Papadopoulos and Helmis, 1999). During the IOP4 a well developed CBL is characterized firstly by an up-valley weakening at the slope foot, while along the slope the up-valley persists longer. The transition starts from the slope foot, and is delayed with respect to the transition onset at IOP2. However, the onset of thermal inversion is always from the slope to the valley. The downslope developed in this case is stronger and has a larger vertical extension (Papadopoulos and Helmis, 1999). In contrast, on IOP2 the well developed CBL is associate with a neutral stratification and a strong downslope, showing the transition onset starting from the valley, and on IOP7 the CBL is less well developed than that on IOP2 and IOP4, but the stratification is as neutral as in IOP4, the transition is gradual and from valley, while the downslope onset is strongly delayed. The IOP7 resembles the characteristics of IOP4, although the IOP2, during which the heating from below is strong and the CBL is well developed, shows the transition onset opposes that observed during the IOP4. So this is not possible to find any seasonal pattern or correlation between the CBL development and the transition onset. The evening calm usually does not occur, probably because of the absence of a sudden solar radiation decrease (i.e., the absence of the shadow front). Nevertheless, the evening transition is often preceded by a wind speed decrease. Before the transition, TKE and its components

show the characteristic CBL turbulence. In fact, the highest values are reached during this period. The TKE values during the CBL are higher on IOP4, during which evening near surface flows are well developed and the wind speed is higher. Despite the absence of a persistent evening calm period, the TKE and its components drop and reach the minimum value right between the astronomical and the local sunset, which occur with a difference of only 10 minutes. The TKE and both the slope-parallel component on IOP4 show slight fluctuations due to the downslope activation that propagates from the slope to the valley. The slow and gradual transition on IOP6 with low wind speed values do not allow to see the activation of the downslope from the TKE. The PSR is in good agreement with the transition length and its onset on IOP4. During this IOP, after the sunset, the kinematic heat flux show an efficient cooling below 2 m AGL. This is in accordance with the cooling onset from below which occurs during this IOP.

In conclusion, the morning and the evening transition on the west gentle slope of the Granite mountain are both triggered by the radiation variation, but the behavior with which the transitions take place depends on the preexistence characteristics of the boundary layer. However the analysis of only 4 case studies is not a sufficient statistics, and therefore other studies on the subject would be necessary to verify or disprove what we have found. Naturally, if supported by complementary instruments (e.g. tethersonde), the analysis of the transitions on the west-facing slope and the vertical structure of the boundary layer can be significantly enhanced.

Bibliography

Arya, S. P. (2001). *Introduction to Micrometeorology*. Internation Geophisics Series, Volume 79.

Aubinet, M., Vesala, T., and Papale, D. (2012). *Eddy covariance: a practical guide to measurement and data analysis*. Springer Science & Business Media.

Banta, R. and Gannon, P. (1995). Influence of soil moisture on simulations of katabatic flow. *Theoretical and applied climatology*, 52(1):85–94.

De Wekker, S. F. J. and Kossmann, M. (2015). Convective boundary layer heights over mountainous terrain—a review of concepts. *Frontiers in Earth Science*, 3:77.

Ekhart, E. (1948). De la structure thermique de l'atmosphere dans la montagne [on the thermal structure of the mountain atmosphere]. *La météorologie*, 4(9):3–26.

Fernando, H. (2010). Fluid dynamics of urban atmospheres in complex terrain. *Annual review of fluid mechanics*, 42:365–389.

Fernando, H., Pardyjak, E., Di Sabatino, S., Chow, F., De Wekker, S., Hoch, S., Hacker, J., Pace, J., Pratt, T., Pu, Z., et al. (2015). The MATERHORN: Unraveling the intricacies of mountain weather. *Bulletin of the American Meteorological Society*, 96(11):1945–1967.

Fleagle, R. G. (1950). A theory of air drainage. *Journal of Atmospheric Sciences*, 7(3):227–232.

Hang, C., Nadeau, D., Jensen, D., Hoch, S., and Pardyjak, E. (2015). Playa Soil Moisture and Evaporation Dynamics During the MATERHORN Field Program. *Boundary-Layer Meteorology*, 159:521–538.

Hang, C., Nadeau, D. F., Jensen, D. D., Hoch, S. W., and Pardyjak, E. R. (2016). Playa soil moisture and evaporation dynamics during the materhorn field program. *Boundary-layer meteorology*, 159(3):521–538.

Hersbach, H., Bell, B., Berrisford, P., Biavati, G., Horányi, A., Muñoz, S. J., Nicolas, J., Peubey, C., Radu, R., Rozum, I., Schepers, D., Simmons, A., Soci, C., Dee, D., and Thépaut, J.-N. (2018). Era5 hourly data on single levels from 1979 to present. Copernicus Climate Change Service (C3S) Climate Data Store (CDS). (Accessed on 18-09-2021), 10.24381/cds.adbb2d47.

Horst, T. and Doran, J. (1986). Nocturnal drainage flow on simple slopes. *Boundary-Layer Meteorology*, 34(3):263–286.

Jensen, D. D., Nadeau, D. F., Hoch, S. W., and Pardyjak, E. R. (2017). The evolution and sensitivity of katabatic flow dynamics to external influences through the evening transition. *Quarterly Journal of the Royal Meteorological Society*, 143(702):423–438.

Kaimal, J. C. and Finnigan, J. J. (1994). *Atmospheric boundary layer flows: their structure and measurement*. Oxford university press.

Kossmann, M., Vögtlin, R., Corsmeier, U., Vogel, B., Fiedler, F., Binder, H.-J., Kalthoff, N., and Beyrich, F. (1998). Aspects of the convective boundary layer structure over complex terrain. *Atmospheric Environment*, 32(7):1323–1348.

Lehner, M. and Rotach, M. W. (2018). Current challenges in understanding and predicting transport and exchange in the atmosphere over mountainous terrain. *Atmosphere*, 9(7).

Lehner, M., Whiteman, C. D., Hoch, S. W., Jensen, D., Pardyjak, E. R., Leo, L. S., Di Sabatino, S., and Fernando, H. J. (2015). A case study of the nocturnal boundary layer evolution on a slope at the foot of a desert mountain. *Journal of Applied Meteorology and Climatology*, 54(4):732–751.

Monti, P., Fernando, H. J. S., Princevac, M., Chan, W. C., Kowalewski, T. A., and Pardyjak, E. R. (2002). Observations of flow and turbulence in the nocturnal boundary layer over a slope. *Journal of the Atmospheric Sciences*, 59(17):2513 – 2534.

Nadeau, D. F., Oldroyd, H. J., Pardyjak, E. R., Sommer, N., Hoch, S. W., and Parlange, M. B. (2020). Field observations of the morning transition over a steep slope in a narrow alpine valley. *Environmental Fluid Mechanics*, 20(5):1199–1220.

Nadeau, D. F., Pardyjak, E. R., Higgins, C. W., Huwald, H., and Parlange, M. B. (2013). Flow during the evening transition over steep alpine slopes. *Quarterly Journal of the Royal Meteorological Society*, 139(672):607–624.

Papadopoulos, K. and Helmis, C. (1999). Evening and morning transition of katabatic flows. *Boundary-Layer Meteorology*, 92(2):195–227.

Princevac, M. and Fernando, H. (2008). Morning breakup of cold pools in complex terrain. *Journal of fluid mechanics*, 616:99–109.

Sastre, M., Yagüe, C., Román-Cascón, C., and Maqueda, G. (2015). Atmospheric boundary-layer evening transitions: a comparison between two different experimental sites. *Boundary-Layer Meteorology*, 157(3):375–399.

Serafin, S., Adler, B., Cuxart, J., De Wekker, S. F. J., Gohm, A., Grisogono, B., Kalthoff, N., Kirshbaum, D. J., Rotach, M. W., Schmidli, J., Stiperski, I., Večenaj, Ž., and Zardi, D. (2018). Exchange processes in the atmospheric boundary layer over mountainous terrain. *Atmosphere*, 9(3).

Skyllingstad, E. D. (2003). Large-eddy simulation of katabatic flows. *Boundary-layer meteorology*, 106(2):217–243.

Stull, R. (2015). *Practical Meteorology: An Algebra-based Survey of Atmospheric Science*. UBC.

Whiteman, C. D. (1982). Breakup of temperature inversions in deep mountain valleys: Part i. observations. *Journal of Applied Meteorology and Climatology*, 21(3):270–289.

Whiteman, C. D. (2000). *Mountain Meteorology Fundamentals and Applications*. Oxford University Press.

Whiteman, C. D. and Zhong, S. (2008). Downslope flows on a low-angle slope and their interactions with valley inversions. part i: Observations. *Journal of Applied Meteorology and Climatology*, 47(7):2023–2038.

Zardi, D. and Whiteman, C. (2013). Diurnal mountain wind systems. In Chow, F. K., De Wekker, S. F., and Snyder, B. J., editors, *Mountain Weather Research and Forecasting*, chapter 2, pages 35–119. Springer, Dordrecht, Springer Atmospheric Sciences.